

The Age and Metallicity Dependence of the Near-Infrared Magnitudes of Red Clump Stars

著者	Onozato Hiroki
学位授与機関	Tohoku University
学位授与番号	11301甲第18436号
URL	http://hdl.handle.net/10097/00125497

博士論文

**The Age and Metallicity Dependence of the
Near-Infrared Magnitudes of Red Clump Stars**
(レッドクランプ星の近赤外線等級の
金属量・年齢依存性)



Astronomical Institute, Graduate School of Science, Tohoku University
東北大学大学院 理学研究科 天文学専攻

Hiroki Onozato
小野里宏樹

平成 30 年

Abstract

Red clump (RC) stars are low mass stars with relatively high metallicity in the core helium-burning phase. They have small scatter of luminosity and effective temperature, and they can be used as a standard candle. The advantage of RC stars as a standard candle is that the number of RC stars is numerous and the statistical error could be small in comparison to variable stars with period-luminosity relation. A large number of RC stars also allows us to utilize them as the tracer of the structure of objects and interstellar extinction. Furthermore, RC stars are luminous in the near-infrared wavelength, and they can be used in the region where interstellar extinction is strong, and stars cannot be observed in the optical wavelength. For example, distance to the Milky Way bulge or nearby galaxies is measured using RC stars with uncertainty smaller than 0.2 mag (~ 20 per cent) in distance modulus.

However, it has been understood from both theoretical and observational work that the absolute magnitude of RC stars depends on age and metallicity (population effect). The population effect is considered to be smaller in infrared than in optical, but relatively large age dependence is predicted for young RC stars. The difference of absolute magnitude in young RC stars are predicted as about 0.5 mag, and it leads to 50 per cent uncertainty in distance determination. Therefore, it is important to confirm the RC population effect by observation. Many studies have confirmed small metallicity dependence. On the other hand, age dependence has not been investigated extensively because it is difficult to obtain the ages of RC stars. So far, the studies are limited to the work using Milky Way star clusters or age that derived from asteroseismology. Thus, the number of samples with both age and metallicity information is quite limited, and the parameter space is not covered enough up until now.

Hence, we use star clusters in the Large Magellanic Cloud (LMC) to fill the parameter space, which previous research has not observationally studied. Star clusters in the LMC are more metal-poor than star clusters containing RC stars in the Milky Way. Also, there are many young star clusters in the LMC. Therefore, we can expand the parameter space to the more metal-poor and younger range. To observe the LMC star clusters, we used the IRSF telescope with long exposure time and VMC survey data.

We obtained empirical relations of the population effect for RC absolute magnitudes m_J , m_H , and m_{K_S} , and their colors $J - H$, $J - K_S$, and $H - K_S$. Especially, we confirmed that $J - K_S$, and

$H - K_S$ have nearly constant values $J - K_S = 0.512 \pm 0.012$ and $H - K_S = 0.050 \pm 0.010$ at least within the ages of 1.5–3.5 Gyr and -0.90 to -0.40 dex. This means that these colors are useful as an interstellar extinction probe. We also confirmed that the population effect of observational data is in good agreement with the newer theoretical models.

Contents

Abstract	i
1 Introduction	1
1.1 Red clump stars	1
1.2 RC stars as a standard candle	3
1.2.1 RC stars as a distance indicator	5
1.2.2 RC stars as the tracer of structures	8
1.2.3 RC stars as an interstellar extinction probe	15
1.3 Absolute magnitudes of RC stars	17
1.4 Star Clusters in the Large Magellanic Cloud	30
1.5 RC stars and stellar evolution	30
1.6 Structure of This Thesis	34
2 The Data	35
2.1 IRSF data	35
2.1.1 Sample selection	35
2.1.2 Age and metallicity of Palma's catalog	37
2.1.3 Observation	41
2.1.4 Data reduction	41
2.2 VMC data	45
2.2.1 Sample Selection	45
2.2.2 RC magnitudes determination	49
3 Results and discussion	51
3.1 Age dependence	51
3.2 Metallicity dependence	63
3.3 Absolute magnitude	64
3.4 RC stars as a standard candle	67

CONTENTS

4	Conclusions and future work	74
4.1	Conclusions	74
4.2	Future work	74
	Acknowledgments	76
	References	77
A	Density maps of VMC survey tiles	82

Chapter 1

Introduction

1.1 Red clump stars

Red clump (RC) stars are evolved from low mass stars with relatively high metallicity. They are in the core helium-burning (CHeB) phase and the next stage of the first ascent red giant branch (RGB) stars. Low mass stars with low metallicity will evolve to hotter CHeB stars, such as horizontal branch (HB) stars or RR Lyrae variable stars. Although both RC stars and HB stars are the CHeB stars, the number of RC stars is much larger than that of HB stars. About 1/3 of all red giants are RC stars in any star-forming galaxies ([Girardi 2016](#)).

In spite of the fact that RC stars are abundant, it has only been half a century since RC stars were recognized. It is in contrast to HB and RR Lyrae stars, which have been studied in old globular clusters for more than one hundred years (e.g., [Bailey 1902](#)). [Cannon \(1970\)](#) first reported that RC stars are in the color-magnitude diagrams (CMDs) of intermediate-age clusters ([Figure 1.1](#)). Not only he identified RC stars, but also he mentioned that RC stars have nearly constant magnitude ($M_V = 0.9 \pm 0.1$, [Figure 1.2](#)) and can be used for a standard candle. In addition, he correctly interpreted that RC stars are evolved from low-mass RGB stars. However, RC stars had been rarely studied for about 30 years after his work, except for the studies of open clusters, Local Group galaxies, and theoretical work on stellar evolution. Examples of a few exceptions that RC stars were used for distance estimation are the work by [Stanek et al. \(1994, 1997\)](#), who used the luminosity distribution of the RC stars as evidence for the Galactic Bar.

The situation drastically changed after work by [Paczynski & Stanek \(1998\)](#). They used the *Hipparcos* parallaxes of around 600 RC stars to determine the absolute magnitudes of RC stars in the solar neighborhood, and showed that RC stars have compact distribution in the CMDs ([Figure 1.3](#)). The different points between their work and [Cannon \(1970\)](#) are the number of RC samples and [Paczynski & Stanek \(1998\)](#) selected *I*-band data, which have smaller color dependence of the absolute magnitudes (approximately corresponding to metallicity dependence). Especially, it is surprising that RC stars in both of two completely different regions (solar neighborhood and

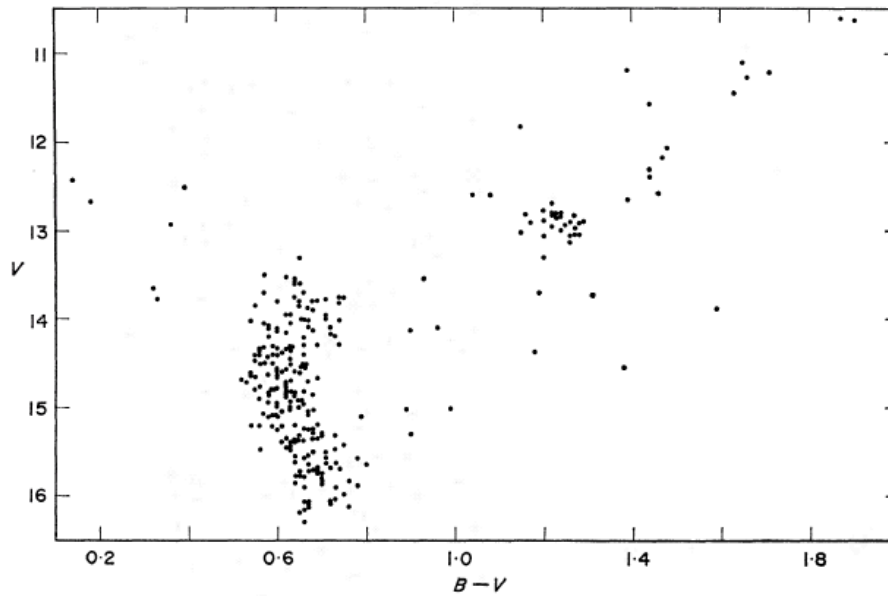


Figure 1.1: The $(B - V, V)$ CMD of NGC 7789. This figure is taken from Cannon (1970), reproduced with the permission of Oxford University Press.

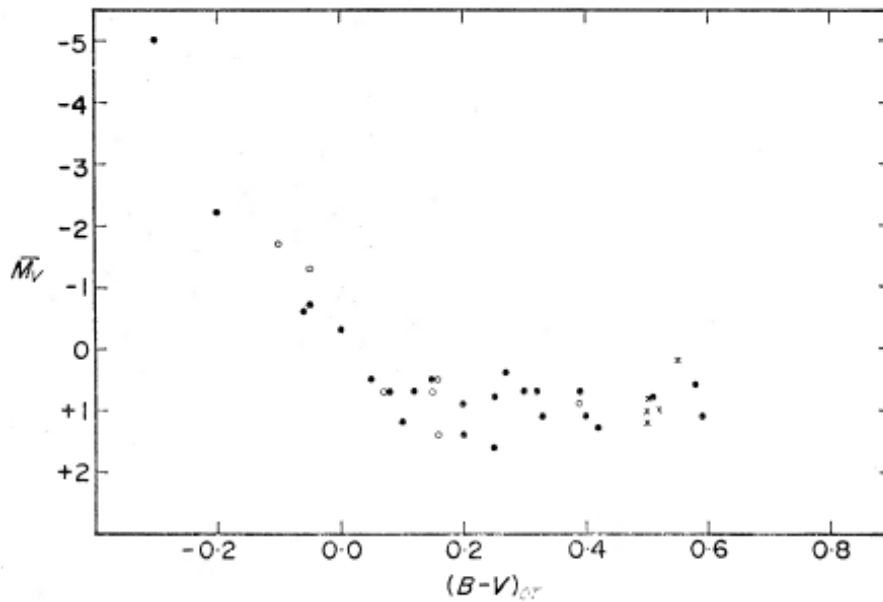


Figure 1.2: The mean V -band absolute magnitudes of RGB stars in star clusters as a function of cluster turn-off colors. This figure is taken from Cannon (1970), reproduced with the permission of Oxford University Press.

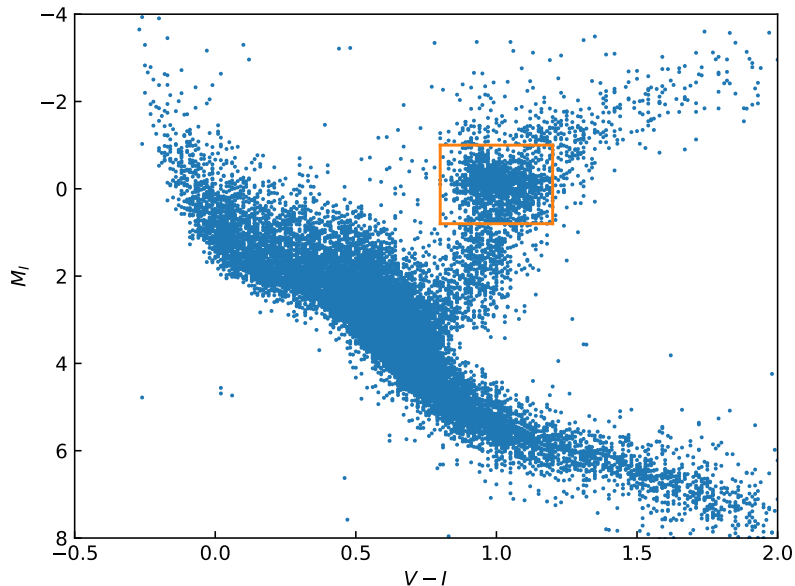


Figure 1.3: CMD of $V - I$ versus M_I for the stars with *Hipparcos* parallax. We only plot the stars with parallax errors smaller than 10%. The orange rectangle indicates the region of RC stars.

Baade's Window) show constant magnitudes as a function of colors (Figure 1.4). RC stars have been widely used as an ideal standard candle to investigate the Milky Way structure, distance to nearby galaxies, and interstellar extinction since Paczyński & Stanek (1998) presented their results.

1.2 RC stars as a standard candle

RC stars have been widely used as a standard candle after the work by Paczyński & Stanek (1998). RC stars have the advantages that they are numerous and bright in near-infrared (NIR) wavelength. On the other hand, it is difficult to identify individual RC stars. Thus, RC stars can only be used as a standard candle in the regions where a large number of RC stars exist at almost the same distance. From these characteristics, RC stars have been mainly used to investigate the Galactic center region.

The basic method to use RC stars as a standard candle is as follows. At first, the luminosity function of all red giants is constructed. Then, this luminosity function is fitted with a function of the form

$$N(\lambda) = a + bm_\lambda + cm_\lambda^2 + d \exp \left[-\frac{(m_\lambda^{RC} - m_\lambda)^2}{2\sigma_\lambda^2} \right], \quad (1.1)$$

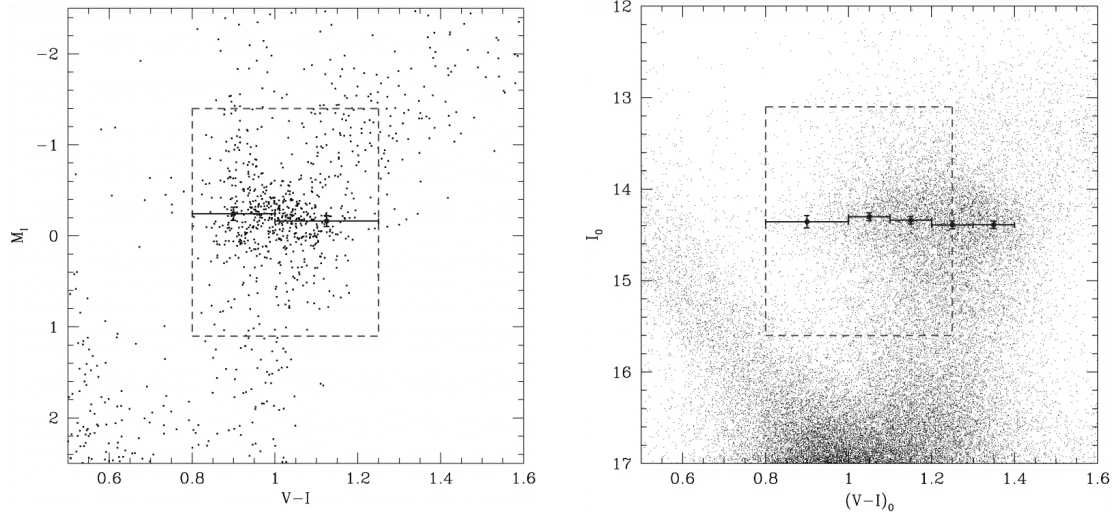


Figure 1.4: (left) The $(V - I, M_I)$ CMD of solar neighborhood. (right) The $(V - I, I)$ CMD of Baade's Window. Interstellar extinction is corrected. These figures are taken from [Paczynski & Stanek \(1998\)](#), reproduced by permission of the AAS.

where λ is a passband. The first three terms represent the background distribution of RGB stars. Some studies use different formulation as the background distribution. For example, power laws (e.g., [Stanek et al. 1997](#)), linear equations (e.g., [Paczynski & Stanek 1998](#)), or exponentials (e.g., [Nataf et al. 2015](#)) were used instead of the second-order polynomial. The Gaussian term represents the RC stars distribution, where m_λ^{RC} is the mean magnitude and σ_λ is the standard deviation of the RC stars. When the number of RC stars is small, the median values of RC stars would be used. The distance modulus μ_0 is derived from

$$\mu_0 = m_\lambda^{\text{RC}} - M_\lambda^{\text{RC}} - A_\lambda + \Delta M_\lambda^{\text{RC}}, \quad (1.2)$$

where A_λ is the interstellar extinction, and ΔM_λ is the correction of population effect. Some studies correct the population effect using theoretical models such as [Girardi & Salaris \(2001\)](#) and [Salaris & Girardi \(2002\)](#), and the others consider the population effect is small and negligible.

Before [Paczynski & Stanek \(1998\)](#), RC stars were rarely used as a standard candle. [Gardiner & Hawkins \(1991\)](#) and the series of their papers investigated the structure of the Small Magellanic Cloud (SMC). They observed the SMC using the Danish 1.5-m telescope at La Silla, and Johnson B and Gunn R filters. They found that the northeast field of the SMC has longer depth between 12 and 16 kpc, and north and northwest regions possess shorter depth between 4 and 9 kpc. [Stanek et al. \(1994, 1997\)](#) studied the V - and I -band photometry of the Optical Gravitational Lensing Experiment ([Udalski et al. 1992, 1993, 1994](#)) toward the Milky Way bulge. They considered the three types of models for the Galactic bar density distribution to fit the luminosity functions of RC

stars (Dwek et al. 1995). The first ones are the Gaussian-type (G) functions represented by

$$\rho_{G1}(x, y, z) = \rho_0 \exp(-r^2/2), \quad (1.3)$$

$$\rho_{G2}(x, y, z) = \rho_0 \exp(-r_s^2/2), \quad (1.4)$$

$$\rho_{G3}(x, y, z) = \rho_0 r^{-1.8} \exp(-r^3). \quad (1.5)$$

G1 is a Gaussian triaxial, G2 is a boxy Gaussian, and G3 is a Bahcall distribution. The second ones are the exponential-type (E) functions like

$$\rho_{E1}(x, y, z) = \rho_0 \exp(-r_e), \quad (1.6)$$

$$\rho_{E2}(x, y, z) = \rho_0 \exp(-r), \quad (1.7)$$

$$\rho_{E3}(x, y, z) = \rho_0 K_0(r_s). \quad (1.8)$$

E1 is an exponential triaxial with the form from Blitz & Spergel (1991), E2 is also an exponential triaxial but with the form from Whitelock & Catchpole (1992), and E3 is a modified spheroid. The third ones are the power-law-type (P) functions described by

$$\rho_{P1}(x, y, z) = \rho_0 \left(\frac{1}{1+r} \right)^4, \quad (1.9)$$

$$\rho_{P2}(x, y, z) = \rho_0 \frac{1}{r(1+r)^3}, \quad (1.10)$$

$$\rho_{P3}(x, y, z) = \rho_0 \left(\frac{1}{1+r^2} \right)^2, \quad (1.11)$$

where

$$r \equiv \left[\left(\frac{x}{x_0} \right)^2 + \left(\frac{y}{y_0} \right)^2 + \left(\frac{z}{z_0} \right)^2 \right]^{1/2}, \quad (1.12)$$

$$r_e \equiv \left(\frac{|x|}{x_0} + \frac{|y|}{y_0} + \frac{|z|}{z_0} \right), \quad (1.13)$$

$$r_s \equiv \left\{ \left[\left(\frac{x}{x_0} \right)^2 + \left(\frac{y}{y_0} \right)^2 \right]^2 + \left(\frac{z}{z_0} \right)^4 \right\}^{1/4}. \quad (1.14)$$

P1 is a power-law triaxial, P2 is a Hernquist profile, and P3 is a perfect ellipsoid. From the fittings of these models, they found that the power-law model P1 gave the best fit inclined to the line of sight from 20° to 30°, with axis ratios $x_0 : y_0 : z_0 = 3.5 : 1.5 : 1$ (Figure 1.5).

1.2.1 RC stars as a distance indicator

After Paczyński & Stanek (1998) demonstrated the usefulness of the RC stars as a standard candle, RC stars gained much attention. There are mainly two types of application of RC stars as a

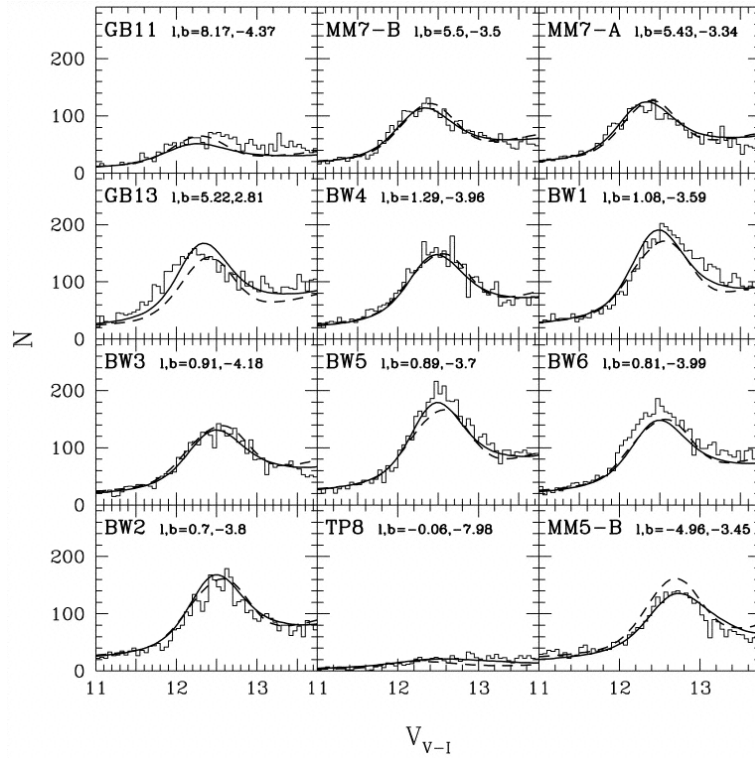


Figure 1.5: The distribution of the reddening corrected V -band magnitudes of RC stars in the Milky Way bulge regions. The best (P1, solid lines) and worst (G2, dashed line) model fits are also represented. This figure is taken from [Stanek et al. \(1997\)](#), reproduced by permission of the AAS.

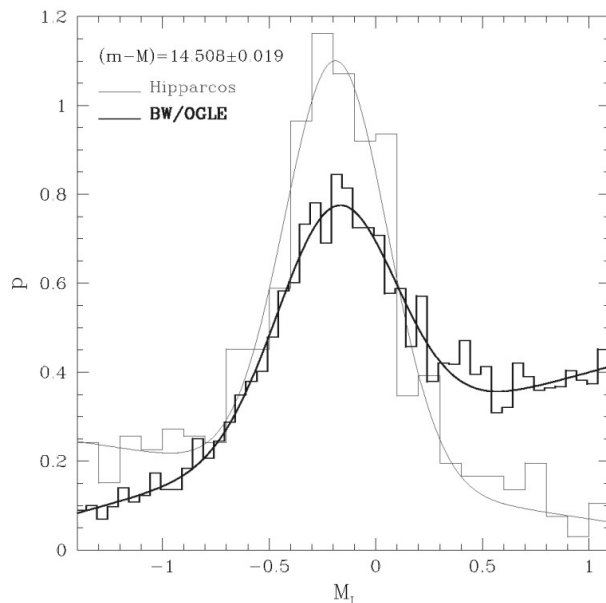


Figure 1.6: The I -band absolute magnitude distribution of RC stars in the solar neighborhood and Baade’s Window. This figure is taken from Paczyński & Stanek (1998), reproduced by permission of the AAS.

standard candle. One is a distance indicator and the other is an interstellar extinction probe. In this subsection, we introduce that RC stars have been used as a distance indicator.

Paczyński & Stanek (1998) derived the I -band absolute magnitudes of RC stars in the solar neighborhood and then applied to the RC stars in the Baade’s Window. They obtained the distance to the Galactic center as 8.4 ± 0.4 kpc by fitting equation (1.1) to the I -band magnitude distribution (Figure 1.6). Nishiyama et al. (2006b) also determined the distance to the Galactic center by the same techniques. The Infrared Survey Facility (IRSF) and Simultaneous three color InfraRed Imager for Unbiased Survey (SIRIUS) were used to obtain K_S -band magnitude. They obtained 7.52 ± 0.10 (statistical) ± 0.35 (systematic) kpc as the distance to the Galactic center and Matsunaga et al. (2013) updated this result as 8.05 ± 0.37 kpc using the recent result of NIR absolute magnitudes of RC stars by Laney et al. (2012).

The RC stars has also been used to measure the distance to the Large Magellanic Cloud (LMC). This application also contains the meaning of a test as a distance indicator because the distance to the LMC has been derived by some other methods. Some studies have been confirmed that the distance to the LMC derived from optical magnitudes of RC stars are shorter than the distance derived from other methods and widely accepted ($\mu_0 \sim 18.50$ mag). It is considered that this disagreement is caused by metallicity difference between RC stars in the solar neighborhood and the LMC (for detail, see section 1.3). For example, Udalski et al. (1998) obtained the distance modulus to the LMC of 18.08 ± 0.03 (statistical) ± 0.12 (systematic) mag from the I -band photometry from the OGLE-II

project (this result was updated as $\mu_{0,\text{LMC}} = 18.24 \pm 0.08$ mag, Udalski 2000). Stanek et al. (1998) used RC stars in the low-reddening regions and determined $\mu_{0,\text{LMC}} = 18.065 \pm 0.031$ (statistical) ± 0.09 (systematic) mag. Cole (1998) considered the population effect with the theoretical RC models (Seidel et al. 1987), and derived a larger value 18.36 ± 0.17 mag. Romaniello et al. (2000) also considered the population effect, and estimated $\mu_{0,\text{LMC}} = 18.59 \pm 0.04$ (statistical) ± 0.08 (systematic) mag from the *I*-band data of *Hubble Space Telescope* (HST). This shorter distance cannot be seen in NIR wavelengths. Alves et al. (2002) used *VIK*-band photometry and obtained the distance modulus to the LMC $\mu_{0,\text{LMC}} = 18.493 \pm 0.033$ (random) ± 0.03 (systematic) mag, and Koerwer (2009) derived $\mu_{0,\text{LMC}} = 18.54 \pm 0.06$ mag from IRSF *JH*-band photometry. However, Laney et al. (2012) obtained smaller distance $\mu_{0,\text{LMC}} = 18.38 \pm 0.03$ mag from *J*-band data, while $\mu_{0,\text{LMC}} = 18.49 \pm 0.06$ mag and $\mu_{0,\text{LMC}} = 18.475 \pm 0.021$ mag were derived from *H*- and *K*-band data. The origin of this shorter distance is also considered as the population effect because *J* – *K* color of RC stars in the LMC are bluer than those in the solar neighborhood. For the SMC, similar short distance has been derived from optical data. Udalski et al. (1998) estimated that $\mu_{0,\text{SMC}} = 18.56 \pm 0.03$ (statistical) ± 0.06 (systematic) mag. This value is also shorter than that derived from other methods (~ 18.9 mag). Cole (1998) considered the population effect and obtained large value 18.82 ± 0.20 mag.

So far, the most distant galaxy for which color-magnitude diagram shows clear RC stars is M31 (Williams et al. 2014). They conducted long time exposure using *HST*, and detected RC stars around 24.4 mag with F814W filter (Figure 1.7). Dalcanton et al. (2009) detected RC stars in further galaxies from the *HST* observations in the project of the ACS Nearby Galaxy Survey Treasury, but detailed analysis has not been done. RC stars in metal-poor dwarf galaxies in the Local Group has also been observed. Examples are Carina (Smecker-Hane et al. 1994), Leo I (Gallart et al. 1999), and Phoenix (Holtzman et al. 2000) dwarf spheroidals). Recently, the most metal-poor RC stars ($[\text{Fe}/\text{H}] = -1.8$) were observed in Leo P (McQuinn et al. 2015, Figure 1.8).

1.2.2 RC stars as the tracer of structures

One advantage of RC stars is that the number of them is very large compared to variable stars with the period-luminosity relation. Therefore, RC stars are used not only to derive the distance to objects but also to investigate the structures of objects. As described above, the earliest work that use RC stars to investigate the Milky Way structure is studies by Stanek et al. (1994, 1997). They used *I*-band magnitude and obtained the evidence for the Galactic Bar from RC luminosity variation. Nishiyama et al. (2005) discovered additional inner structure from IRSF *K_S*-band observation (Figure 1.9). They observed the region from $l = -10^\circ.5$ to $+10^\circ.5$ at $b = +1^\circ$, and divided the region into smaller grids. Then, they fitted equation (1.1) to the histograms of the dereddened *K_S*-band magnitudes (they used exponential functions for RGB background distribution). Cabrera-Lavers et al. (2008) observed outer regions of Galactic bar, and found two different bar-like structures with

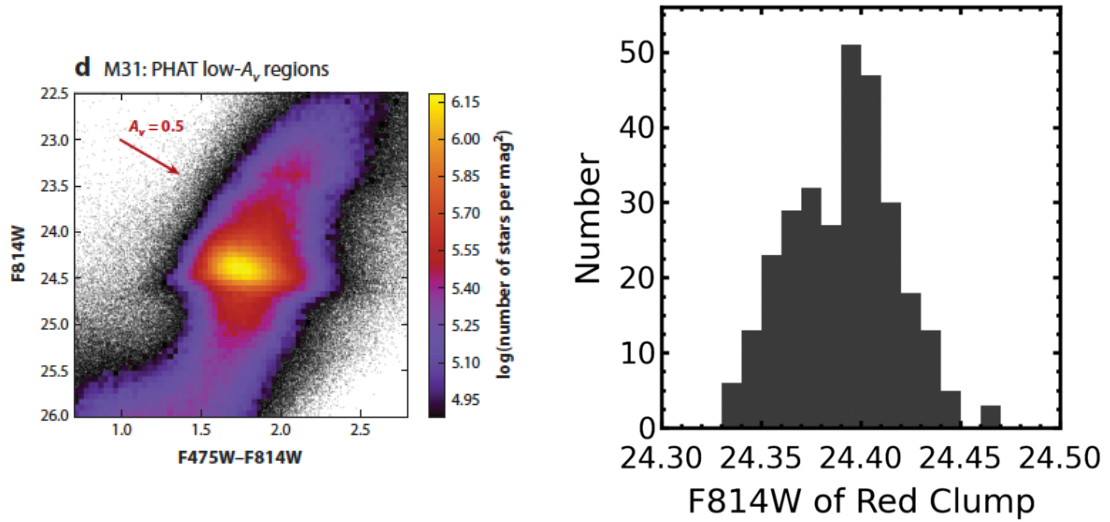


Figure 1.7: (left) The $(F475W - F814W, F814W)$ CMDs of low-reddening regions of M31. This figure is taken from [Girardi \(2016\)](#), reproduced with the permission of Annual Reviews. (right) The $F814W$ magnitude distribution around RC stars. This figure is taken from [Williams et al. \(2014\)](#), reproduced by permission of the AAS.

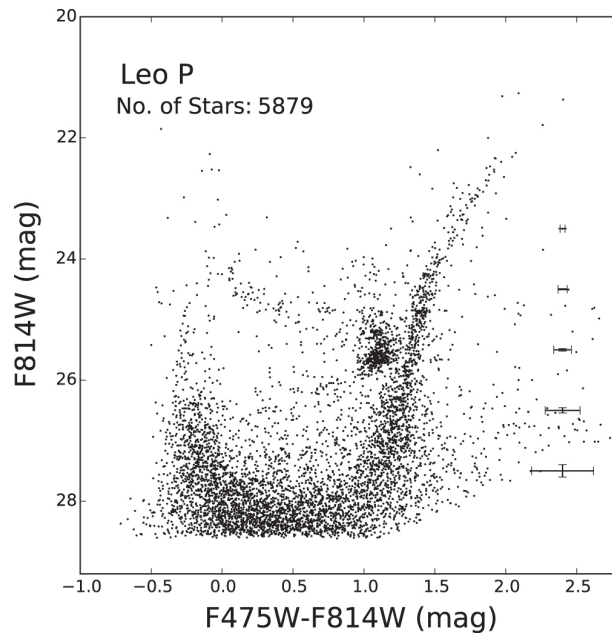


Figure 1.8: The $(F814W, F475W - F814W)$ CMD of Leo P from *HST* observation. This figure is taken from [McQuinn et al. \(2015\)](#), reproduced by permission of the AAS.

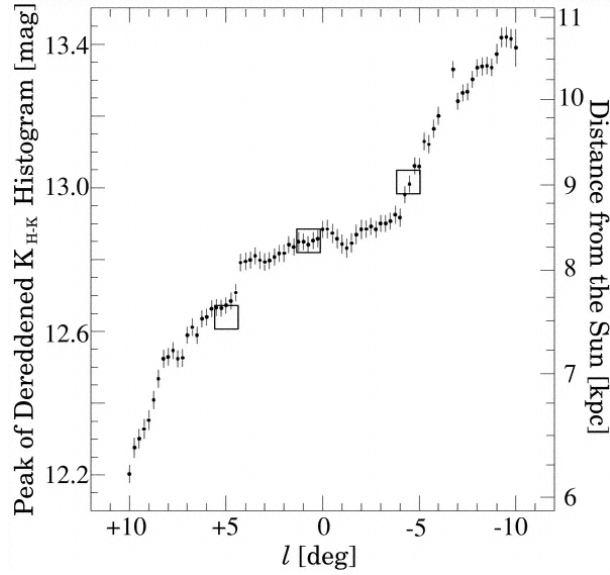


Figure 1.9: The distribution of the distance to the inner structure of the Milky Way derived from the peak of dereddened K_S -band magnitudes of RC stars. This figure is taken from [Nishiyama et al. \(2005\)](#), reproduced by permission of the AAS.

a position angle of $23^{\circ}60 \pm 2^{\circ}19$ near the Galactic center, and with a large position angle $42^{\circ}44 \pm 2^{\circ}14$ extended to $l = 28^{\circ}$ (Figure 1.10). [Gonzalez et al. \(2018\)](#) used the new photometric catalog of VISTA Variables in the Vía Láctea (VVV) survey ([Minniti et al. 2010](#)), and found that the K_S -band luminosity function has another peak in fainter magnitudes. They interpreted the secondary peaks as the spiral arm beyond the Galactic center (Figure 1.11).

In the Milky Way bulge, 0.3–0.5 mag different RC stars has been found along several Bulge lines of sight ([McWilliam & Zoccali 2010](#); [Nataf et al. 2010](#); [Li & Shen 2012](#); [Wegg & Gerhard 2013](#); [Gonzalez et al. 2015](#), Figure 1.12). These splitting magnitudes of RC stars are prominent in high-latitude regions, while they disappear around the Bulge center. The magnitude distribution of RC stars varies depending on the latitude and longitude, this RC splitting has been interpreted as evidence for an X-shaped structure seen in some extragalactic bulges based on the latitude and longitude dependence (Figures 1.13 and 1.14). From their results, RC stars at the positive longitude are bright and hence near to the Earth, while RC stars at the negative longitude are faint and distant. In the X-Z plane, the distribution of RC stars shows a clear X-shape. Furthermore, [Ness & Lang \(2016\)](#) discovered the obvious X-shape from a Wide-Field Infrared Survey Explorer (WISE) image (Figure 1.15). However, another interpretation for the RC splitting has been suggested ([Lee et al. 2015](#); [Lee & Jang 2016](#); [Joo et al. 2017](#)). They have claimed that two groups of RC magnitudes do not arise from the different distances but intrinsic RC luminosities are different. They explained that the different RC luminosities are caused by the multiple stellar populations with different

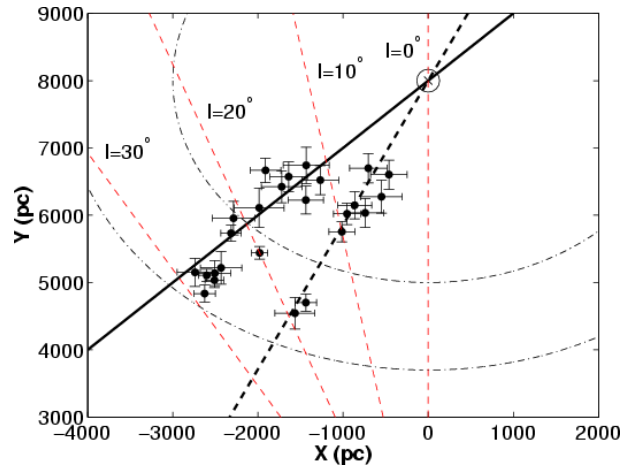


Figure 1.10: The distribution of the distance to the outer structures of the Milky Way. This figure is taken from [Cabrera-Lavers et al. \(2008\)](#), reproduced with permission from Astronomy & Astrophysics, © ESO.

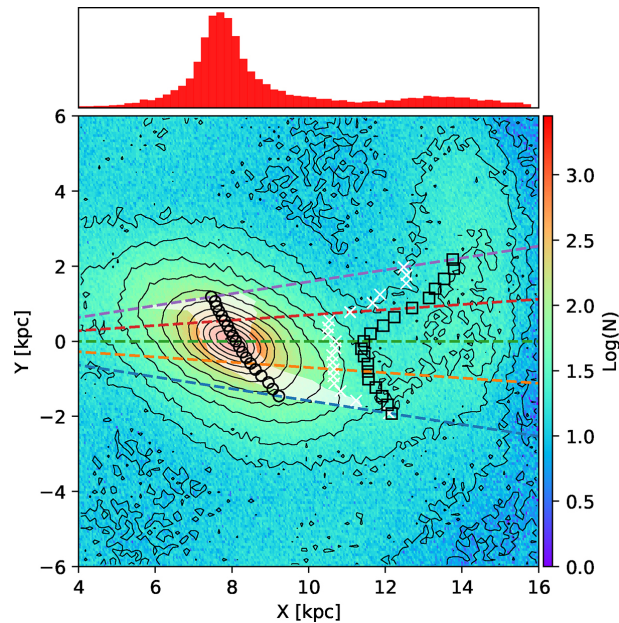


Figure 1.11: The distribution of the secondary peaks of RC stars compared with simulation. White crosses represent the secondary peak of observed RC stars. Color scale indicates the simulated density map, black circles are near structures, and black squares are far structures. The white shaded region display 1σ dispersion estimated from the width of the Gaussian fit. The upper panel represents the distance distribution for $l = +4^\circ$ estimated from the simulation. This figure is taken from [Gonzalez et al. \(2018\)](#), reproduced with the permission of Oxford University Press.

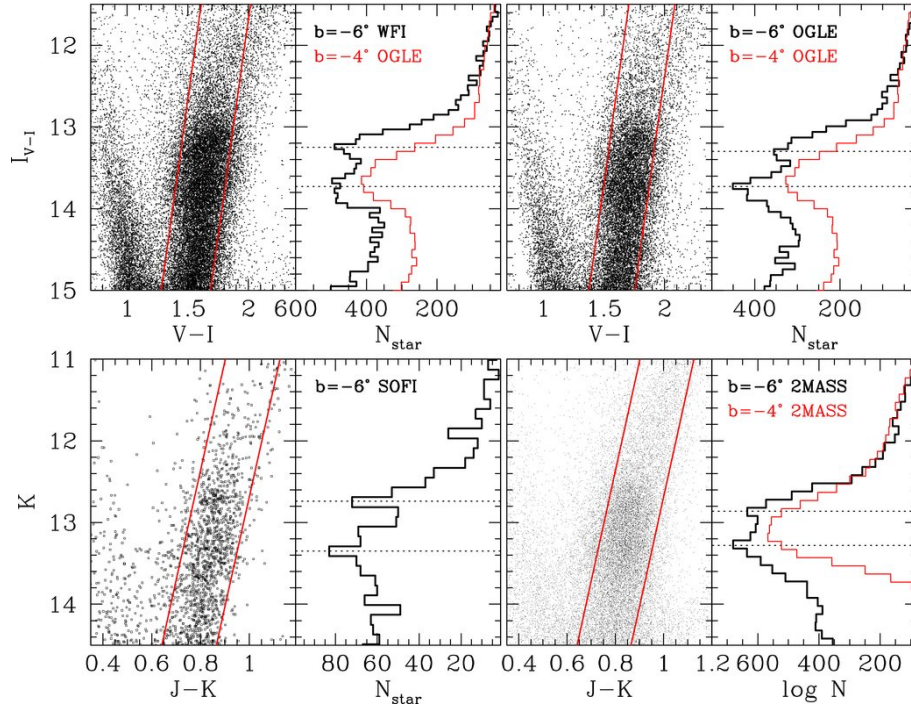


Figure 1.12: $(V - I, I)$ and $(J - K, K)$ CMDs and magnitude distribution at $(l, b) = (0, -6)$ from four photometric catalogs. (upper left) Wide Field Imager photometry at the 2.2-m ESO/MPG telescope at La Silla, for a $34' \times 33'$ field. (upper right) OGLE data from [Udalski et al. \(2002\)](#). (lower left) SOFI photometry at the New Technology Telescope in La Silla or a $8.3' \times 8.3'$ field. (lower right) 2MASS PSC. This figure is taken from [McWilliam & Zoccali \(2010\)](#), reproduced by permission of the AAS.

ages, metallicities, and helium abundances as observed in some globular clusters ([Lee et al. 1999](#); [Ferraro et al. 2009](#); [Gratton et al. 2012](#); [Renzini et al. 2015](#); [Bastian & Lardo 2018](#), Figure 1.16). In addition, [Han & Lee \(2018\)](#) asserted that the X-shape structure seen in the WISE image is an artificial structure caused by two problems: interstellar extinction is not considered, and an ellipsoidal bulge model is applied. It is well-known that the Milky Way has a boxy bulge ([Dwek et al. 1995](#); [López-Corredoira et al. 2005](#); [Gonzalez et al. 2013](#)). When an ellipsoidal bulge model is subtracted from a boxy bulge, an artificial X-shape structure will appear in the residual. The same problem is well-known for the studies of extragalaxies ([Peng et al. 2011](#); [Cho et al. 2016](#)).

For the LMC, [Koerwer \(2009\)](#) investigated the inclination, i , and the position angle of the line of nodes, ϕ from the IRSF/SIRIUS JH -band photometry of the IRSF Magellanic Clouds Point Source Catalog ([Kato et al. 2007](#)). He divided $\sim 40 \text{ deg}^2$ survey area into small regions, and searched for the peak of luminosity functions. As a result, he obtained $i = 23^\circ.5 \pm 0^\circ.4$ and $\phi = 154^\circ.6 \pm 1^\circ.2$ as the best-fit plane (Figure 1.17). [Gardiner & Hawkins \(1991\)](#) studied the depth of the SMC as described above.

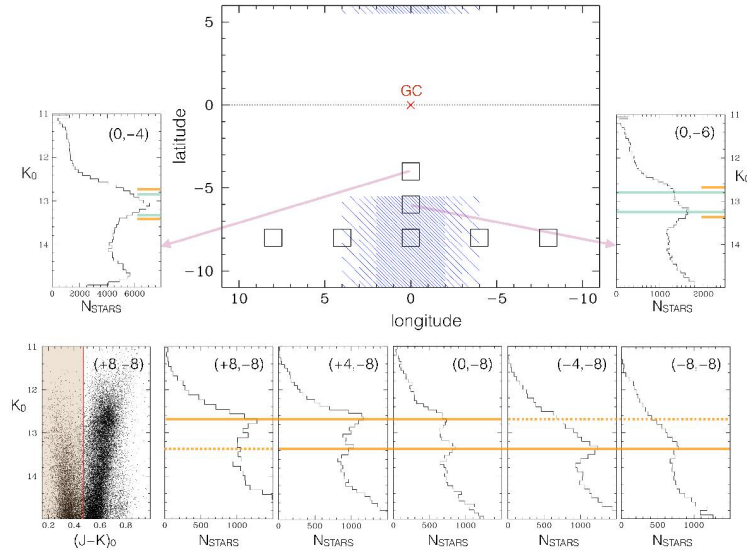


Figure 1.13: The difference of luminosity functions for several regions around Milky Way Bulge. This figure is taken from [Gonzalez et al. \(2015\)](#), reproduced with permission from Astronomy & Astrophysics, © ESO.

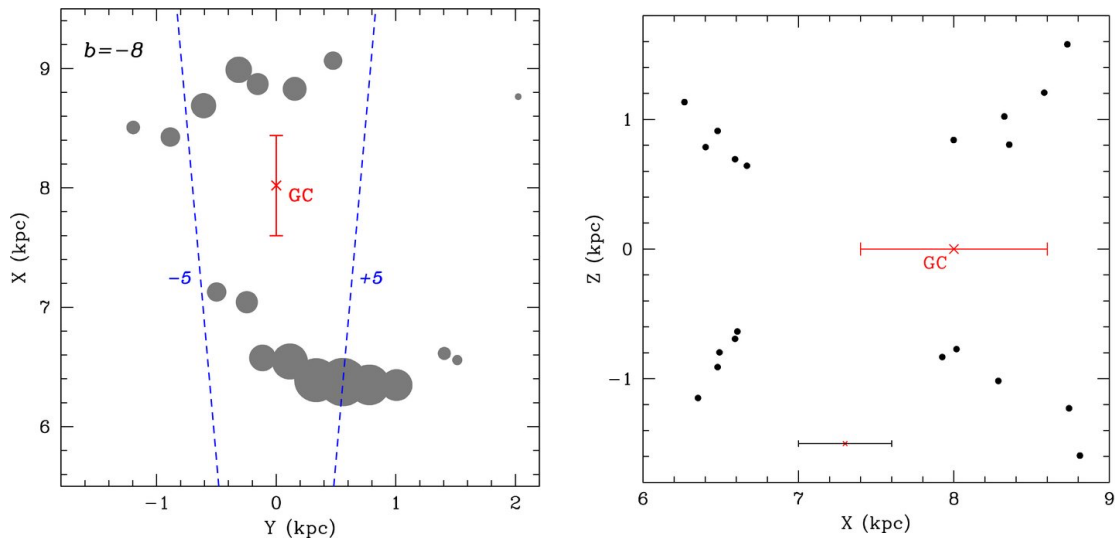


Figure 1.14: (left) The distance of RC stars derived from luminosity functions in the $b = -8^\circ$ plane from $l = -9^\circ$ to $l = 14^\circ$. Point sizes represent the number of RC stars. (right) The distance of RC stars in the X-Z plane. These figures are taken from [McWilliam & Zoccali \(2010\)](#), reproduced by permission of the AAS.

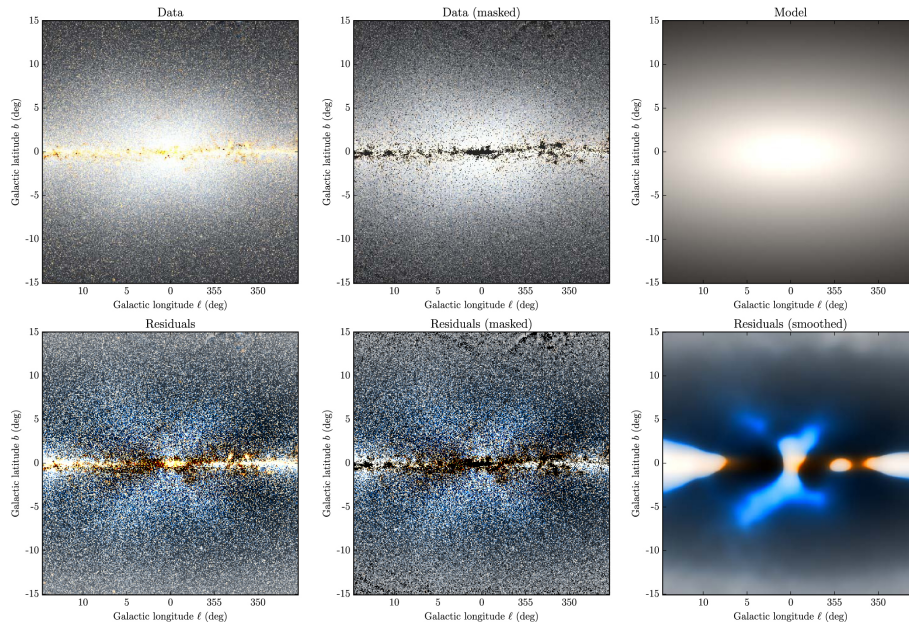


Figure 1.15: The image of Milky Way Bulge obtained from *WISE* *W1* and *W2* images. (upper left) *WISE* image (upper center) *WISE* image masked for the top and bottom 5 per cent of pixels based on $W1 - W2$ color and with pixels with negative flux. (upper right) exponential disk model (lower left) disk subtracted *WISE* image (lower center) disk subtracted and masked *WISE* image (lower right) Smoothed version of lower center image. These figures are taken from [Ness & Lang \(2016\)](#), reproduced by permission of the AAS.

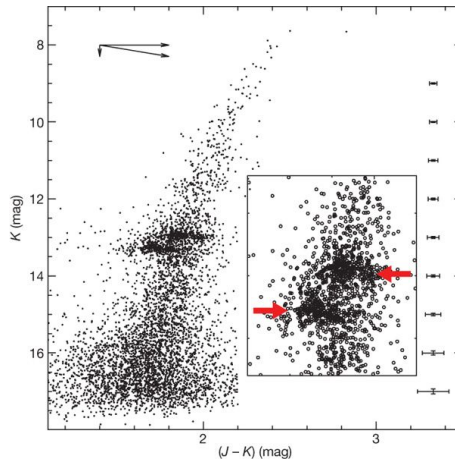


Figure 1.16: The $(K, J - K)$ CMD of the central region of a globular cluster, Terzan 5. The small panel is the same plot as the main panel but magnified around RC stars. This figure is taken from [Ferraro et al. \(2009\)](#), reproduced with permission from Springer Nature.

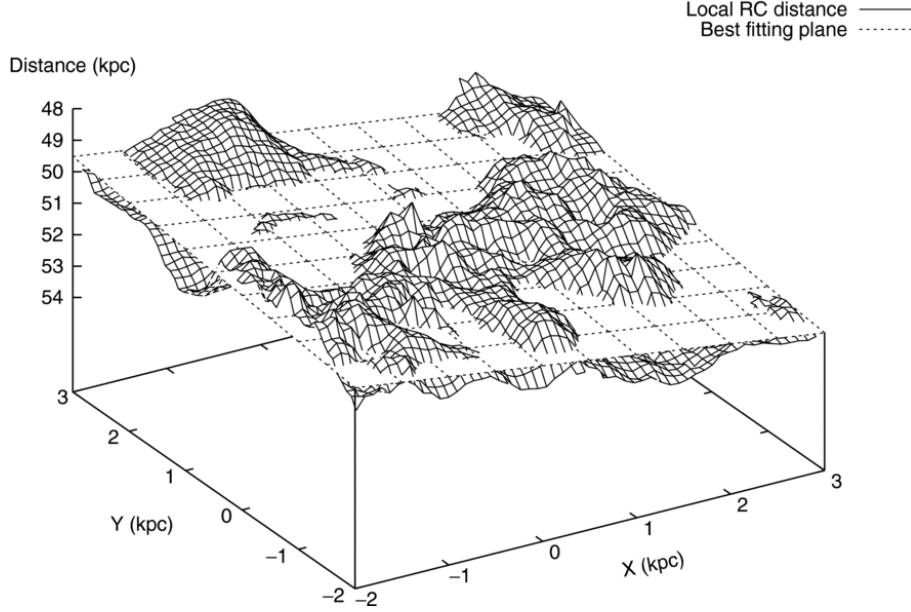


Figure 1.17: The distance distribution of RC stars in the LMC, and the best-fit plane. Up is nearer to the Earth. North is in the direction of positive Y , and west is in the direction of positive X . This figure is taken from Koerwer (2009), reproduced by permission of the AAS.

1.2.3 RC stars as a interstellar extinction probe

Taking advantage of the large quantities, RC stars has also been used as an interstellar extinction probe. To investigate the interstellar extinction law, the color-difference method has widely used. In the color-difference method, the extinction curves are obtained in the form of the ratios of color excesses $E_{\lambda-\lambda_1}/E_{\lambda_2-\lambda_1}$. Customarily, V - and B -band has been used as λ_1 and λ_2 , respectively. Using the absolute extinction A_λ , the ratios of color excesses are written as

$$\frac{E_{\lambda-V}}{E_{B-V}} = \frac{A_\lambda}{E_{B-V}} - \frac{A_V}{E_{B-V}} = \frac{A_\lambda}{E_{B-V}} - R_V, \quad (1.15)$$

where R_V is so-called the ratio of total to selective extinction ratio defined by

$$R_V \equiv \frac{A_V}{E_{B-V}}. \quad (1.16)$$

This means that if R_V is given, we can obtain A_λ from observing color excesses. The color excesses can be obtained by comparing reddened colors with intrinsic colors, and intrinsic colors are derived from the spectral types of stars. However, we cannot directly obtain R_V from observable data. Instead, the extrapolation of the extinction curve to $\lambda^{-1} = 0$ has been used. To estimate R_V , observations at longer wavelengths have been performed but there are two uncertainty sources for these observations: contamination by dust emission and the possible existence of neutral extinction by grains much larger than observing wavelengths.

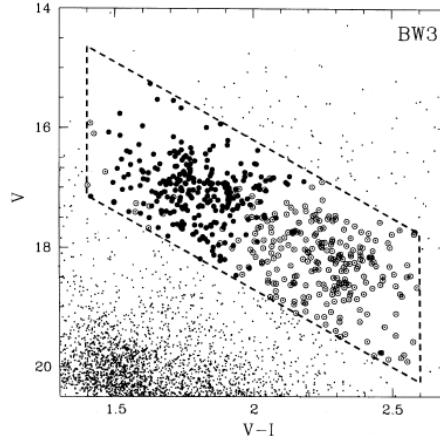


Figure 1.18: The $(V, V - I)$ CMD for a field in the Baade's Window. Different symbols represent the different level of extinction: (open circles) highest (filled circles) lowest. This figure is taken from [Wozniak & Stanek \(1996\)](#), reproduced by permission of the AAS.

To avoid the uncertainty, so-called RC method was developed [Wozniak & Stanek \(1996\)](#). The RC method uses the nature of RC stars that occupy a small region in the CMD if they are not suffered from interstellar extinction. In the RC method, three assumptions are needed: age and metallicity dependence of the absolute magnitudes of RC stars is small, distance to the RC stars is the same, and extinction laws are the same in a region used to make a CMD. When the assumption is reasonable, RC stars are located in a straight line with a slope of $R_\lambda = A_\lambda / E_{\lambda'-\lambda}$ (Figure 1.18). Unlike the color-difference method, we can directly obtain R_λ from the RC method.

[Wozniak & Stanek \(1996\)](#) use the RC method to investigate the coefficient of the selective extinction for the first time with OGLE data for the Milky Way Bulge. They obtained nearly constant values as A_V / E_{V-I} for 13 fields ranging from -5° to $+5^\circ$, and the weighted mean of the value is 2.44 (Figure 1.19). [Udalski \(2003\)](#) used OGLE data and found that the slope of reddening line is significantly smaller than that expected from the standard extinction law ([Cardelli et al. 1989](#); [Fitzpatrick 1999](#), Figure 1.20). In infrared wavelengths, [Nishiyama et al. \(2006a\)](#) observed Galactic center regions ($|l| \lesssim 2^\circ$ and $0^\circ.5 \lesssim |b| \lesssim 1^\circ$) with IRSF/SIRIUS. They obtained that $A_J : A_H : A_{K_S} = 1 : 0.573 \pm 0.009 : 0.331 \pm 0.004$ and $E_{J-H} / E_{H-K_S} = 1.72 \pm 0.04$. Also, they found the steeper power law $A_\lambda \propto \lambda^{-1.99}$ in infrared compared with [Rieke & Lebofsky \(1985, \$A_\lambda \propto \lambda^{-1.54}\$ \)](#) or [Cardelli et al. \(1989, \$A_\lambda \propto \lambda^{-1.61}\$ \)](#), and a small variation across the survey regions. [Nishiyama et al. \(2008\)](#) added the OGLE V -band data, and discovered that $A_V : A_J : A_H : A_{K_S} = 1 : 0.188 : 0.108 : 0.062$. The obtained ratio $A_{K_S} / A_V \sim 1/16$ is much smaller than that usually used ($A_{K_S} / A_V \sim 1/10$). [Nishiyama et al. \(2009\)](#) extended the study to longer wavelengths to $8.0 \mu\text{m}$ using RC stars and upper RGB stars from *Spitzer Space Telescope* Legacy program, Galactic Legacy Infrared Mid-Plane Survey Extraordinaire II. They derived that

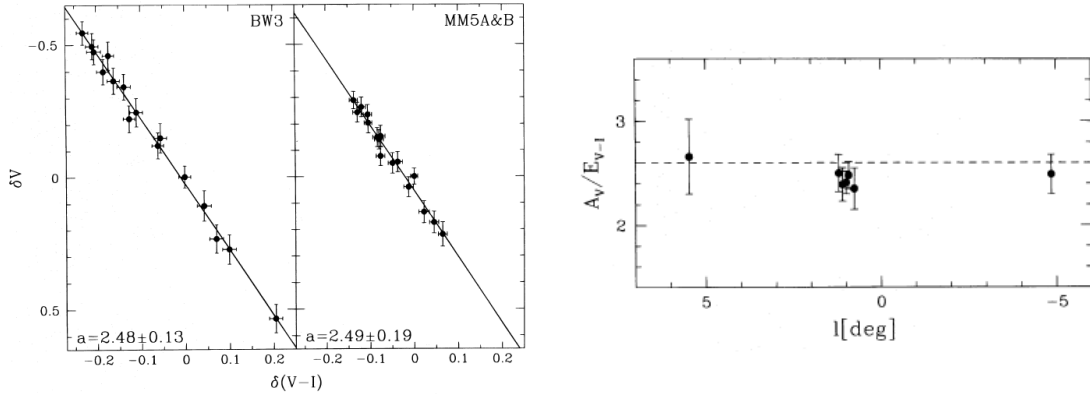


Figure 1.19: (left) The distribution of reddened RC stars in $(V - I, V)$ for two regions at $l = 0^\circ.923$ (BW3) and $l = -4^\circ.853$ (MM5). The solid line indicates the least-squares fit to the distribution. (right) The values of A_V/E_{V-I} for some regions with different Galactic longitude. These figures are taken from [Wozniak & Stanek \(1996\)](#), reproduced by permission of the AAS.

$A_J : A_H : A_{K_S} : A_{[3.6]} : A_{[4.5]} : A_{[5.8]} : A_{[8.0]} = 3.02 : 1.73 : 1 : 0.50 : 0.39 : 0.36 : 0.43$, and confirmed that the extinction curve becomes flat at $\lambda \gtrsim 3 \mu\text{m}$ (Figure 1.21). [Nataf et al. \(2013\)](#) combined OGLE-III V - with I -band data with VVV and 2MASS data, and discovered that the I -band extinction is well fitted by $A_I = 0.7465 \times E(V - I) + 1.3700 \times E(J - K_S)$. Recently, [Alonso-García et al. \(2017\)](#) obtained a much steeper power law $A_\lambda \propto \lambda^{-2.47}$ compared with [Nishiyama et al. \(2006a, 2009\)](#) from the VVV survey.

RC stars has also been used to create extinction maps. [Stanek \(1996\)](#) applied the RC method to the $40' \times 40'$ of Baade's Window using the OGLE data, and constructed an extinction map with resolution of $\sim 30''$ (Figure 1.22). [Sumi \(2004\)](#) conducted more precise investigation of the OGLE data for wider regions, and presented the reddening map for 11 deg^2 (Figure 1.23). [Gonzalez et al. \(2018\)](#) used the photometric catalog of VVV survey and constructed the reddening map for the region $-10^\circ < l < 10^\circ$ and $-1.5^\circ < b < 1.5^\circ$ in NIR wavelengths (Figure 1.24).

Extinction maps have also been constructed for the LMC. [Subramaniam \(2005\)](#) utilized the OGLE-II V - and I -band photometry to create the reddening map for the bar region of the LMC (Figure 1.25). [Haschke et al. \(2011\)](#) constructed extinction maps of both LMC and SMC using OGLE-III photometric data (Figure 1.26). [Tatton et al. \(2013\)](#) investigated 30 Dor region suffered from the strongest interstellar extinction is the LMC using the VISTA near-infrared YJK_S Public Survey of the Magellanic Clouds system (VMC survey, [Cioni et al. 2011](#), Figure 1.27).

1.3 Absolute magnitudes of RC stars

[Paczyński & Stanek \(1998\)](#) stated that distance determination with stars suffer from at least four problems.

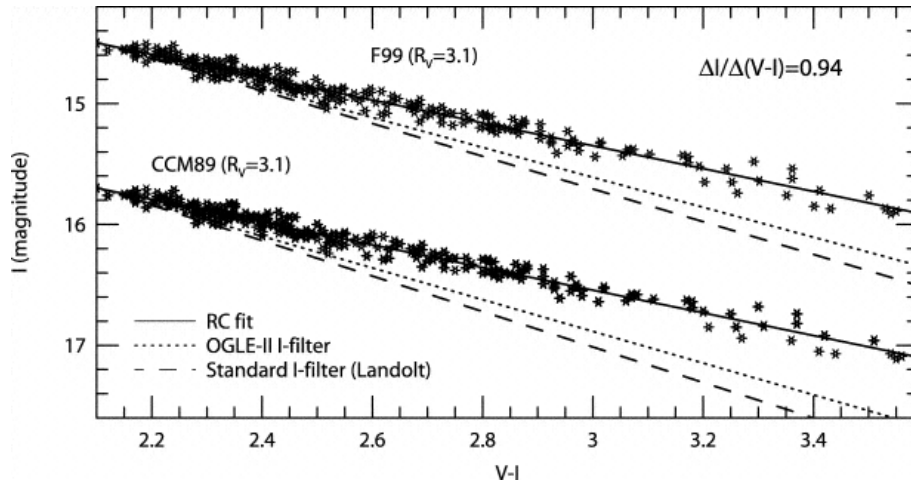


Figure 1.20: The location of the peak magnitudes of RC stars in $(I, V - I)$ CMD. Solid lines represent the best-fit for observational data, dotted lines represent the standard extinction laws for OGLE-II I -band filter, and dashed lines represent the standard extinction laws for Landolt I -band filter. Lower lines indicate [Cardelli et al. \(1989\)](#), and upper lines indicate [Fitzpatrick \(1999\)](#). This figure is taken from [Udalski \(2003\)](#), reproduced by permission of the AAS.

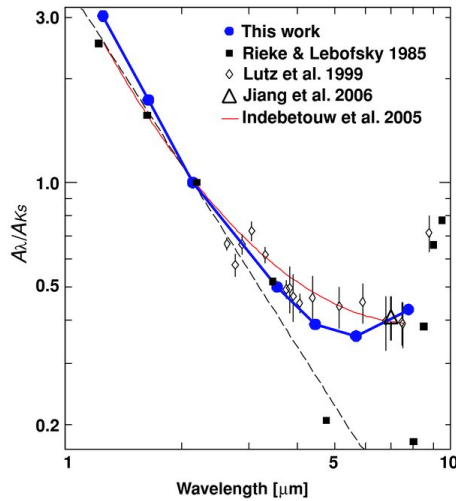


Figure 1.21: Extinction ratios (A_λ/A_{K_S}) toward the Galactic center regions as a function of wavelength. Some previous studies are also shown. This figure is taken from [Nishiyama et al. \(2009\)](#), reproduced by permission of the AAS.

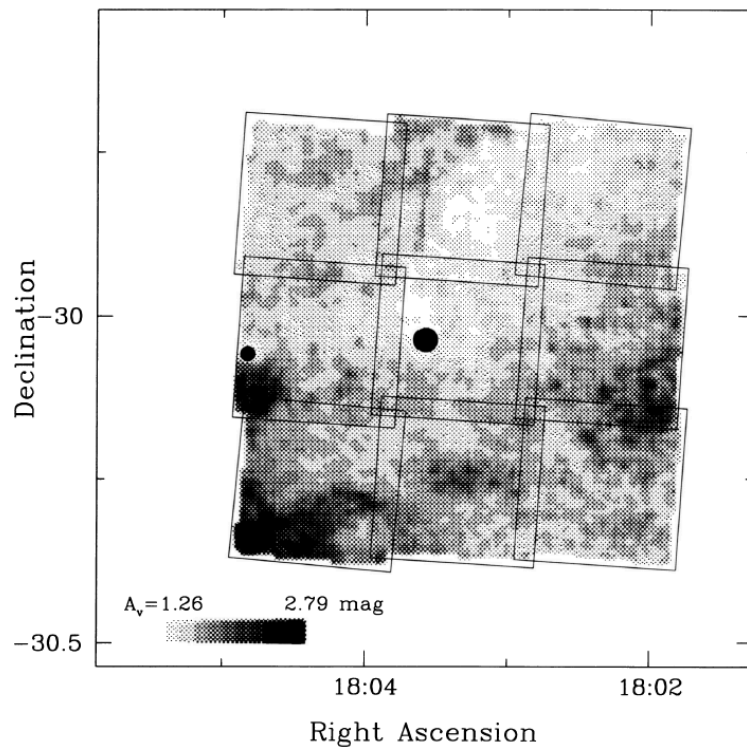


Figure 1.22: An extinction map toward Baade's Window. The strength of the interstellar extinction A_V is represented by gray scale. Two filled circles indicate the globular clusters NGC 6528 (left) and NGC 6522 (right). This figure is taken from [Stanek \(1996\)](#), reproduced by permission of the AAS.

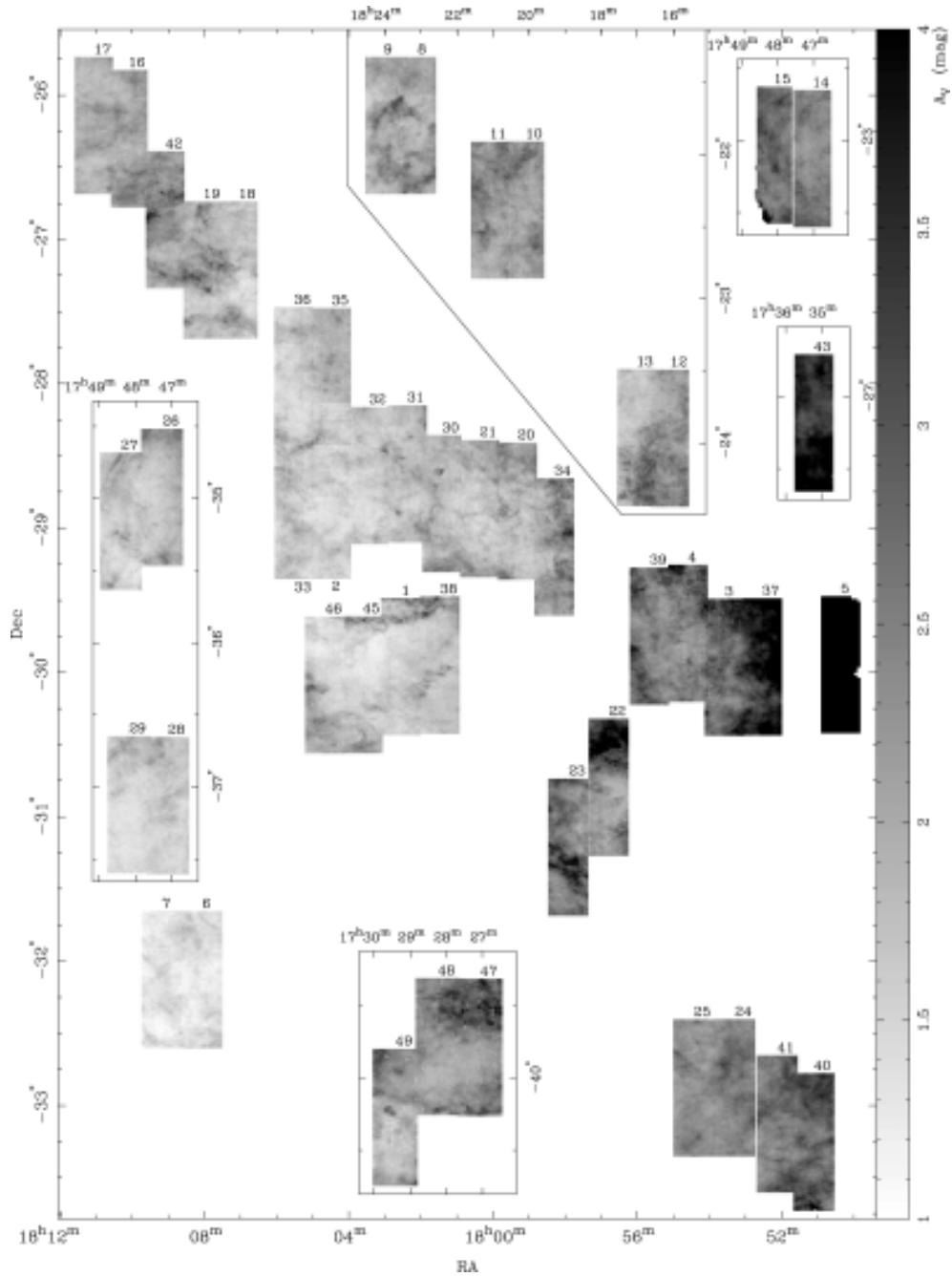


Figure 1.23: A_V extinction map for the Milky Way bulge. The strength of the interstellar extinction A_V is represented by gray scale. This figure is taken from [Sumi \(2004\)](#), reproduced with the permission of Oxford University Press.

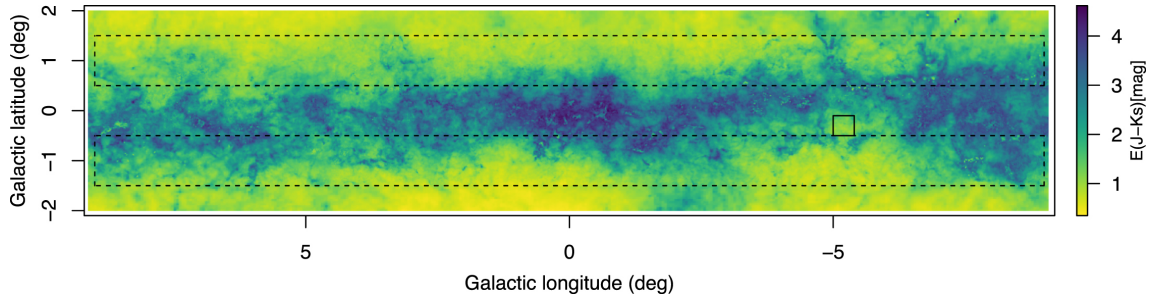


Figure 1.24: A reddening map for the Milky Way bulge, $-10^\circ < l < 10^\circ$ and $-2^\circ 0 < b < 2^\circ 0$. Dashed boxes represent the regions analyzed by [Gonzalez et al. \(2018\)](#). This figure is taken from [Gonzalez et al. \(2018\)](#), reproduced with the permission of Oxford University Press.

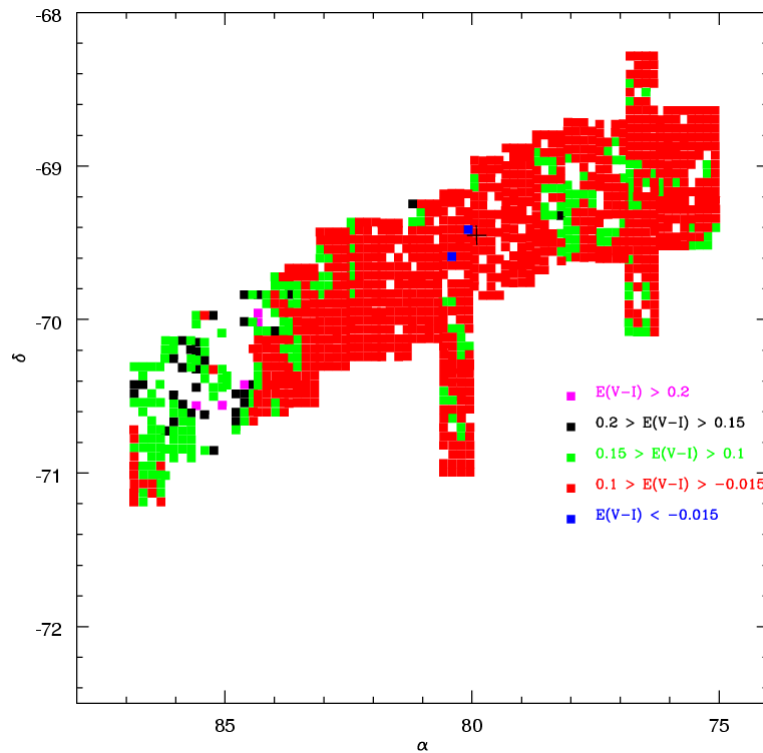


Figure 1.25: The reddening map of the bar region of the LMC. The strength of reddening is presented by some different colors. The center of the LMC is displayed by the plus sign. This figure is taken from [Subramaniam \(2005\)](#), reproduced with permission from Astronomy & Astrophysics, © ESO.

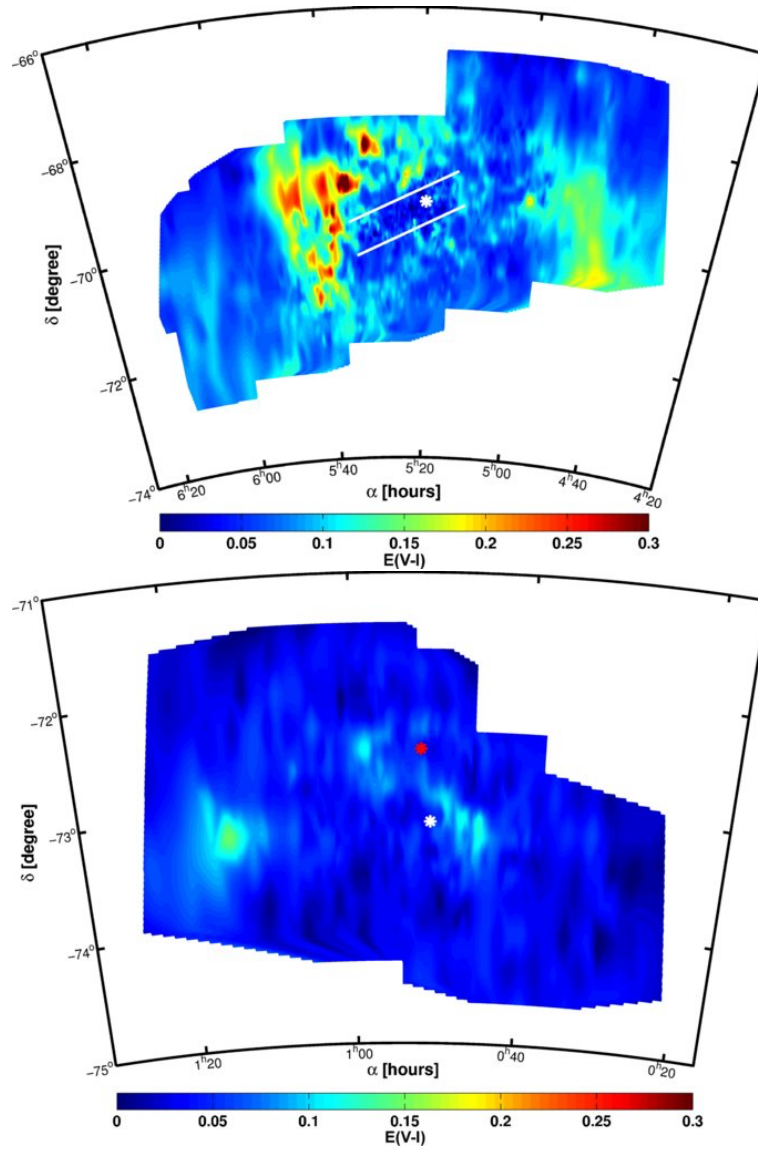


Figure 1.26: (top) The reddening map of the LMC. The strength of the reddening is shown as color scale. Two white lines indicate the bar region. The asterisk represent the center of the LMC. (bottom) The reddening map of the SMC. The strength of the reddening is shown as color scale. The asterisk represent the center of the SMC. These figures are taken from [Haschke et al. \(2011\)](#), reproduced by permission of the AAS.

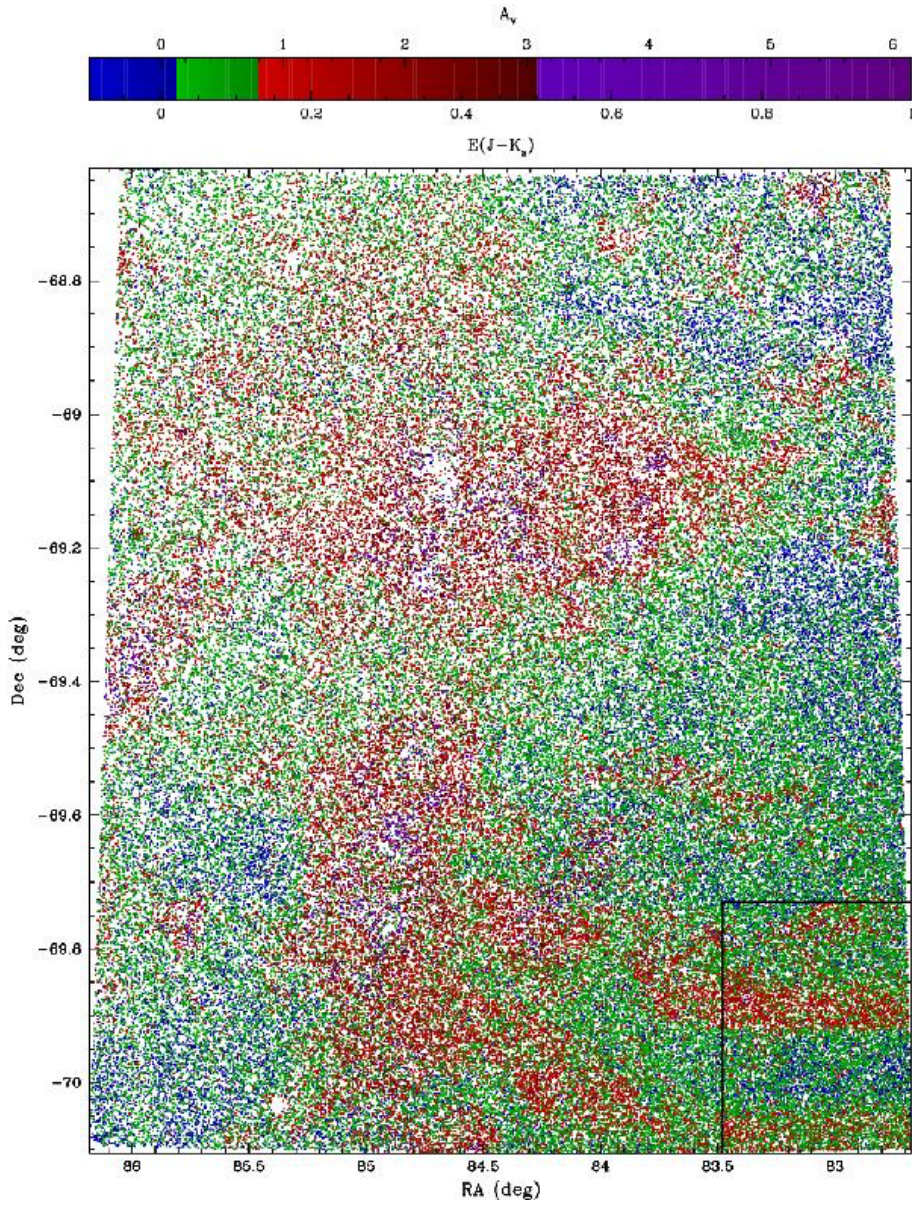


Figure 1.27: An extinction map toward 30 Dor in the LMC. The strength of the extinction is presented by color scale. This figure is taken from [Tatton et al. \(2013\)](#), reproduced with permission from Astronomy & Astrophysics, © ESO.

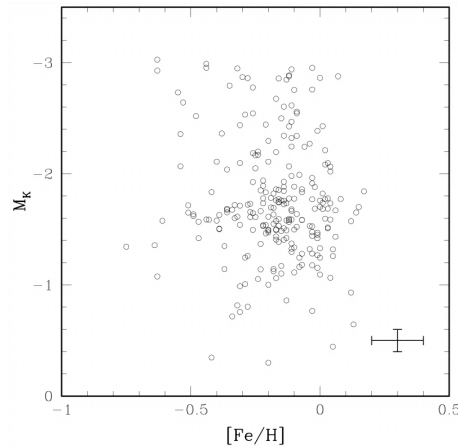


Figure 1.28: K -band absolute magnitudes as a function of $[\text{Fe}/\text{H}]$ for the 238 RC stars with *Hipparcos* parallaxes. Cross in the lower right is the typical error bar. This figure is taken from [Alves \(2000\)](#), reproduced by permission of the AAS.

1. The accuracy of absolute magnitudes for the nearby stars
2. Interstellar extinction must be determined
3. The mass, age, and metallicity dependence of absolute magnitude (population effect)
4. The statistical error

RC stars are the only type of stars that overcome the fourth problem because the number of them is numerous, contrary to the variable stars with the period-luminosity relation, such as Cepheid, RR Lyrae, and Mira variables.

When RC stars came into use as a standard candle, the population effect was considered to be small especially in longer wavelengths (not much suffered from the third problem). [Paczynski & Stanek \(1998\)](#) claimed that I -band magnitudes of RC stars showed no color dependence, and thus population effect is small (Figure 1.4). [Alves \(2000\)](#) investigated the metallicity dependence of the K -band absolute magnitudes of RC stars with compiling many previous work (mainly from the Caltech Two Micron Sky Survey, TMSS), *Hipparcos* parallaxes, and $[\text{Fe}/\text{H}]$ from high-resolution spectroscopic data, and confirmed small metallicity dependence (Figure 1.28). Interstellar extinction is also small in K -band, and the second problem should be minimized.

However, it came to be recognized that the population effect cannot be ignored to use them as an excellent standard candle, as both theoretical and observational research on the RC stars has proceeded. From theoretical side, [Girardi & Salaris \(2001\)](#) investigated the population effects on the V - and I -band absolute magnitudes, and [Salaris & Girardi \(2002\)](#) studied the effects in the K -band (Figure 1.29). They determined absolute magnitudes of RC stars using evolutionary

tracks and isochrones from [Girardi et al. \(2000\)](#). They calculated the mean magnitudes of RC stars ($\langle M_\lambda \rangle$) for a given isochrone of age and metallicity (t, Z) using the following equation

$$\langle M_\lambda(t, Z) \rangle = -2.5 \log \left[\frac{1}{N_{\text{RC}}(t, Z)} \int^{\text{CHeB}} \phi(m_i) 10^{-0.4M_\lambda} dm_i \right], \quad (1.17)$$

where M_λ is the absolute magnitude of each filter, $\phi(m_i)$ is the Salpeter initial mass function, and m_i is the initial mass of each star. N_{RC} is the number of RC stars per unit mass and is calculated by

$$N_{\text{RC}}(t, Z) = \int^{\text{CHeB}} \phi(m_i) dm_i. \quad (1.18)$$

From their results, the longer the wavelength, the smaller the dependence of absolute magnitude on metallicity, and it does not depend much on metallicity in NIR wavelengths except for very metal-poor RC stars. Meanwhile, they predict that the age dependence of the absolute magnitude is not simple such that there is only weak age dependence for RC stars older than 2 Gyr, but there is strong age dependence for RC stars younger than 2 Gyr.

Many observational studies have confirmed small metallicity dependence of NIR magnitudes of RC stars. As described above, [Alves \(2000\)](#) verified the small metallicity dependence in the K -band

$$M_K = (0.57 \pm 0.36)[\text{Fe}/\text{H}] - (1.64 \pm 0.07). \quad (1.19)$$

We note that only low mass star with relatively high metallicity ($[\text{Fe}/\text{H}] \gtrsim -1.5$) can evolve to RC stars. [Groenewegen \(2008\)](#) investigated I - and K_S -band metallicity dependence using revised *Hipparcos* parallaxes, photometric data from TMSS, the Deep Near Infrared Survey of the Southern Sky (DENIS), and the Two Micron All Sky Survey (2MASS) point source catalog (PSC), and spectroscopic $[\text{Fe}/\text{H}]$ values from various work. They confirmed marginal metallicity dependence of I -band absolute magnitude ($(0.08 \pm 0.07)([\text{Fe}/\text{H}] + 0.15)$) and no metallicity dependence of K_S -band absolute magnitude (Figure 1.30). [Laney et al. \(2012\)](#) retook JHK -band magnitudes for the RC stars studied by [Alves \(2000\)](#) using 0.75-m telescopes at the Southern African Astronomical Observatory and Mk II infrared photometer. They found no significant trend in H - and K -band absolute magnitudes with metallicity at least for stars with $[M/\text{H}]$ higher than -0.6 (Figure 1.31). [Grocholski & Sarajedini \(2002\)](#) and [van Helshoecht & Groenewegen \(2007\)](#) investigated RC stars in the Milky Way star clusters with 2MASS PSC, and negligible metallicity dependence of K -band absolute magnitude for RC stars with $-0.5 < [\text{Fe}/\text{H}] < 0.4$ (Figure 1.32).

On the other hand, age dependence has not been investigated extensively because it is difficult to know the ages of RC stars. So far, the studies are limited to the work using Milky Way star clusters or age that derived from asteroseismology. [Grocholski & Sarajedini \(2002\)](#) studied the RC stars in the Milky Way star clusters as described above, and little age dependence of K -band absolute magnitude with $10^{9.2} < \text{Age} < 10^{9.9}$, but relatively strong age dependence was seen in RC stars younger than ~ 2 Gyr as the theoretical model predicted. [van Helshoecht & Groenewegen](#)

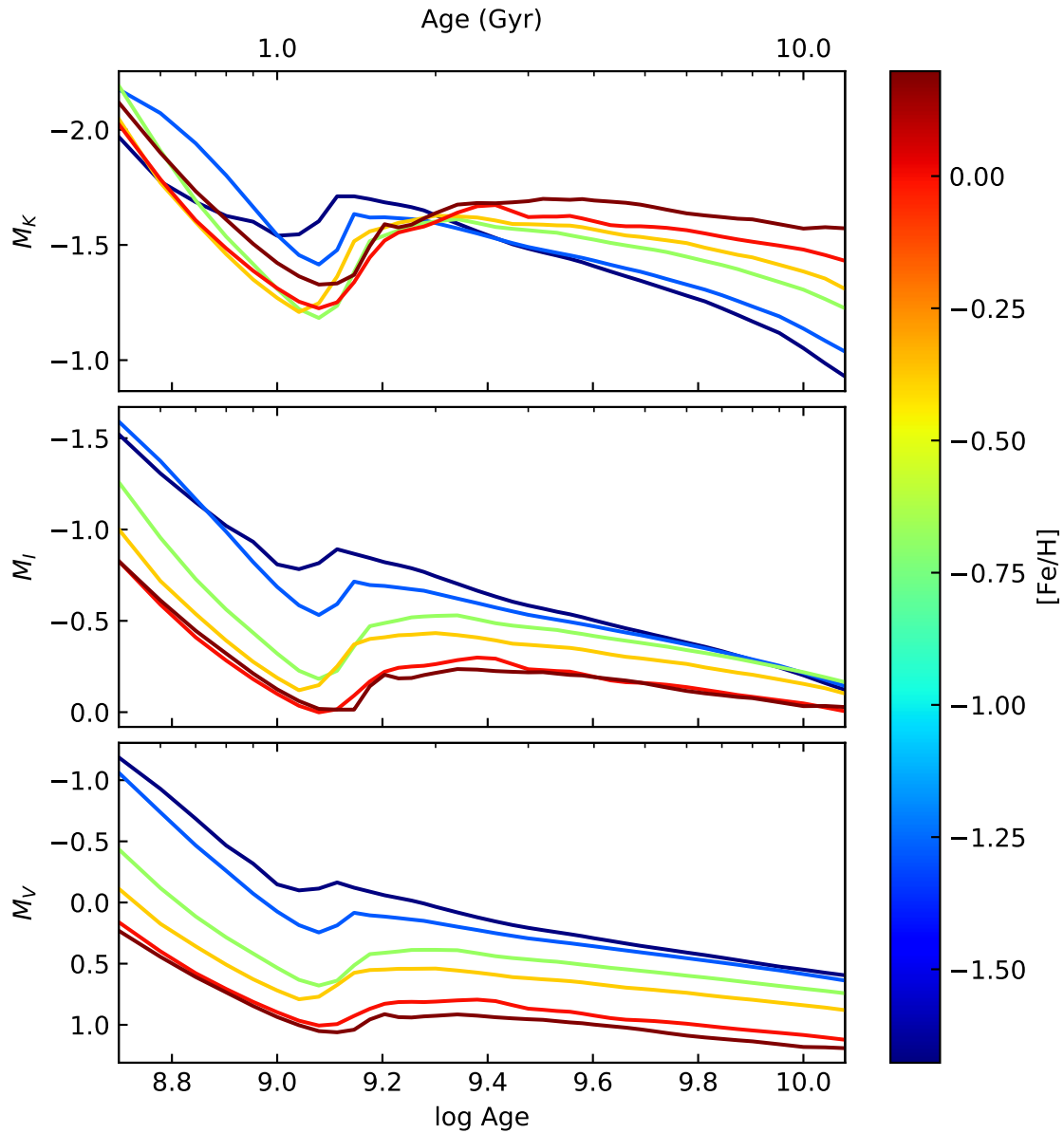


Figure 1.29: Model predictions for the absolute magnitudes of RC stars as a function of age for several metallicities (top: K -band, middle: I -band, bottom: V -band). The different colors represent the difference of metallicities (from black to brown, $[Fe/H] = -1.68, -1.28, -0.68, -0.38, 0.00,$ and 0.20). The data of the top panel is taken from [Salaris & Girardi \(2002\)](#), and the data of the middle and bottom panels are taken from [Girardi & Salaris \(2001\)](#).

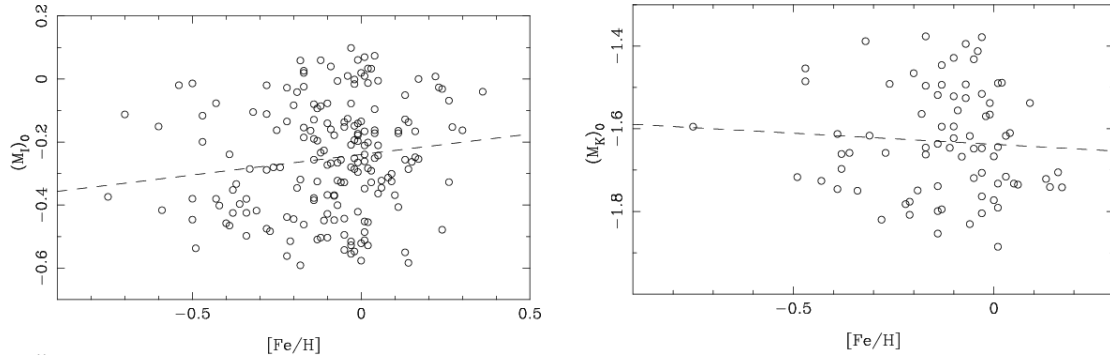


Figure 1.30: M_I (left) and M_K (right) as a function of $[\text{Fe}/\text{H}]$. The dashed lines represent the best-fit ($M_I = (0.08 \pm 0.07)([\text{Fe}/\text{H}] + 0.15)$). The best-fit relation for M_K is not described in [Groenewegen \(2008\)](#). These figures are taken from [Groenewegen \(2008\)](#), reproduced with permission from Astronomy & Astrophysics, © ESO.

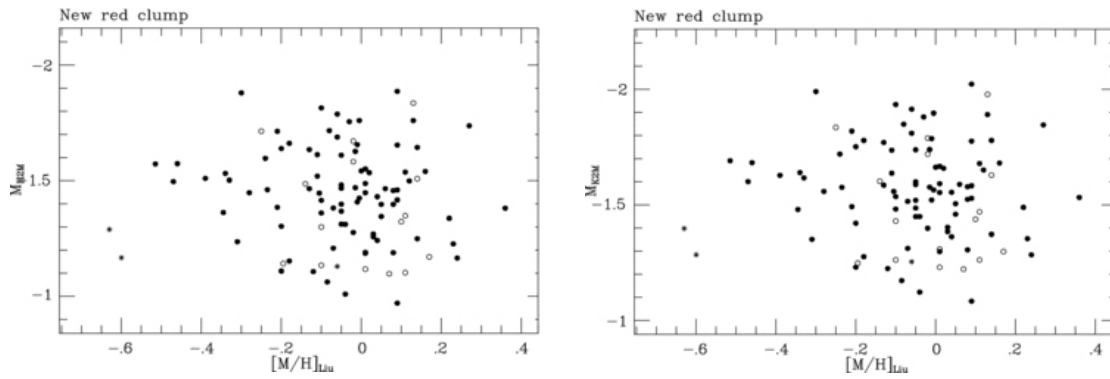


Figure 1.31: M_H (left) and M_K (right) versus $[\text{Fe}/\text{H}]$ for the 226 RC stars. Filled circles indicate the RC stars with five astrometric parameters, and open circles represent the other RC stars. These figures are taken from [Laney et al. \(2012\)](#), reproduced with the permission of Oxford University Press.

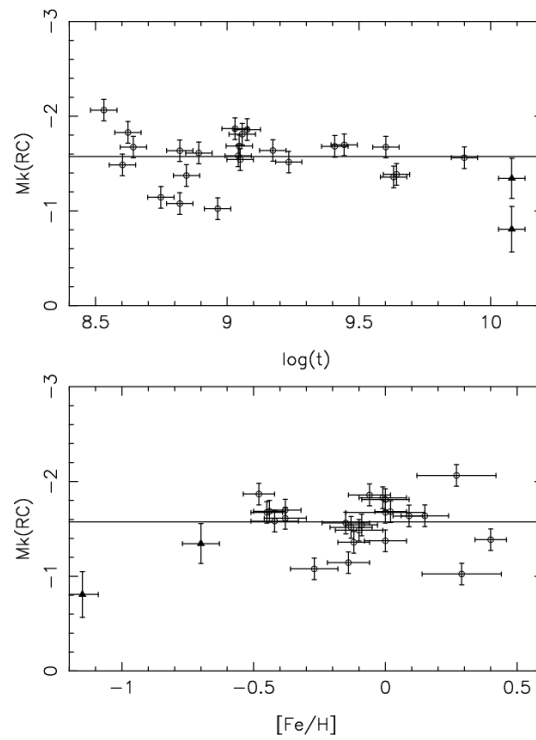


Figure 1.32: K -band absolute magnitudes of RC stars in star clusters as a function of $\log(t)$ (top) and $[\text{Fe}/\text{H}]$ (bottom). Open circles indicate the open clusters and filled triangles represent the globular clusters. These figures are taken from [van Helshoecht & Groenewegen \(2007\)](#), reproduced with permission from Astronomy & Astrophysics, © ESO.

1.3. ABSOLUTE MAGNITUDES OF RC STARS

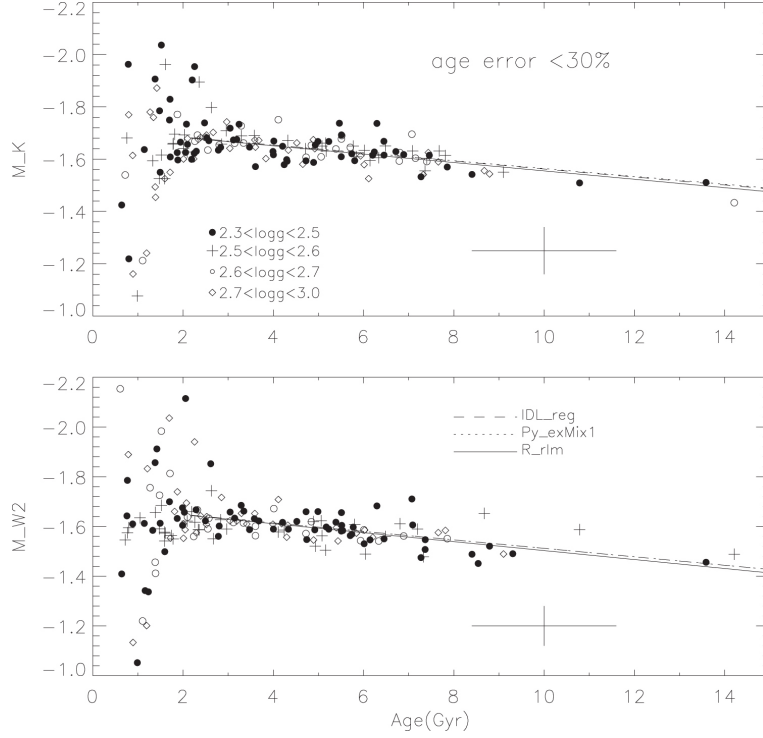


Figure 1.33: The age dependence of K and $W2$ absolute magnitudes. Different symbols indicate different $\log(g)$. Interstellar extinction is corrected. Lines display the best-fit relations derived by slightly different methods. Stars with age errors smaller than 30 per cent are plotted. These figures are taken from [Chen et al. \(2017\)](#), reproduced by permission of the AAS.

(2007) also investigated the RC stars in the Milky Way star clusters and concluded that negligible metallicity dependence of K -band absolute magnitude with $10^{8.5} < \text{Age} < 10^{9.9}$. However, young RC stars have a large scatter and the similar trend to the model prediction can be seen (Figure 1.32). [Chen et al. \(2017\)](#) used age and distance derived from asteroseismology, and derived very weak age dependence of K_S and $WISE W2$ absolute magnitudes for RC stars older than 2 Gyr

$$M_{K_S} = (0.015 \pm 0.003)\tau - (1.715 \pm 0.016), \quad (1.20)$$

$$M_{W2} = (0.017 \pm 0.003)\tau - (1.682 \pm 0.016), \quad (1.21)$$

where τ is the age in Gyr, but younger RC stars shows a large scatter of magnitudes (Figure 1.33). Unfortunately, detailed age dependence of absolute magnitudes for young RC stars could not be studied because of relatively large age errors.

Therefore, the observational research on the age dependence of RC stars is not enough. For the studies using the Milky Way star clusters, the small number of samples is the main limitation, and for the study using asteroseismology, the relatively large uncertainty in age is the limitation. Thus, the number of samples with both age and metallicity information is quite limited, and the

parameter space has not been covered enough up until now. So far, the correction of the population effect can be applied by theoretical models.

1.4 Star Clusters in the Large Magellanic Cloud

We use star clusters in the LMC to fill the parameter space, which previous research has not observationally studied. Star clusters in the LMC have different age and metallicity from Milky Way star clusters. Star clusters in the LMC are more metal-poor than star clusters containing RC stars in the Milky Way. Therefore, we can expand the parameter space to the more metal-poor and younger range. Moreover, the LMC has the almost face-on position in the sky, and is distant enough to be considered as the stars in the galaxy are at the same distance, so the uncertainty of the distance does not much affect the determination of absolute magnitudes of RC stars. In addition to these advantages, there are many young star clusters in the LMC, so we can investigate the age dependence of young RC stars where large age dependence is predicted from theoretical models.

Unfortunately, only one cluster with age between approximately 3 and 12 Gyr has been found (Geisler et al. 1997, the boundary values are different depending on literature). The reason why this cluster age-gap exists has not yet been understood, and the nature and cause of the age-gap attract great interest. On the other hand, it has been confirmed from observations with Hubble Space Telescope that the corresponding age-gap does not exist in the field stars (Holtzman et al. 1999; Smecker-Hane et al. 2002).

RC stars in the LMC star clusters have not been studied because they are too faint to determine their mean magnitude reliably in past NIR surveys such as 2MASS. Hence, we conducted NIR observations of the clusters using the IRSF. The long exposure time of our observations makes it possible to determine the mean RC magnitude in the LMC clusters. We also use the photometric data from the VMC survey. VMC photometric data are very deep and RC stars in the LMC are easily detected.

1.5 RC stars and stellar evolution

For low-mass CHeB stars, the theory of stellar structure and evolution is sophisticated. However, the basic theory has mainly three uncertainties.

1. The precise parameters of stars (e.g., core and envelope mass, chemical profile) with different masses and metallicities when they become CHeB stars
2. Convective processes at the core border
3. Nuclear reaction rate $^{12}\text{C}(\alpha, \gamma)^{16}\text{O}$

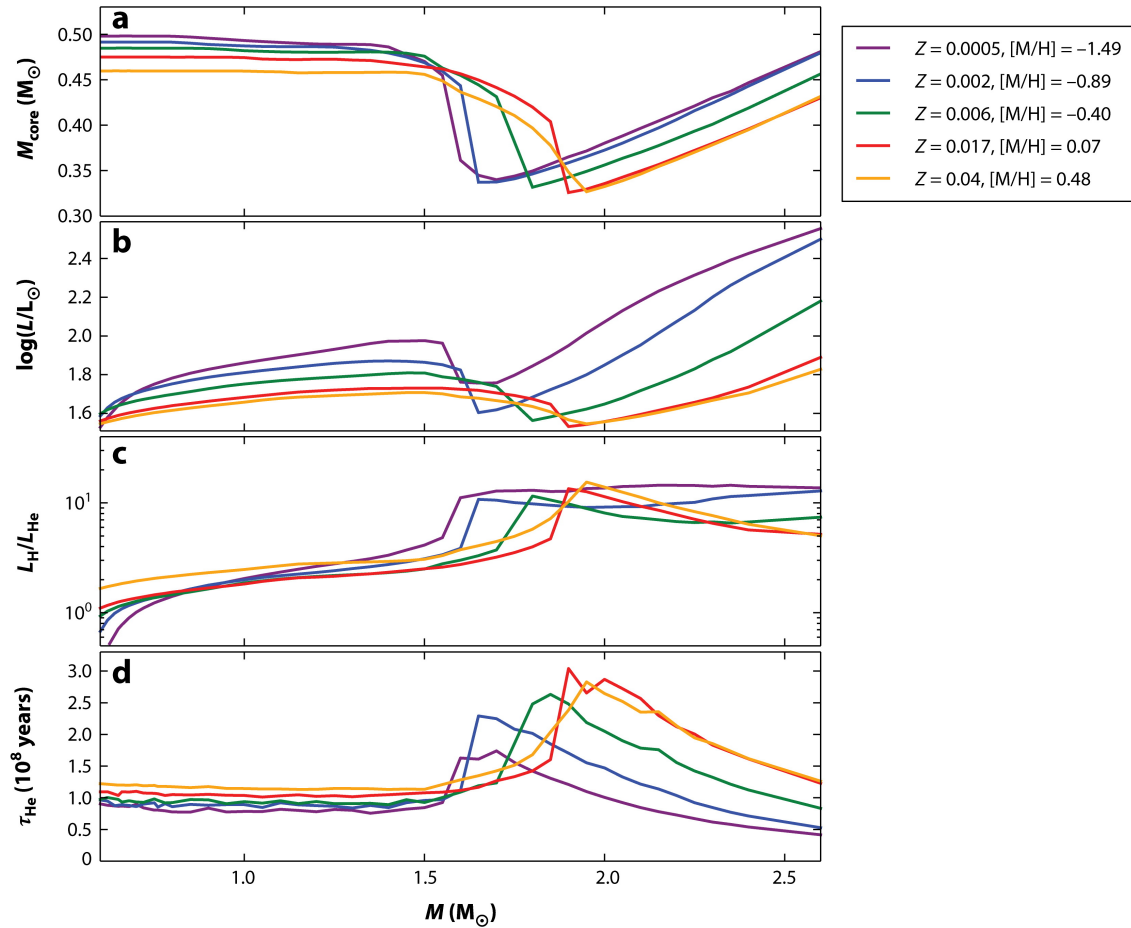
The luminosity of RC stars is mainly determined by core and envelope masses. For low-mass stars, the core mass at He ignition, M_{core}^0 is nearly constant regardless of the initial mass of stars (Figure 1.34). These low mass stars have electron-degenerate cores at the RGB phase, and the cores are supported by degeneration pressure. When the core mass reaches $0.5 M_{\odot}$ (the mass slightly changes with the chemical composition), core He ignition occurs. This ignition is explosive and so-called He flash. For more massive stars, the temperatures of He cores are high enough to occur He ignition before He cores become strongly degenerated. These stars quietly turn into CHeB phase, and M_{core}^0 is nearly proportional to the initial mass of stars (Figure 1.34).

This general picture has been confirmed by many independent theoretical calculations (e.g., Sweigart et al. 1990; Castellani et al. 2000; Girardi et al. 2013). However, the behavior of the parameters of stars with masses around the critical mass of He flash is not settled. The first problem is the critical mass of He flash has not yet understood. This critical mass is related to the minimum mass of M_{core}^0 . This mass is the boundary between low- and intermediate-mass stars. One of the factors that lead to mass uncertainty is the uncertainty of convective processes. The weaker convective mixing becomes, the higher critical masses become. The minimum mass of M_{core}^0 is associated with the faintest luminosity of RC stars. Therefore, if the faintest absolute magnitude of RC stars around 1 Gyr is determined from the observation, the critical mass of He flash can be obtained, and then the convective processes could be confined.

The second problem is how sharp M_{core}^0 drops between electron degenerated and not degenerated cores. The theoretical model by Sweigart et al. (1990) indicated that this transition occurs within the mass range smaller than $\sim 0.1 M_{\odot}$. More recent calculation with the high mass resolution by Girardi et al. (2013) suggested that this transition would occur in less than $0.01 M_{\odot}$. These behaviors are related to the population effect around 1-2 Gyr, and thus we can limit these behaviors from observations.

This uncertainty causes some differences in model predictions. One example is the differences between Salaris & Girardi (2002, Figure 1.29) and Girardi (2016, Figure 1.35). Comparing these two models, the general behavior is similar but the behavior between 2-4 Gyr is different. In Salaris & Girardi (2002), the more metal-rich RC stars are, the brighter K -band absolute magnitude becomes. However, the more metal-rich RC stars are, the fainter K -band absolute magnitude becomes in Girardi (2016) prediction.

In addition to the above problems, mass loss rate before CHeB phase is another uncertainty source. For relatively high mass stars, this uncertainty does not much affect the absolute magnitudes because the lifetime of stars is not long and the decrease of their masses are little. However, low mass stars lose substantial masses because their lifetime is long. Therefore, we can obtain the information about the mass loss rate before CHeB phase by investigating the absolute magnitudes of old RC stars.




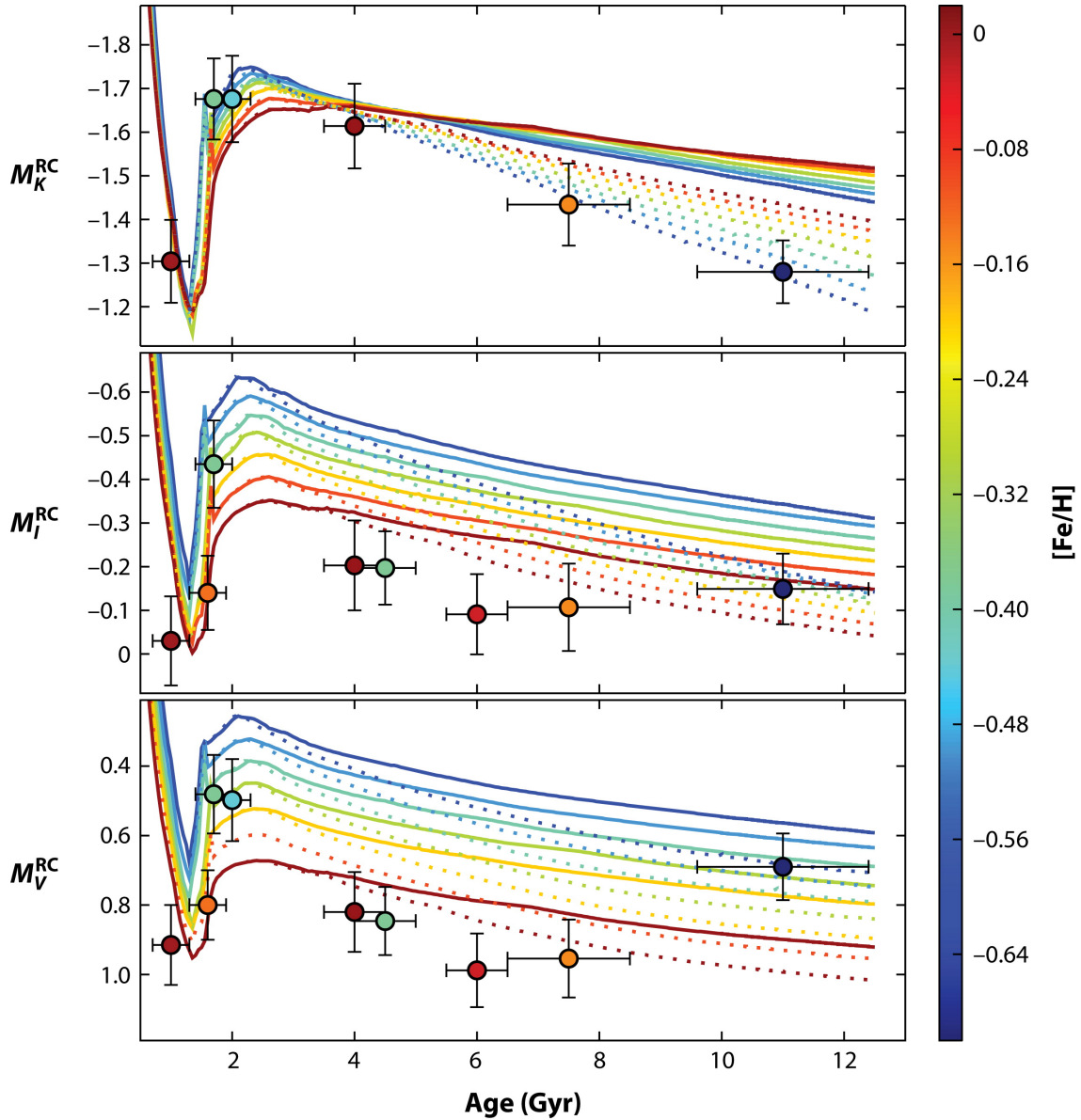
 Girardi L. 2016.
Annu. Rev. Astron. Astrophys. 54:95–133

Figure 1.34: Four parameters of the early time of CHEB stars as a function of mass and metallicity. Each panel shows (a) the He core mass, (b) the total stellar luminosity, (c) the luminosity ratio of H-burning shell to He-burning core, and (d) the lifetime of CHEB stars. This figure is taken from [Girardi \(2016\)](#), reproduced with the permission of Annual Reviews.




 Girardi L. 2016.
 Annu. Rev. Astron. Astrophys. 54:95–133

Figure 1.35: RC absolute magnitudes of the theoretical model for metallicities between 0 and -0.5 dex calculated by [Girardi \(2016\)](#), reproduced with the permission of Annual Reviews.

1.6 Structure of This Thesis

In chapter 2, we show the data and methods to determine NIR magnitudes of RC stars with the IRSF and VMC data. The results and comparison with previous work are presented in section 3. Chapter 4 is our conclusions. Part of this thesis with the IRSF data is the modified version of the paper entitled "The Age and Metallicity Dependence of the Near-Infrared Magnitudes of Red Clump Stars" by Onozato et al. that has been submitted to the Monthly Notice of the Royal Astronomical Society (MNRAS). Another part of this thesis with the VMC data is the modified version of the paper entitled "The Age and Metallicity Dependence of the Near-Infrared Magnitudes of Red Clump Stars II" by Onozato et al. that will be submitted to the MNRAS.

Chapter 2

The Data

2.1 IRSF data

2.1.1 Sample selection

When we investigate the metallicity and age dependence of absolute magnitudes of RC stars in clusters, it is important that metallicities and ages of the clusters have been determined using the same techniques. We can avoid systematic errors by using uniform samples. As a catalog that satisfies this condition, we used the LMC star cluster catalog compiled by [Palma et al. \(2016\)](#). The Palma's catalog lists 277 clusters.

From the catalog, we first selected clusters that had both age and metallicity information. Then, we chose clusters whose radii are larger than $0'.65$ (9.5 pc at 50 kpc) as our target clusters because we cannot detect the number excess of RC stars for small clusters. We excluded clusters that are in the bar region from the target (Figure 2.1), since these clusters are heavily contaminated by field stars. The number of clusters at each selection process is shown in Table 2.1. Finally, 15 clusters were selected to be observed by ourselves. Among the 15 clusters, we have detected a clear RC peak in its luminosity function for 10 clusters (see below for more detail). Figure 2.2 shows age and metallicity distribution of our target clusters, compared to clusters observed by [van Helshoecht & Groenewegen \(2007\)](#). This figure also contains VMC samples (see section 2.2). Most of our target clusters in the LMC ranges from 1 to 3 Gyr in age and from -1.0 to -0.4 dex in $[\text{Fe}/\text{H}]$, where [van Helshoecht & Groenewegen \(2007\)](#) have few samples. In this age range, a strong age dependence of the RC absolute magnitudes is predicted. Our target clusters have lower metallicity than the clusters used in [van Helshoecht & Groenewegen \(2007\)](#). In the very low metallicity region, theoretical models predict relatively strong metallicity dependence of absolute magnitudes. Our sample clusters allow us to investigate the dependence of the RC magnitudes at lower metallicity range than in our Galaxy.

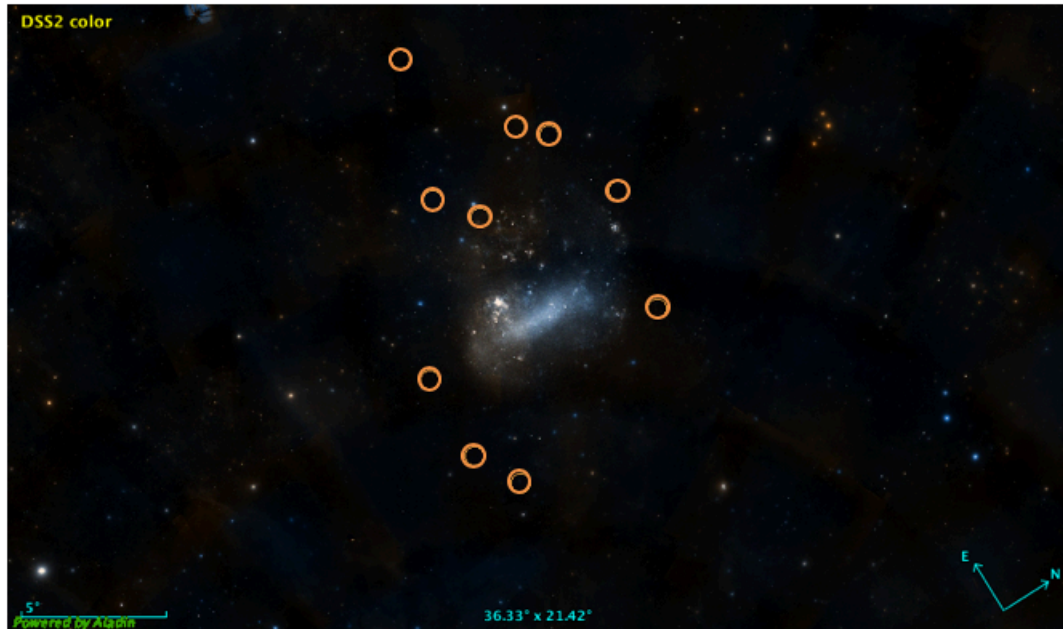


Figure 2.1: The distribution of the IRSF sample clusters.

Table 2.1: The number of star clusters at each selection process

Selection process	number of clusters
clusters in Palma et al. (2016)	277
clusters with age and metallicity	176
clusters larger than $0'.65$	26
clusters in outer region (observed)	15
clusters that have significant RC excess and can be fitted by equation (1.1)	10

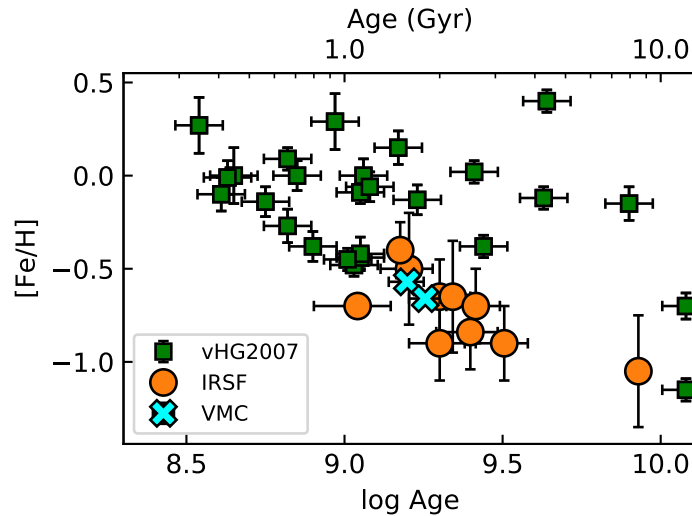


Figure 2.2: Age and metallicity distribution of IRSF target clusters (orange circles), VMC sample clusters (cyan crosses), and clusters observed by [van Helshoecht & Groenewegen \(2007\)](#), green squares).

2.1.2 Age and metallicity of Palma’s catalog

As described above, we used [Palma et al. \(2016\)](#) as the list of the LMC star clusters. This catalog contains 277 star clusters in the LMC. Within the 277 star clusters, 235 star clusters were collected by 16 previous studies, and 42 star clusters were newly observed in their work. All of these star clusters were observed using the Washington photometric system, and the parameters of the star clusters were obtained by the same procedures. Therefore, we can gain a uniform and homogeneous star cluster sample. Unfortunately, the number of star clusters in the catalog are limited compared to the total number of star clusters in the LMC. The LMC is very populous and the total number of star clusters that have been confirmed in the LMC is more than 3000 ([Bica et al. 2008](#)). However, the Palma’s catalog is the largest uniform LMC star clusters samples up until now.

The Washington photometric system was originally developed by [Canterna \(1976\)](#) to study G and K giants. This photometric system is composed of four filters, C (the effective wavelength is 3910 Å), M (5085 Å), T_1 (6330 Å), and T_2 (8050 Å, [Figure 2.3](#)). The accuracy of determining metallicity using this system was improved by [Geisler et al. \(1991\)](#). This system has been widely used to investigate star clusters with various age (from young to old) in the Milky Way (e.g., [Clariá et al. 2007](#); [Piatti et al. 2009](#)) and in the Magellanic Clouds ([Geisler et al. 2003](#)). The advantage of this system is that the C and T_1 filters are approximately three times more sensitive to metallicity than the Johnson V and I filters.

The ages and metallicities of the star clusters were determined by two independent procedures.

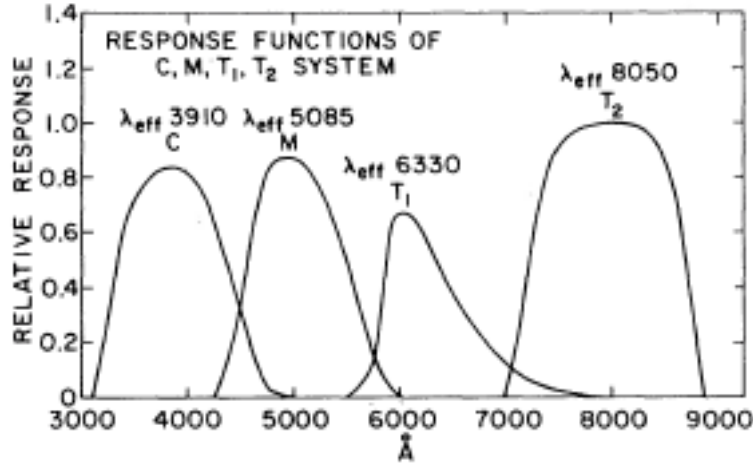


Figure 2.3: The relative response curve of the four filters of the Washington system. This figure is taken from [Canterna \(1976\)](#), reproduced by permission of the AAS.

In both procedures, $(C - T_1, T_1)$ CMD is used to determine the ages and metallicities. First, field star contamination was cleaned by a statistical method developed by [Piatti & Bica \(2012\)](#). The expected number density of field stars was computed and subtracted randomly. For the cleaned CMDs of the clusters, isochrone fitting was done in the first method. Interstellar extinction was estimated by interpolating the extinction maps created by [Burstein & Heiles \(1982\)](#) using HI (21-cm) emission data. The values of $E(B - V)$ are small (< 0.23), so the uncertainty of these values would not be a large error source. As the distance modulus to the LMC, $(m - M)_0 = 18.50 \pm 0.10$ ([Saha et al. 2010](#)) was applied. [Subramanian & Subramaniam \(2009\)](#) reported that the average depth of the LMC disk is 3.44 ± 0.16 kpc. This leads to ~ 0.13 mag difference at the distance modulus of 18.50 mag. This value is smaller than the average uncertainty of isochrone fitting (~ 0.3 mag). Therefore, the uncertainty of the distance also would not be a large error source. Conversely, we cannot determine the distance to the individual LMC star clusters by isochrone fittings. Two types of theoretical isochrones were used for validation. One is developed by the Padova group ([Girardi et al. 2002](#); [Bressan et al. 2012](#)), and the other is developed by Geneva group ([Lejeune & Schaerer 2001](#)). According to [Palma et al. \(2016\)](#), nearly similar results were obtained from [Girardi et al. \(2002\)](#) and [Lejeune & Schaerer \(2001\)](#), but slightly different results were obtained from the newer isochrone ([Bressan et al. 2012](#), Figure 2.4). From Figure 2.4, the estimated ages are 20-30 per cent different in [Girardi et al. \(2002\)](#) isochrones and [Bressan et al. \(2012\)](#) isochrones. For the newer data in the catalog, [Bressan et al. \(2012\)](#) isochrones were used for fittings because metallicity intervals are smaller than [Girardi et al. \(2002\)](#) isochrones, and more precise parameters could be obtained. However, some older data collected from previous papers used [Girardi et al. \(2002\)](#) isochrones. For these clusters, metallicity values have lower accuracy than those calculated by [Bressan et al. \(2012\)](#). In our sample clusters, the ages and metallicities of NGC 1997 and NGC 2161 were

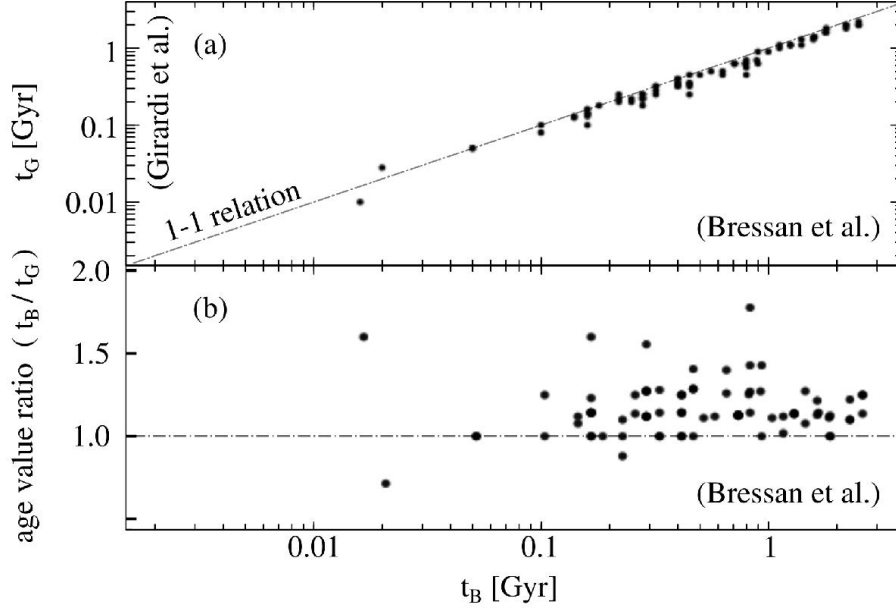


Figure 2.4: The comparison of the cluster ages estimated by two isochrones, [Girardi et al. \(2002\)](#) and [Bressan et al. \(2012\)](#). This figure is taken from [Palma et al. \(2016\)](#), reproduced with permission from Astronomy & Astrophysics, © ESO.

derived using [Girardi et al. \(2002\)](#) isochrones.

In the second method, the difference in T_1 magnitude (δT_1) between RC stars and main sequence turn off in the $(C - T_1, T_1)$ CMD was used. The age was estimated using the equation obtained by [Geisler et al. \(1997\)](#)

$$\text{Age(Gyr)} = 0.23 + 2.31 \times \delta T_1 - 1.80 \times \delta T_1^2 + 0.645 \times \delta T_1^3. \quad (2.1)$$

The estimated typical errors are ± 0.3 Gyr, and the majority of the estimated ages are consistent with the ages obtained by isochrone fittings within the uncertainty. This method can be used for star clusters with a sufficient number of RC stars because the magnitude of RC stars are critical to derive δT_1 . Therefore, the ages of young clusters ($\lesssim 1$ Gyr) were not obtained from this method. Metallicities were obtained by the absolute magnitudes M_{T_1} and the dereddened colors $(C - T_1)_0$ of RGB stars. This method is so-called standard giant method ([Geisler & Sarajedini 1999](#)). The dereddened colors were derived from

$$E(C - T_1) = 1.97E(B - V), \quad (2.2)$$

and the absolute magnitudes were calculated by

$$M_{T_1} = T_1 + 0.58E(B - V) - 18.50. \quad (2.3)$$

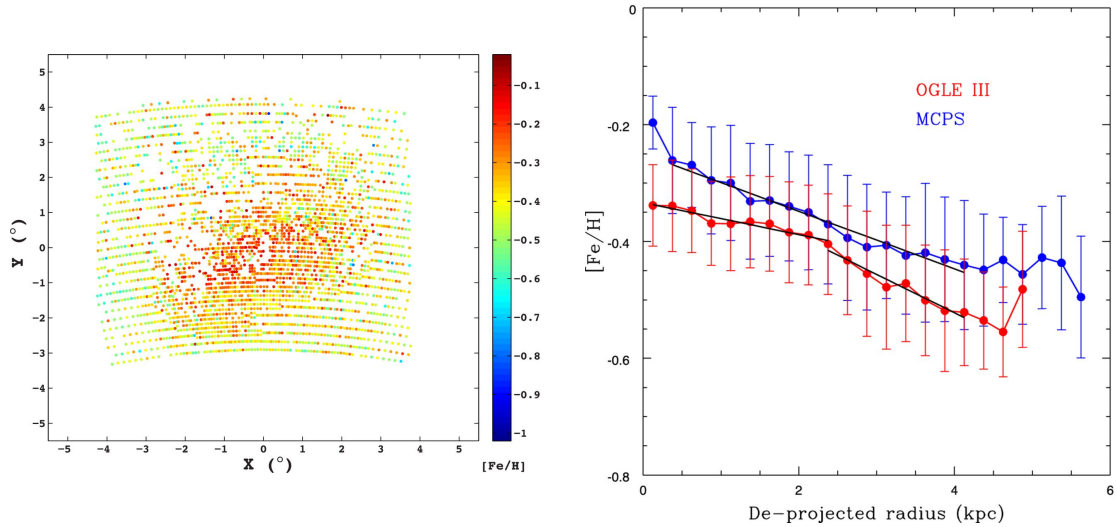


Figure 2.5: (left) A metallicity map created from photometric metallicity using the Magellanic Cloud Photometric Survey (MCPS). (right) Metallicity distribution as a function of the de-projected radius. Red points represent OGLE III data, and blue points indicate MCPS. This figure is taken from Choudhury et al. (2016), reproduced with the permission of Oxford University Press.

The typical errors of metallicities derived from this method are 0.3 dex, and most of the derived metallicities are consistent with the metallicities calculated by isochrone fittings within the uncertainty. These techniques are applicable only for older clusters ($\gtrsim 2$ Gyr, Geisler & Sarajedini 1999), so the metallicities of younger clusters were not derived from this method.

To verify the accuracy of these methods, we investigated the metallicity gradient of the LMC star clusters. As is the case with the Milky Way and other spiral galaxies, it is known that the metallicity gradient exists in the LMC (Choudhury et al. 2016, Figure 2.5). From their results, the average metallicity varies from -0.2 (center) to -0.5 dex (outside). Star clusters in Palma et al. (2016) show the similar trend that clusters at inner regions are metal-rich and clusters at outer regions are metal-poor as can be seen in Figure 2.6, although the scatter is relatively larger. However, there are many clusters with $[\text{Fe}/\text{H}] = -0.4$ dex. The majority of the metallicities of these clusters were estimated using Girardi et al. (2002) isochrones. The metallicities of some clusters with $[\text{Fe}/\text{H}] = -0.7$ dex were also derived from Girardi et al. (2002) isochrones, although the number of clusters is small. These clusters deviate from the metallicity gradient trend. Considering the metallicity intervals of 0.3 or 0.4 dex, the accuracy of metallicity determination is 0.3 dex or worse for these clusters.

We used the ages and metallicities of star clusters derived by the isochrone fitting method. However, Palma et al. (2016) did not derive the ages and metallicities of the three clusters (KMHK 21, ESO 85-72, and ESO 121-3) in our samples from the isochrone fittings. Therefore, we applied the ages and metallicities derived from the second method for these three clusters. From the catalog

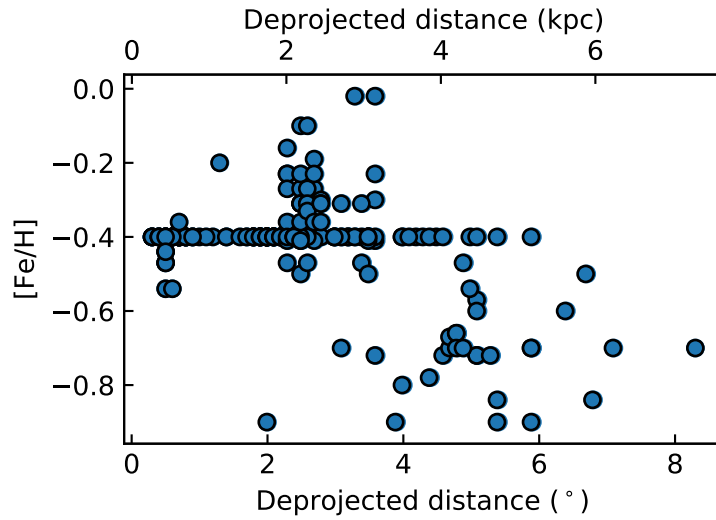


Figure 2.6: The metallicity distribution of star clusters in [Palma et al. \(2016\)](#) as a function of de-projected distance from the LMC center.

data, we can consider that the accuracy of the ages are 20-30 per cent and the metallicities are 0.3 dex.

2.1.3 Observation

Observations were performed using the SIRIUS camera equipped on the IRSF 1.4-m telescope ([Nagashima et al. 1999](#); [Nagayama et al. 2003](#)) in the South African Astronomical Observatory in 2017 November and December. SIRIUS can collect JHK_S -band images simultaneously with a 7.7×7.7 field of view with a pixel scale of $0''.45 \text{ pixel}^{-1}$. The seeing size was typically 1.5 arcsec and sometimes reached to 0.9 arcsec. The exposure time of each image was 20 s and 25 images were taken in each dithering set. The number of the observation sets were from 35 to 41. Observed clusters and their observational information are listed in [Table 2.2](#).

2.1.4 Data reduction

We reduced the obtained images by the standard data reduction process. We used pyIRSF pipeline software¹ for this reduction. The outline of the reduction process is as follows. First, a dark frame was subtracted from each raw image to remove the effect of the dark current. Ten dark frames were combined with average values to make a dark frame. Then we did flat-field division to correct nonuniform sensitivity of each pixel. Twilight-flat exposures were used to produce the flat-field

¹<https://sourceforge.net/projects/irsfsoftware/>

Table 2.2: List of observed star clusters

Cluster name	RA (J2000)	Dec (J2000)	Observation Date	Number of combined images	total exposure time (sec)
KMHK 21	04 ^h 37 ^m 52 ^s	-69°01'42''	2017 Nov 16	925	18500
KMHK 337	04 ^h 57 ^m 34 ^s	-65°16'00''	2017 Nov 22	1025	20500
ESO 85-72	05 ^h 20 ^m 05 ^s	-63°28'49''	2017 Nov 11	900	19000
NGC 1997	05 ^h 30 ^m 34 ^s	-63°12'12''	2017 Nov 10	800	16000
IC 2140	05 ^h 33 ^m 21 ^s	-75°22'35''	2017 Dec 3	925	18500
KMHK 1281	05 ^h 43 ^m 20 ^s	-66°15'44''	2017 Dec 12	975	19500
NGC 2161	05 ^h 55 ^m 42 ^s	-74°21'14''	2017 Nov 27	1000	20000
NGC 2155	05 ^h 58 ^m 33 ^s	-65°28'37''	2017 Nov 30	1000	20000
ESO 121-3	06 ^h 02 ^m 02 ^s	-60°31'24''	2017 Nov 9	875	17500
NGC 2213	06 ^h 10 ^m 42 ^s	-71°31'44''	2017 Dec 11	975	19500

image. Several dozen pairs of images with dimming or brightening twilight sky were collected from twilight-flat images, and the difference between two images of the pairs was combined to make a flat-field image after each image was normalized. After flat-field divisions were performed, then sky frames were subtracted to remove the background pattern of the images. Object frames themselves were used to make sky frames. These dithered images were combined with median values and no shift. To avoid the effect of cluster stars, we chose large (60'') dithering radii in the observations. Finally, these sky-subtracted images were combined with average values. The dithering offsets were shifted using bright stars in the sky-subtracted images.

Point spread function fitting photometry was performed for combined images with IRAF/DAOPHOT package. We used the 2MASS PSC (Skrutskie et al. 2006) to convert instrumental magnitudes to calibrated apparent magnitudes. We calculated the weighted mean difference between instrumental magnitude and 2MASS magnitude in the field of view to decide zero point. Photometric errors against JHK_S magnitudes for stars in our target clusters are plotted in Figures 2.7 and 2.8. These errors were calculated by the allstar task in IRAF/DAOPHOT package. Typical error of J -band is 0.04 mag at 18.0 mag, H -band is 0.08 mag at 17.5 mag, and K_S band is 0.20 mag at 17.5 mag.

We used Palma's catalog value as cluster radii and chose stars in circular regions as cluster stars. These radii are taken from Bica et al. (2008). For stars within the circles, we plotted color-magnitude diagrams and decided to use stars with $17.5 \text{ mag} < K_S < 15.0 \text{ mag}$ and $0.2 < J - K_S < 0.8$ to fit the luminosity function of the RC stars (Figure 2.9). We fitted the magnitude distribution of the stars with equation 1.1. The uncertainty in m_λ^{RC} is standard error and calculated by

$$\text{standard error} = \frac{\sigma_\lambda}{\sqrt{N_{RC}}}, \quad (2.4)$$

where N_{RC} is the number of RC stars calculated by

$$N_{RC} = \sqrt{2\pi}\sigma_\lambda \times 10d. \quad (2.5)$$

Factor 10 corresponds to the width of histogram bin 0.1 mag. A typical standard error of the RC mean magnitudes for the clusters is 0.015 mag. Then, reddening was corrected using $E(B - V)$

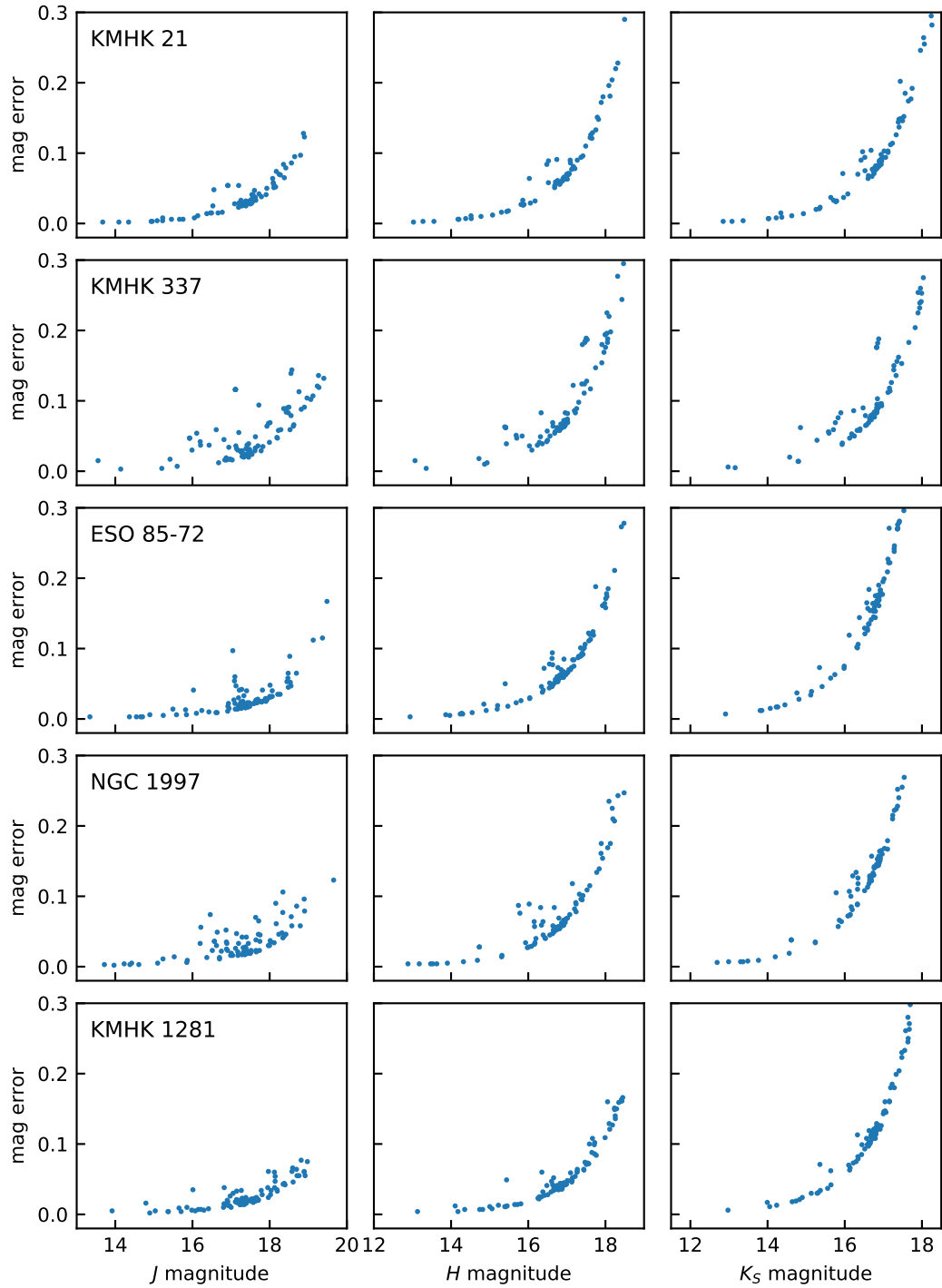


Figure 2.7: Photometric errors versus magnitudes for our target clusters.

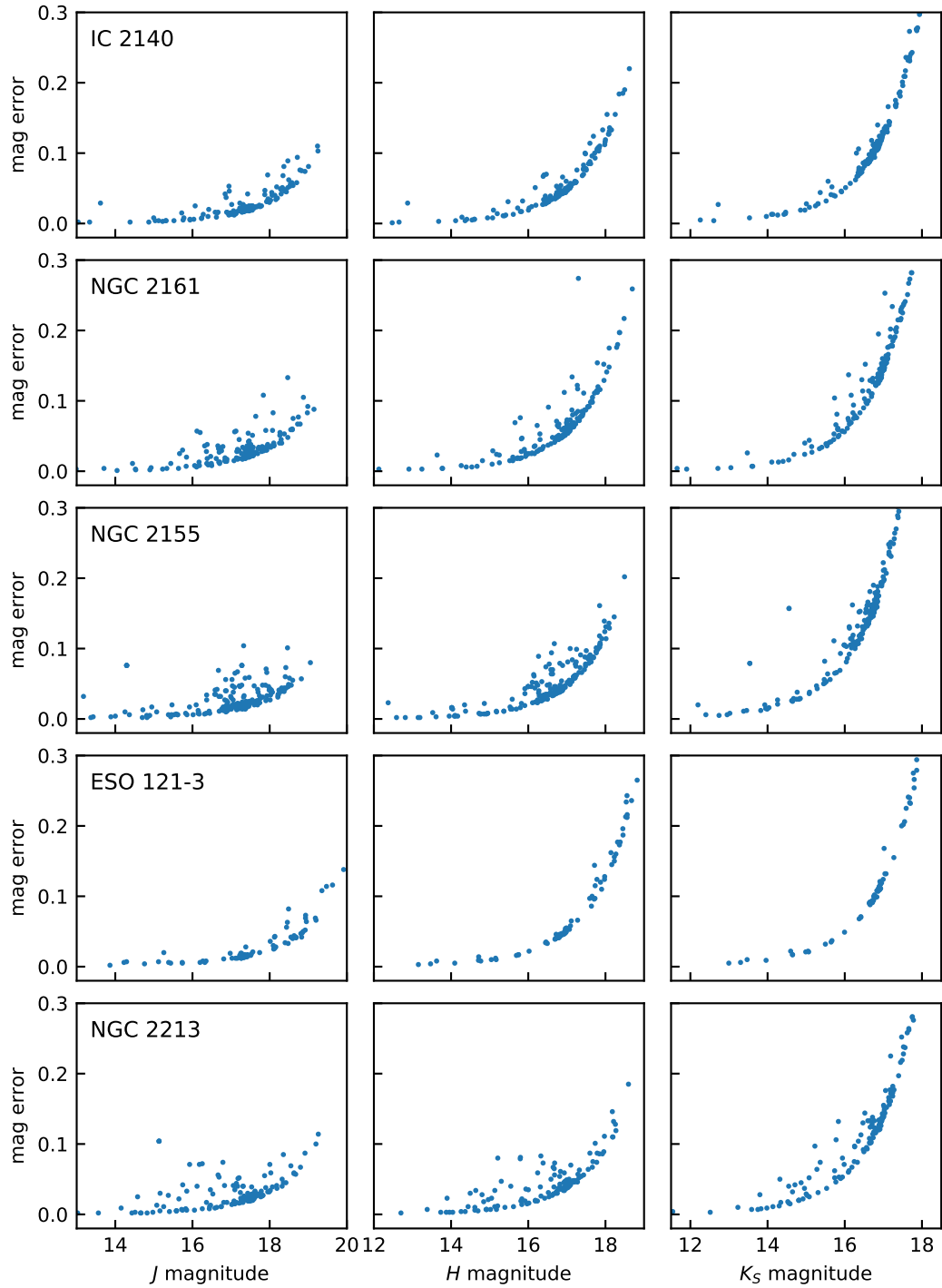


Figure 2.8: Continued from Figure 2.7.

Table 2.3: Cluster Information

Cluster name	Radius (arcmin)	$E(B - V)$	Age (Gyr)	[Fe/H]	m_J^a	m_H^a	$m_{K_s}^a$	$m_J - m_{K_s}^a$
KMHK 21	0.75	0.040	1.60 ± 0.30	-0.50 ± 0.30	17.485 ± 0.017	16.962 ± 0.029	16.860 ± 0.027	0.625 ± 0.032
KMHK 337	0.68	0.020	2.00 ± 0.20	-0.65 ± 0.20	17.381 ± 0.015	16.900 ± 0.017	16.833 ± 0.013	0.548 ± 0.020
ESO 85-72	0.85	0.030	2.20 ± 0.30	-0.65 ± 0.30	17.279 ± 0.025	16.806 ± 0.024	16.799 ± 0.017	0.480 ± 0.030
NGC 1997	0.90	0.040	2.60 ± 0.50	-0.70 ± 0.20	17.374 ± 0.014	16.889 ± 0.015	16.857 ± 0.015	0.517 ± 0.020
IC 2140	1.15	0.111	$2.50^{+0.60}_{-0.50}$	$-0.84^{+0.22}_{-0.18}$	17.337 ± 0.020	16.860 ± 0.019	16.794 ± 0.019	0.543 ± 0.027
KMHK 1281	0.80	0.050	2.00 ± 0.40	-0.90 ± 0.20	17.272 ± 0.011	16.802 ± 0.011	16.750 ± 0.014	0.522 ± 0.018
NGC 2161	1.15	0.130	1.10 ± 0.30	-0.70^b	17.374 ± 0.012	16.961 ± 0.013	16.896 ± 0.012	0.478 ± 0.017
NGC 2155	1.20	0.050	3.20 ± 0.60	-0.90 ± 0.20	17.254 ± 0.011	16.771 ± 0.010	16.728 ± 0.018	0.527 ± 0.021
ESO 121-3	1.05	0.030	8.50 ± 0.30	-1.05 ± 0.30	17.308 ± 0.018	16.900 ± 0.015	16.827 ± 0.024	0.480 ± 0.030
NGC 2213	1.05	0.116	1.50^b	-0.40 ± 0.15	17.427 ± 0.012	16.906 ± 0.016	16.915 ± 0.010	0.512 ± 0.016

^a Interstellar extinction was corrected by Cardelli et al. (1989) extinction law.

^b The uncertainties are not described in Palma et al. (2016)

values from Palma’s catalog and the Cardelli et al. (1989) extinction law. This extinction law takes the form

$$\frac{A_\lambda}{A_V} = a(\lambda) + \frac{b(\lambda)}{R_V}, \quad (2.6)$$

where $a(\lambda)$ and $b(\lambda)$ are

$$a(\lambda) = 0.574\lambda^{-1.61} \quad (2.7)$$

$$b(\lambda) = -0.527\lambda^{-1.61} \quad (2.8)$$

for infrared wavelengths ($0.9 \mu\text{m} < \lambda < 3.3 \mu\text{m}$), and we used $R_V = 3.1$. We only used clusters that had significant excess of red clump stars. As a consequence, 10 clusters were used to investigate the magnitude of RC stars. The parameters of the clusters used in this work are listed in Table 2.3.

2.2 VMC data

2.2.1 Sample Selection

As is the case with the IRSF samples, we used the LMC star cluster catalog by Palma et al. (2016) to avoid the systematic errors of ages and metallicities of the LMC star clusters. For photometric data, we used the VMC survey Data Release 4 (DR4). The VMC survey is a uniform and homogeneous survey of the LMC, the SMC, and the Magellanic Bridge with the NIR YJK_S filters. Observations were conducted using VISTA infrared camera (VIRCAM) on VISTA 4-m telescope in the La Silla Paranal Observatory. DR4 data were taken from 2009 November to 2013 August. VIRCAM has a field of view of 1.65 deg^2 with a mean pixel size of $0''.339$. The 10σ detection limit of Y -band is 21.9 mag, J -band is 21.4 mag, and K_S -band is 20.3 mag. These magnitudes are much deeper than that expected for RC stars in the LMC. DR4 data cover about 8 deg^2 in the LMC, and the survey field is shown in Figure 2.10. The center coordinate of each survey tile is presented in Table 2.4. The VMC survey provides both aperture photometry data and PSF fitting photometry data, and we used the latter one.

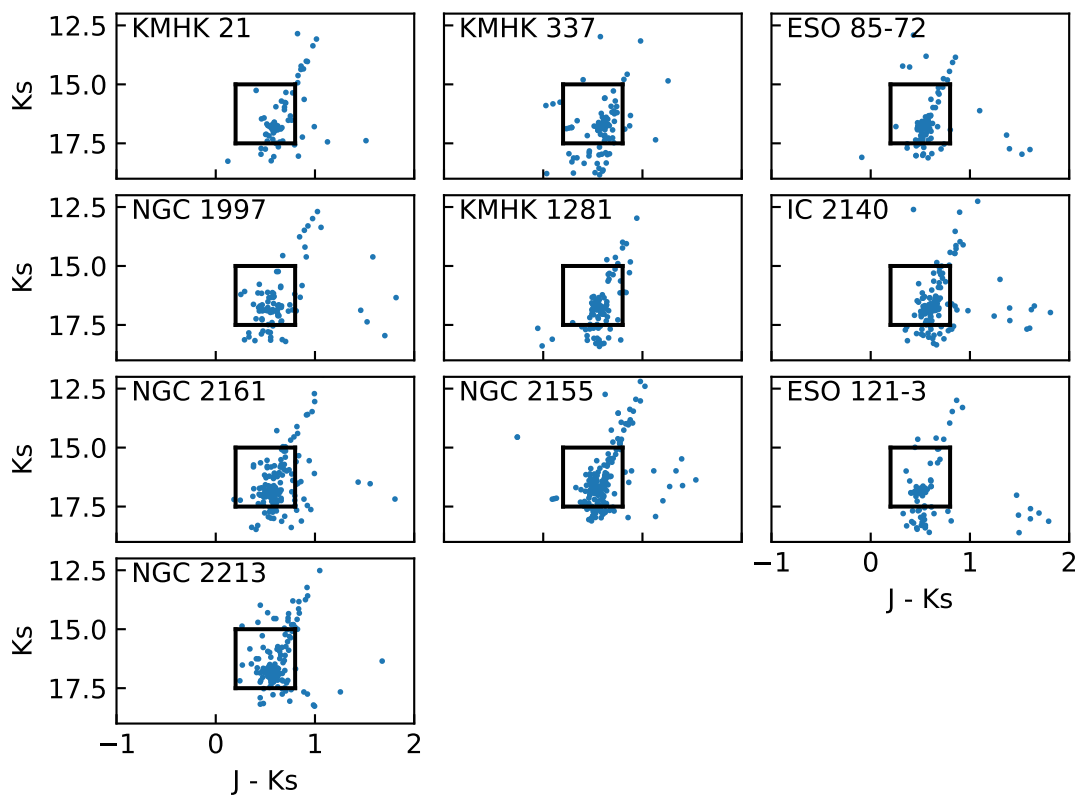


Figure 2.9: $J - K_S$ versus K_S CMDs of our target clusters. All stars within the box are used to determine the mean RC magnitude in the clusters.

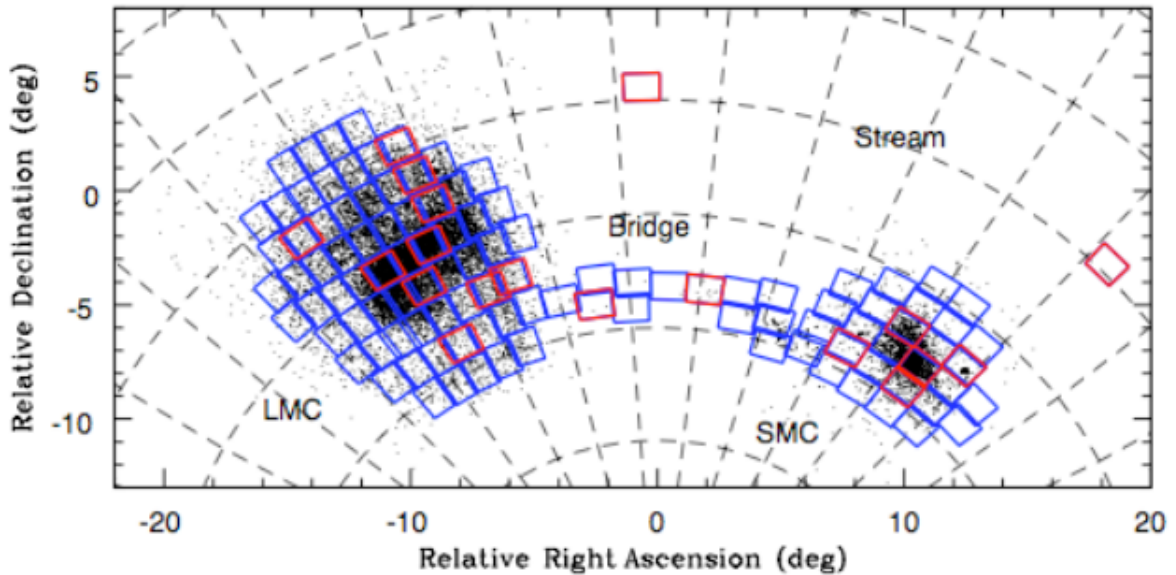


Figure 2.10: The survey field of the VMC survey. Red rectangles represent the fields released in the DR4, and blue rectangles represent the fields which will be observed by the final data release. This figure is taken from ESO Phase 3 Data Release Description².

First, we chose the Palma’s clusters that are in the observing field of VMC survey DR4. From these clusters, we searched the clusters whose peak number densities are two times higher than the number densities around the clusters when we divided the survey fields into $15'' \times 15''$ tiles because it is difficult to identify the clusters with low overdensity (Figures A.1 - A.5 in the Appendix A). Even if the identification is possible, these clusters are heavily suffered from field star contamination. This effect is especially strong in the bar region (LMC 5_5, LMC 6_4, and LMC 6_6), and we could not find the clusters exceeding the criterion, although these regions have many clusters (Figures A.2 and A.3 in the Appendix A). We selected 11 clusters by the criterion, but three clusters do not have metallicity information. Finally, 8 clusters were selected as our sample clusters, but in these clusters, we could not detect clear RC peaks in the luminosity functions of six clusters after the contamination of field stars was subtracted. Therefore, we selected only two clusters as our sample clusters (Table 2.5). The number of star clusters at each selection process is presented in Table 2.6. The age and metallicity distribution of selected sample clusters is shown in Figure 2.2.

²<http://eso.org/rm/api/v1/public/releaseDescriptions/93>

Table 2.4: The center coordinates of survey tiles

Tile	RA	Dec
LMC 3_5	05:22:43.056	-73:43:25.320
LMC 4_2	04:41:30.768	-71:49:16.320
LMC 4_3	04:55:19.510	-72:01:53.400
LMC 5_5	05:24:30.336	-70:48:34.200
LMC 6_4	05:12:55.800	-69:16:39.360
LMC 6_6	05:37:40.008	-69:22:18.120
LMC 7_3	05:02:55.200	-67:42:14.760
LMC 8_3	05:04:53.952	-66:15:29.880
LMC 8_8	05:59:23.136	-66:20:28.680
LMC 9_3	05:06:40.632	-64:48:40.320

Table 2.5: The equatorial coordinates and radii of our sample clusters

Cluster name	RA (J2000)	Dec (J2000)	Radius (arcmin)
KMHK 105	04 ^h 47 ^m 30 ^s	-72° 35' 18"	0.92
2MASX J05283953-7337514	05 ^h 28 ^m 39 ^s	-73° 37' 49"	1.08

Table 2.6: The number of star clusters at each selection process

Selection process	number of clusters
clusters in Palma et al. (2016)	277
clusters observed by VMC survey DR4	95
clusters with two times higher peak densities than those in field regions	11
clusters with age and metallicity	8
clusters that have significant RC excess and can be fitted by equation (1.1)	2

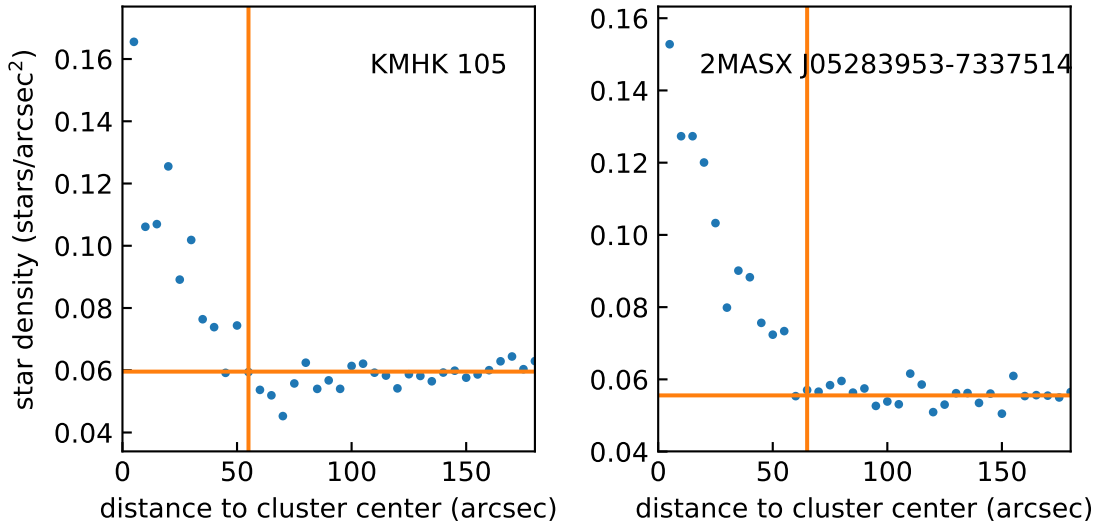


Figure 2.11: The density profiles of our sample clusters. Horizontal lines represent the median star densities of field regions (120-180 arcsec), and Vertical lines represent cluster radii. We defined the cluster radii where the star densities equal the median densities of field regions.

2.2.2 RC magnitudes determination

After sample clusters were selected, we decided the radii of sample clusters. We defined the cluster radii at which the star densities equal the densities of field regions (Figure 2.11). The densities of field regions were determined from the median densities between 120 and 180 arcsec from the cluster centers. Using the determined cluster radii, we plotted the CMDs of sample clusters (Figure 2.12). We used stars with $18.0 < K_S < 15.0$ and $0.2 < J - K_S < 0.8$ to fit the luminosity function of the RC stars. We used equation (1.1) as a fitting function as is the case in the IRSF data. Before we fit the function to the luminosity functions, field star contamination was subtracted. The luminosity functions of field regions were obtained from the regions between 120 and 300 arcsec from the cluster centers and then multiplied area ratios. This luminosity functions of field stars were subtracted from the luminosity functions of cluster regions and fitted to the equation (1.1). The uncertainty in m_λ^{RC} is also calculated in the same manner with the IRSF data. The [Cardelli et al. \(1989\)](#) extinction law was applied to correct the interstellar extinction.

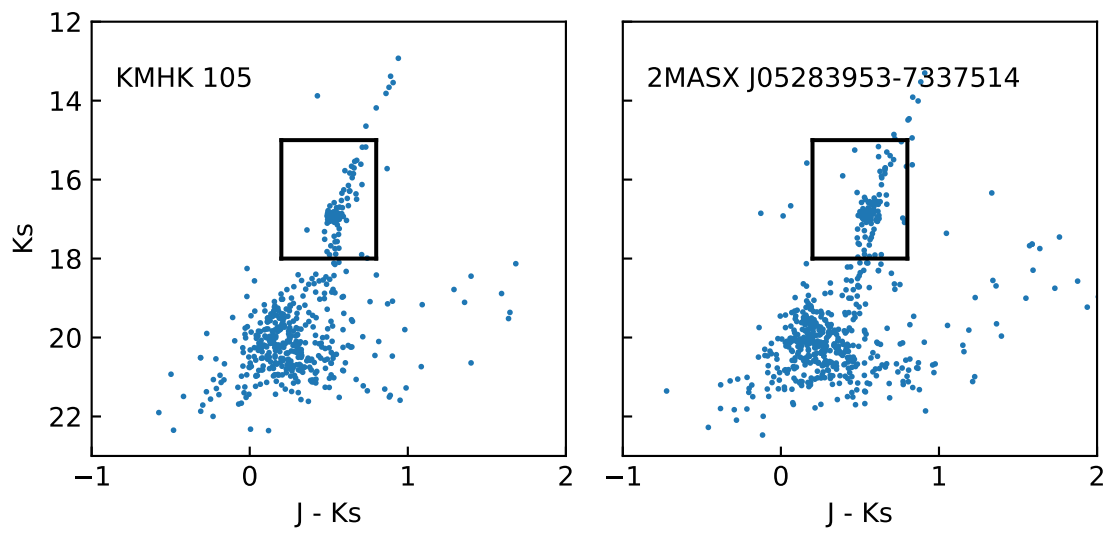


Figure 2.12: $J - K_S$ versus K_S CMDs of our target clusters. All stars within the box are used to determine the mean RC magnitude in the clusters.

Chapter 3

Results and discussion

The JHK_S magnitude distribution of the RC stars and fitting results for the IRSF data are shown in Figures 3.1 and 3.2, and YJK_S magnitude histograms for VMC data are provided in Figure 3.3 and 3.4. RC magnitudes derived from the fittings using equation (1.1) are listed in Tables 2.3 and 3.1. To verify the robustness of obtained magnitudes, we changed the bin size to narrower value 0.05 and wider value 0.20 (Tables 3.2 and 3.3). For the bin size of 0.05, we obtained consistent results within the standard errors. For the bin size of 0.20, some star clusters show the relatively large difference compared to the standard errors. However, this difference does not affect our discussion.

The m_λ values for the star clusters in our sample versus age are plotted in Figure 3.5, and the m_λ versus metallicity are plotted in Figure 3.6. Figures 3.7 and 3.8 present comparison of our K_S -band results with data from van Helshoecht & Groenewegen (2007) and the model of Salaris & Girardi (2002). In these two figures, apparent magnitudes of our results are converted to absolute magnitudes using the distance modulus to the LMC (18.493 mag, Pietrzyński et al. 2013). We assume that all clusters in the LMC are at the same distance because we cannot obtain the distance information on each cluster from Palma’s catalog.

3.1 Age dependence

Apparent magnitudes m_Y , m_J , m_H , m_{K_S} show the same trends that older RC stars are brighter within 1–3 Gyr, and much older RCs are slightly fainter (Figure 3.5). These are the same trends

Table 3.1: Cluster Information

Cluster name	$E(B - V)$	Age (Gyr)	[Fe/H]	m_Y^a	m_J^a	$m_{K_S}^a$	$m_J - m_{K_S}^a$
KMHK 105	0.116	1.58 ± 0.20	-0.57^b	17.740 ± 0.018	17.374 ± 0.018	16.894 ± 0.022	0.480 ± 0.028
2MASX J05283953-7337514	0.106	1.80 ± 0.20	-0.66^b	17.677 ± 0.026	17.389 ± 0.021	16.914 ± 0.018	0.475 ± 0.027

^a Interstellar extinction was corrected by Cardelli et al. (1989) extinction law.

^b The uncertainty is not described in Palma et al. (2016)

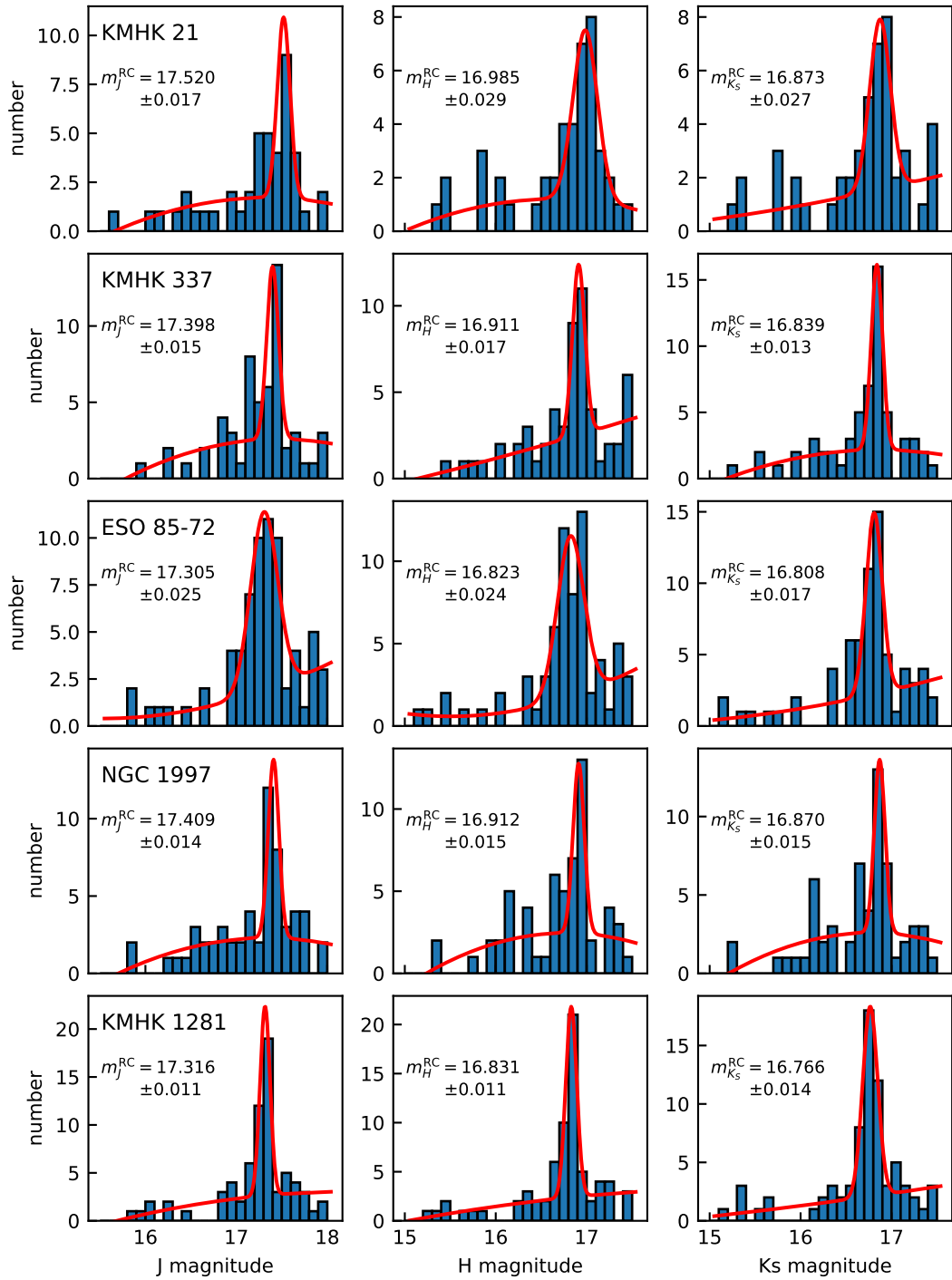


Figure 3.1: The distribution of the RC stars as a function of their magnitudes in the J - (left), H - (center), and K_S -bands (right). The fitting results with the equation (1.1) are shown by red lines.

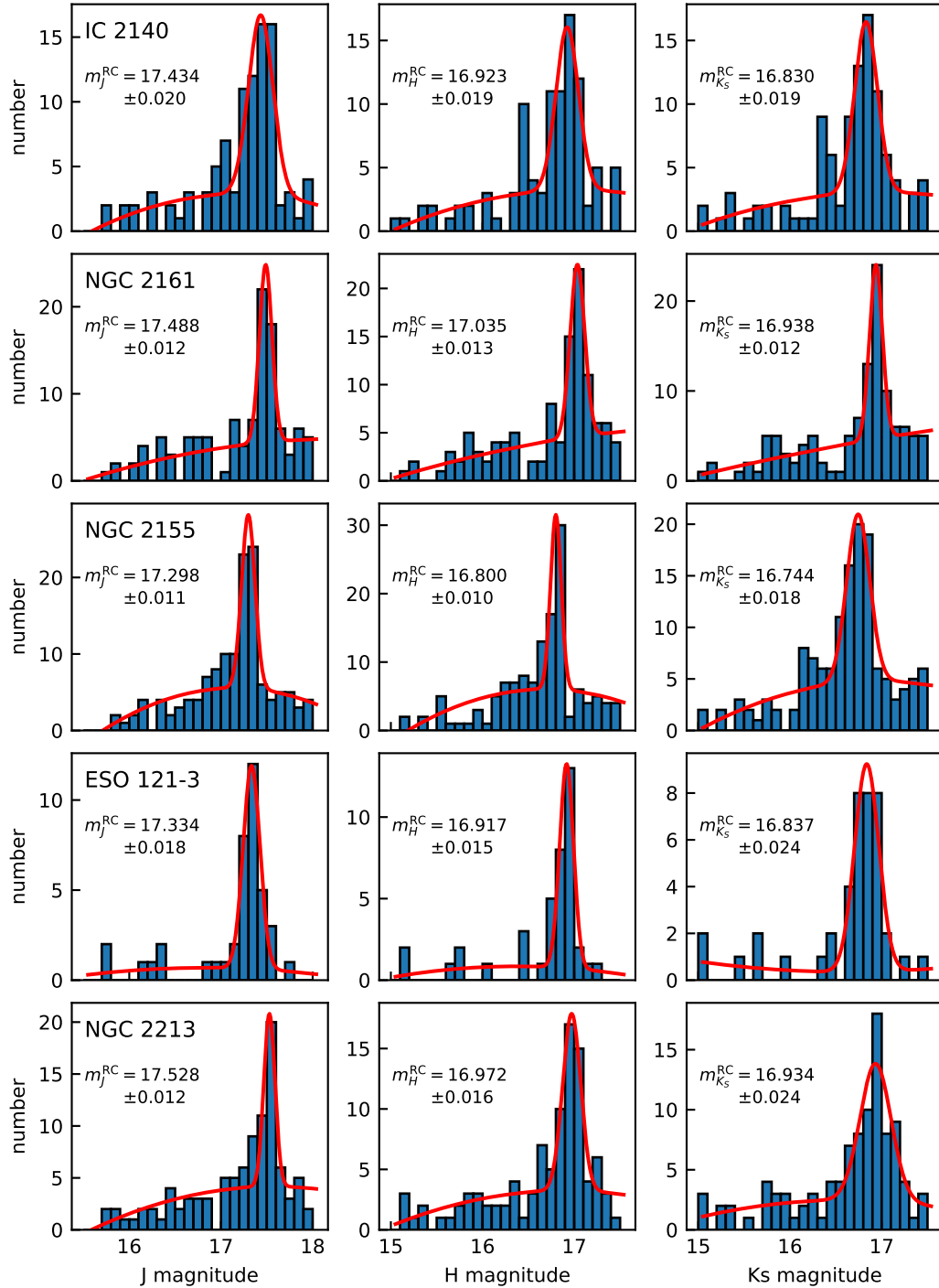


Figure 3.2: Continued from Figure 3.1.

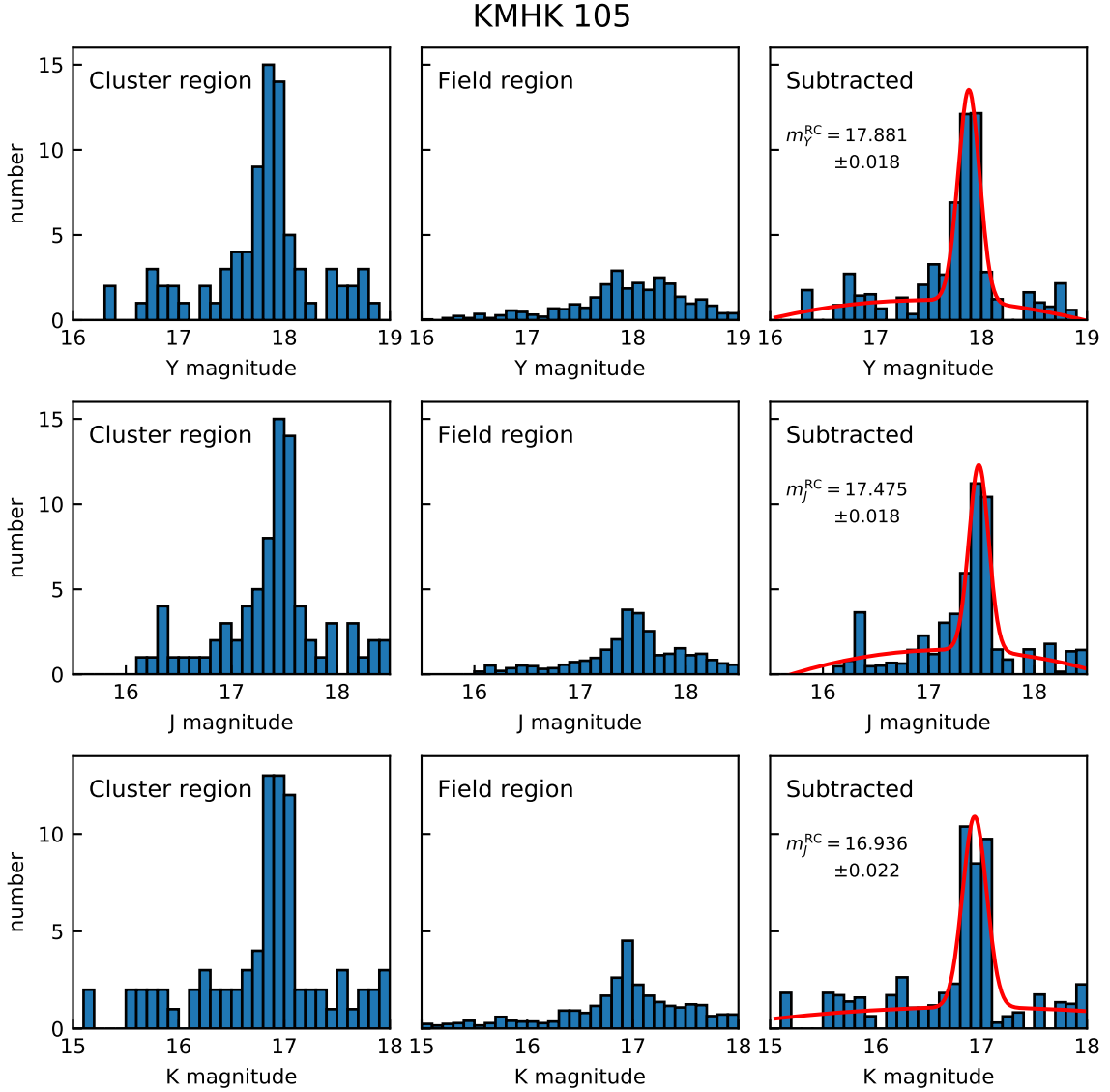


Figure 3.3: The luminosity functions of the RC stars as a function of their magnitudes in the Y- (top), J- (center), and K_S-bands (bottom) for KMHK 105. (left) The luminosity functions of the cluster region. (center) The luminosity functions of the field region. (right) The luminosity functions of the star cluster. The luminosity functions of the field region are subtracted from that of the cluster region. The fitting results with the equation (1.1) are shown by red lines.

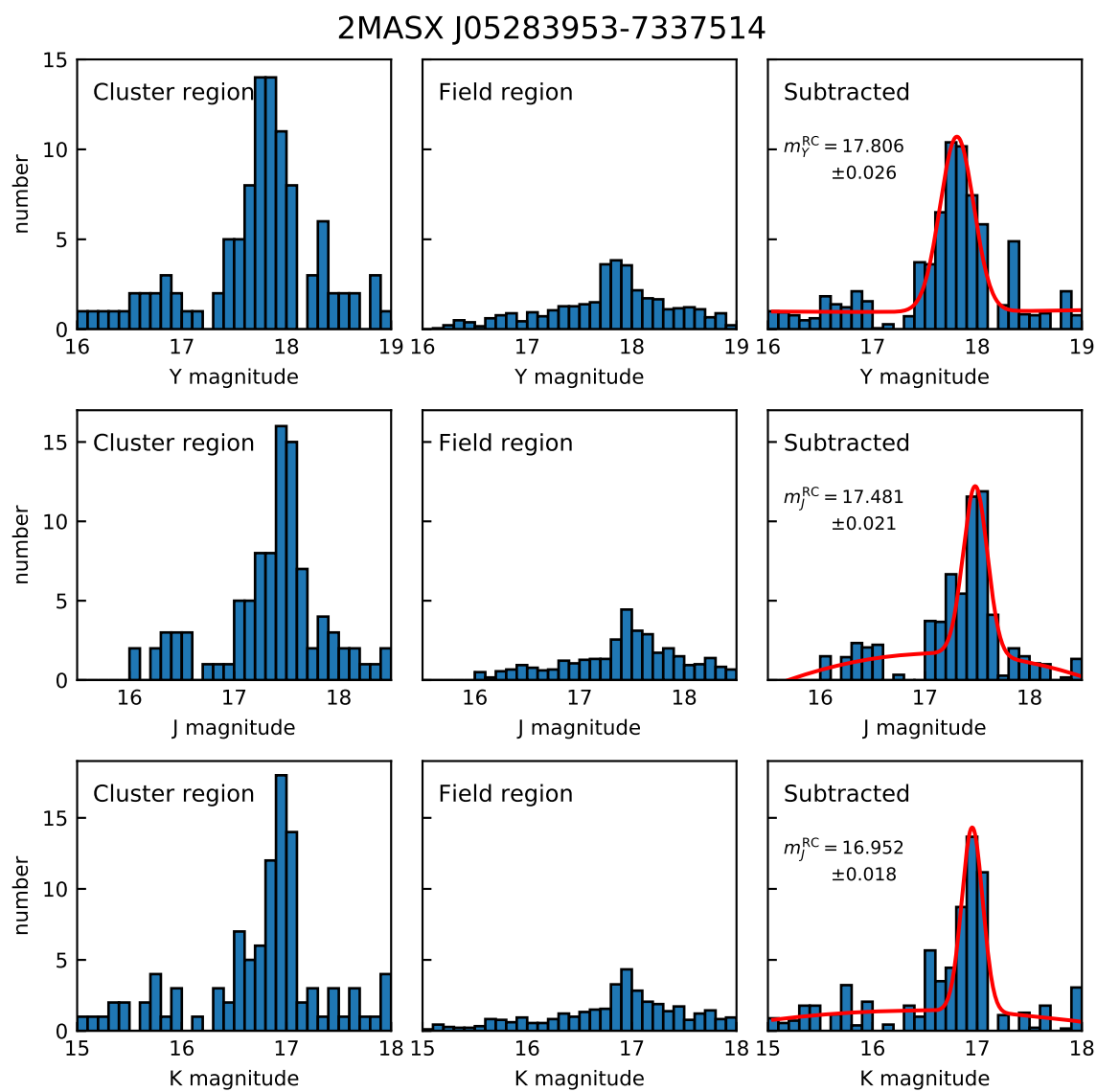


Figure 3.4: The same plot as Figure 3.3, but for 2MASX J05283953-7337514.

Table 3.2: The standard errors and the magnitude difference for other bin size fittings for IRSF data

Cluster name	Standard error			bin size of 0.05			bin size of 0.2		
	J	H	K_S	J	H	K_S	J	H	K_S
KMHK 21	0.017	0.029	0.026	0.028	0.015	0.028	0.078	0.016	0.014
KMHK 337	0.015	0.017	0.013	0.041	0.003	0.013	0.030	0.027	0.076
ESO 85-72	0.025	0.024	0.017	0.029	0.022	0.001	0.013	0.006	0.059
NGC 1997	0.014	0.015	0.015	0.028	0.001	0.016	0.000	0.039	0.082
IC 2140	0.020	0.019	0.019	0.017	0.010	0.008	0.019	0.002	0.003
KMHK 1281	0.011	0.011	0.014	0.004	0.003	0.011	0.020	0.044	0.013
NGC 2161	0.012	0.013	0.012	0.003	0.012	0.004	0.023	0.015	0.015
NGC 2155	0.011	0.010	0.018	0.005	0.029	0.018	0.000	0.007	0.016
ESO 121-3	0.018	0.015	0.024	0.003	0.007	0.012	0.005	0.004	0.016
NGC 2213	0.012	0.016	0.010	0.003	0.011	0.016	0.070	0.004	0.014

Table 3.3: The standard errors and the magnitude difference for other bin size fittings for VMC data

Cluster name	Standard error			bin size of 0.05			bin size of 0.2		
	Y	J	K_S	Y	J	K_S	Y	J	K_S
KMHK 105	0.018	0.018	0.022	0.020	0.011	0.021	0.066	0.081	0.036
2MASX J05283953-7337514	0.026	0.021	0.018	0.022	0.007	0.038	0.064	0.084	0.084

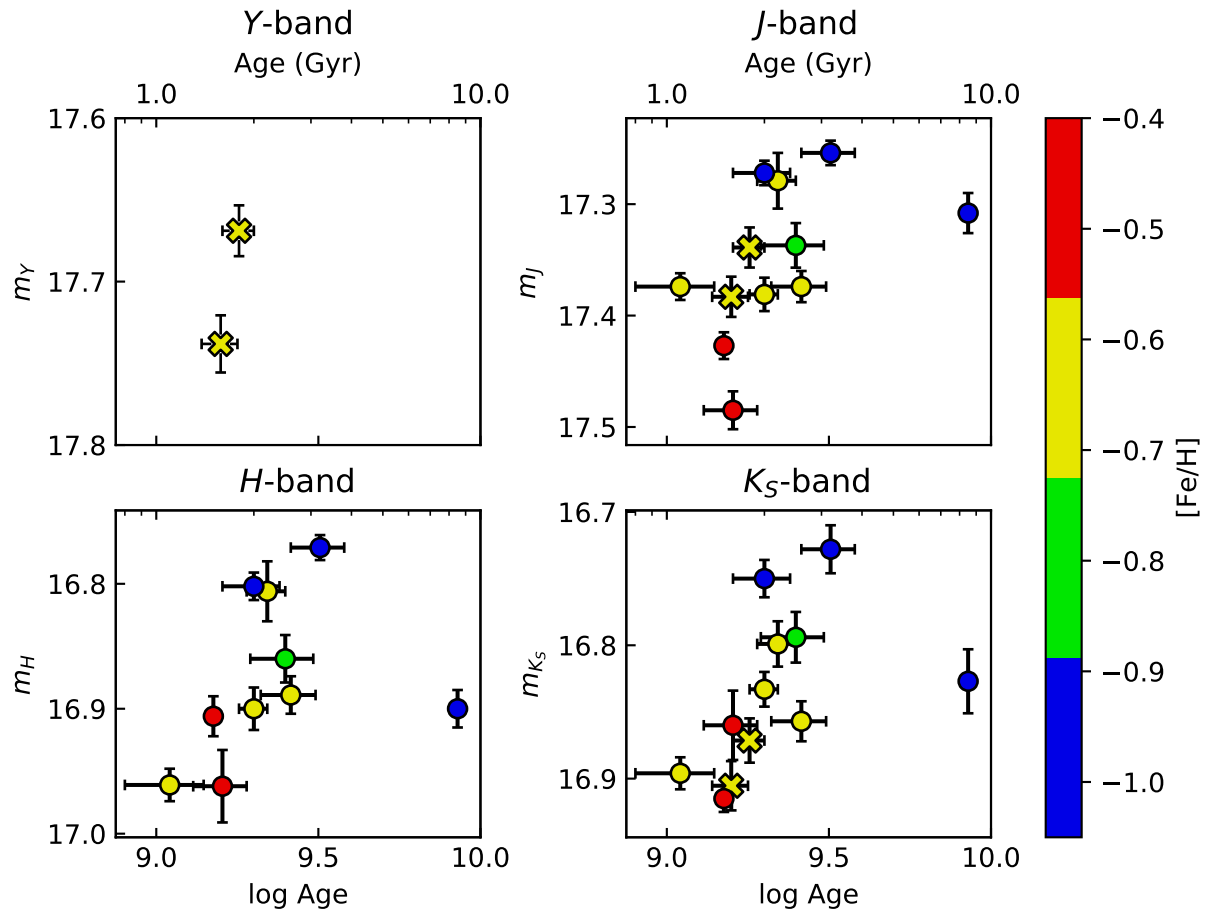


Figure 3.5: Mean RC magnitude versus age in the Y - (upper left), J - (upper right), H - (lower left), and K_S -bands (lower right). Circles represent the IRSF data, and crosses represent the VMC data. Metallicity differences are shown by color scales.

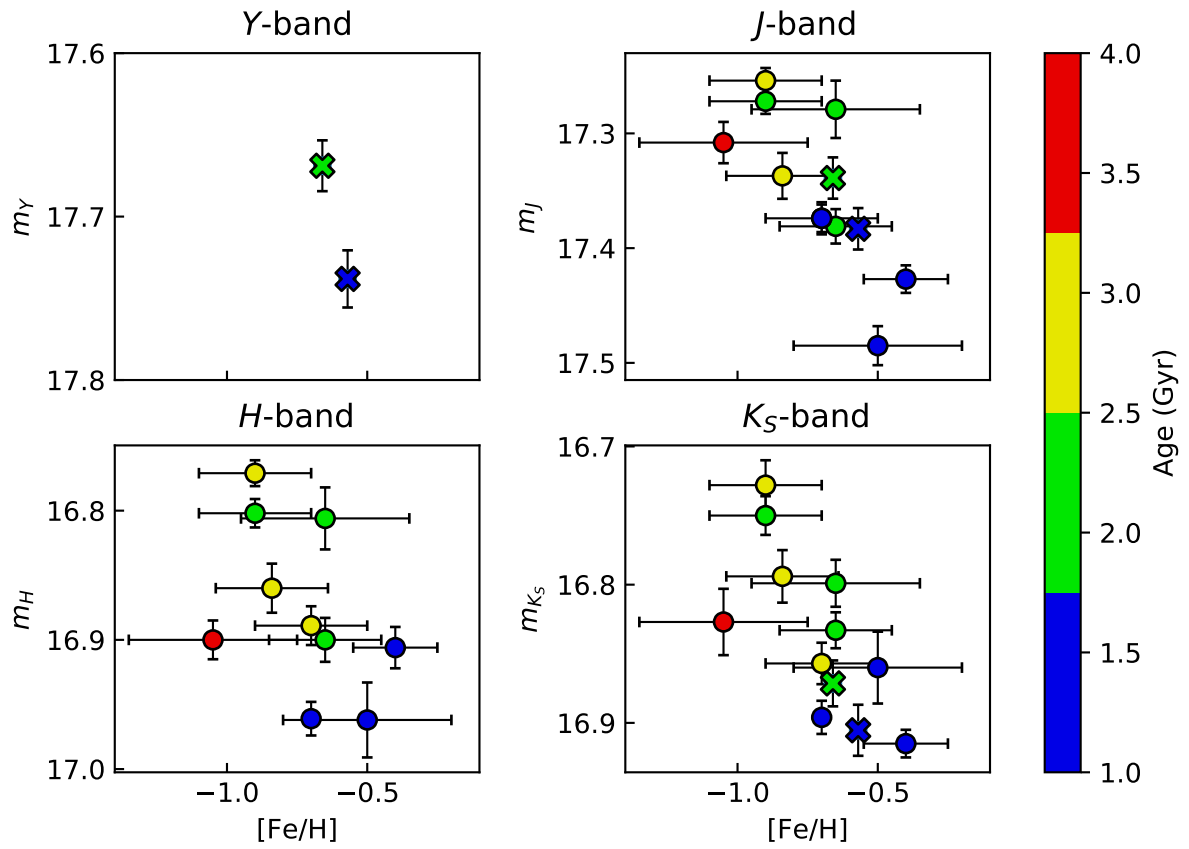


Figure 3.6: Mean RC magnitude versus metallicity in the Y - (upper left), J - (upper right), H - (lower left), and K_S -bands (lower right). The IRSF data are indicated by circles, and the VMC data are presented by the VMC data. Age differences are shown by color scales.

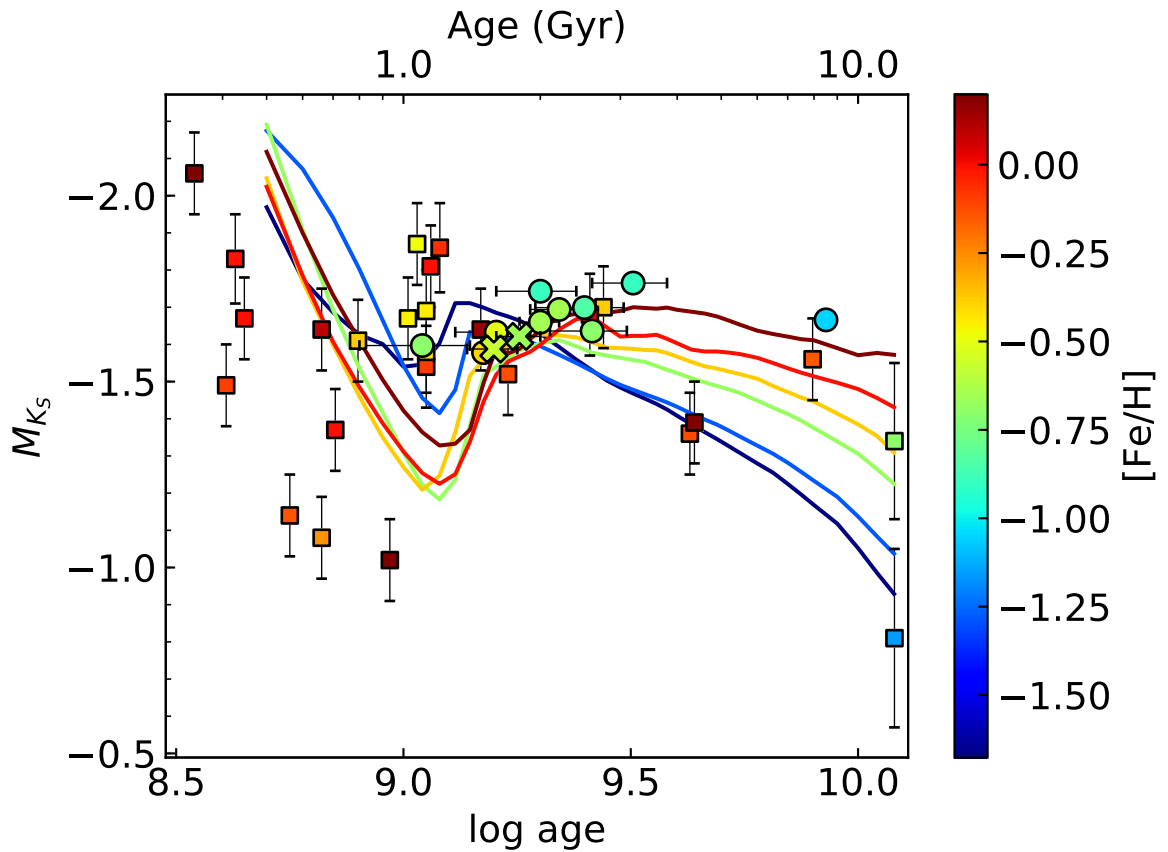


Figure 3.7: The comparison of K_S -band absolute magnitudes between model predictions and observations. Solid lines represent model prediction for some different metallicities from [Salaris & Girardi \(2002\)](#). Circles represent the IRSF data, squares are data from [van Helshoecht & Groenewegen \(2007\)](#), and crosses are the VMC data. Metallicity difference is illustrated by the color scale.

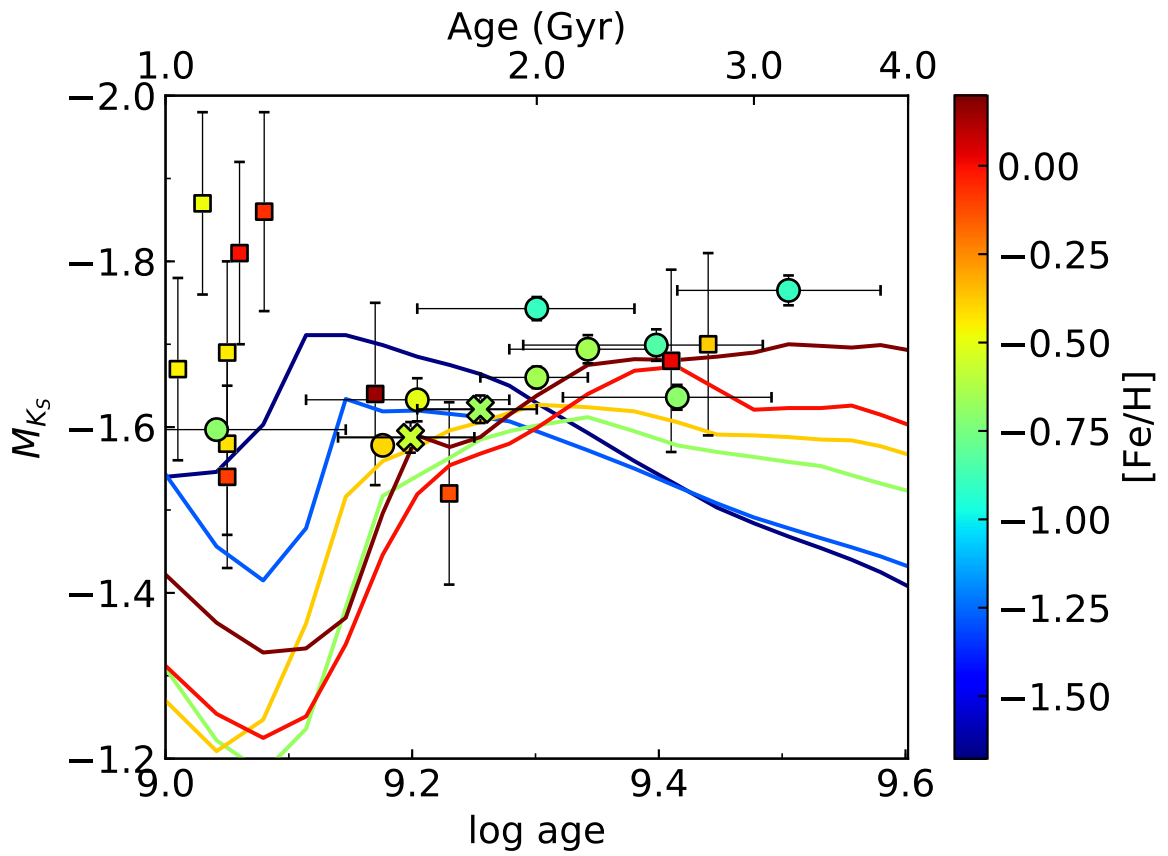


Figure 3.8: The same plot as Figure 3.7 but changing the plot range to focus on the samples between 1 and 3 Gyr.

seen in VJK -band data (Percival & Salaris 2003, although they have only three or four data points in the same age range) and in K -band data (Grocholski & Sarajedini 2002; van Helshoecht & Groenewegen 2007) for the Milky Way clusters. Theoretical models (Salaris & Girardi 2002; Girardi 2016) predict very similar trends to our results, although the individual values of absolute magnitudes are slightly different (Figure 3.7). Between 1.5 and 2.5 Gyr, our observational data are consistent with theoretical models within 0.1 mag. A slight deviation between observational data and the model prediction by Salaris & Girardi (2002) can be seen between 2.5 and 3.0 Gyr. However, our data is in good agreement with the model by Girardi (2016) between 2.5 and 3.0 Gyr, too.

For NGC 2161 (1.1 Gyr), our data show the brighter result compared to the theoretical models. However, the error of age is relatively large comparing the strong age dependence predicted by model predictions. Considering the relatively large error of age, our data are consistent with the models within the age error. The old cluster ESO 121-3 (8.5 Gyr) also deviate from the theoretical models. Theoretical models predict fainter absolute magnitudes for such an old and metal-poor RC stars. The mass loss before the CHeB phase is the one possible uncertainty source for old RC stars. However, much fainter absolute magnitudes are predicted when the mass loss is considered (Figure 1.35). Therefore, the mass loss cannot explain this deviation. Another possible reason is the quality of our data. The number of RC stars contained in ESO 121-3 is smaller compared to other clusters (Figures 2.9 and 3.2). The number of fainter stars is also small. For such an object, it is possible that the depth of the photometric data is not deep enough and the number of fainter stars are underestimated. If it is real, the fitting result would become brighter. This prediction matches the current situation. However, the difference between the observational data and the theoretical models is about 0.3 mag. It is unrealistic that the underestimation of faint stars changes the result so much. Therefore, the underestimation only is not enough to explain the deviation. Still another possibility is that the age of ESO 121-3 might not be correct. The age of this cluster was derived from the second method (equation 2.1). This method is powerful for intermediate-age clusters (1-3 Gyr), but not good for other age clusters because the number of RC stars becomes smaller for younger or older clusters. If the age of ESO 121-3 was overestimated, the deviation will be smaller.

The age dependence of $J - H$, $J - K_S$, and $H - K_S$ colors is shown in Figure 3.9. In this figure, $J - H$, and $J - K_S$ colors show weak age dependence that the older RC stars have redder colors between 1 and 3 Gyr. On the other hand, $H - K_S$ color does not show age dependence. These trends are similar to model predictions (Figure 3.10). The theoretical models predict that metal-poor and young (< 1.5 Gyr) RC stars have strong age dependence of colors but metal-rich RC colors have weak age dependence in the young age range. On the other hand, metal-poor and older (> 1.5 Gyr) RC stars does not show age dependence of colors but metal-rich RC colors slightly depend on ages. In addition, the weakest age dependence is predicted for metallicities between -0.68 and -0.38 dex. Furthermore, the population effect becomes weaker at longer wavelengths. Comparing $V - K$ and $I - K$ colors of model predictions, our observational data show weak age dependence of colors.

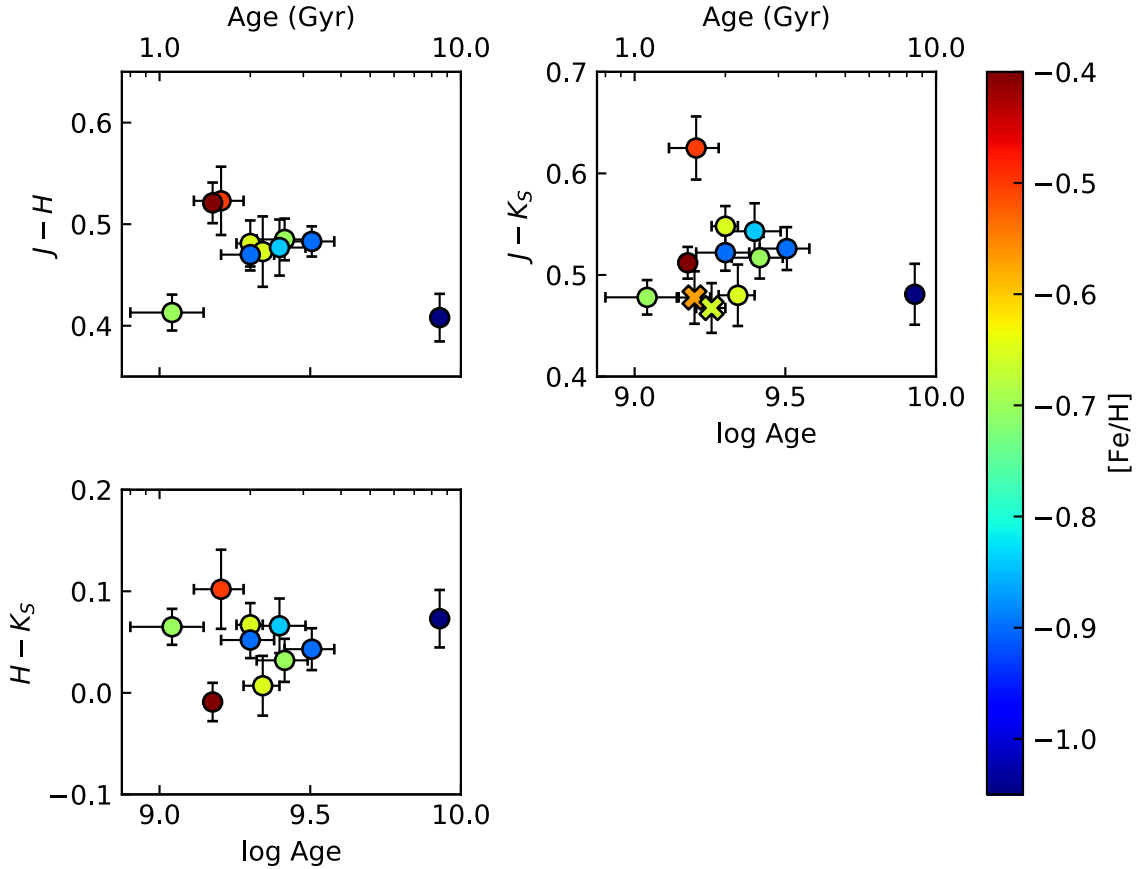


Figure 3.9: (Upper left) $J - H$, (Upper right) $J - K_S$, and (lower left) $H - K_S$ colors of RC stars as a function of age. Circles indicate the IRSF data, and crosses represent the VMC data. Metallicity difference is shown by color scales.

This result is consistent with the model prediction that the population effect becomes weaker at longer wavelengths. Moreover, older RC stars have redder colors between 1.0 and 3.0 Gyr in $J - H$, and $H - K$. It is predicted that the RC stars of this age region have the strongest age dependence, and consistent with our data.

Most of our sample clusters have the age of 1–3 Gyr where theoretical models predict strong age dependence. This age dependence is clearly confirmed in our study, thanks to many samples in this narrow age range. For very young (< 1 Gyr) RC stars, theoretical models predict that younger RC stars have brighter magnitudes. However, such young star clusters do not meet our target selection criteria; they are expected to be very small or exist in the bar region, so we cannot investigate the trend in this study. The later release of VMC survey data plays an important role to investigate the dependence of very young RC stars.

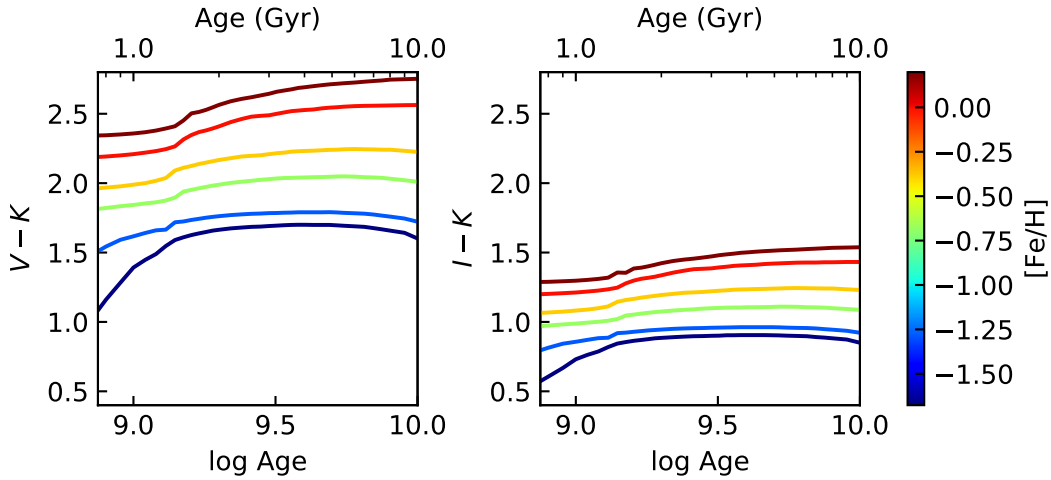


Figure 3.10: Model predictions for (left) $V - K$ and (right) $I - K$ color of RC stars as a function of age for several metallicities. The difference of metallicities are represented by (from blue to yellow, $[\text{Fe}/\text{H}] = -1.68, -1.28, -0.68, -0.38, 0.00,$ and 0.20). The model predictions are taken from [Girardi & Salaris \(2001, V and I-band\)](#) and [Salaris & Girardi \(2002, K-band\)](#).

3.2 Metallicity dependence

We can see metallicity dependence on m_Y, m_J, m_H and m_{K_S} (Figure 3.6). The predicted metallicity dependence in the K -band is only 0.1–0.2 magnitude around 2 Gyr, and this is smaller than those in the shorter wavelengths. The expected trend is that RC stars with lower metallicity have brighter magnitudes; this trend can be seen in our results (Figure 3.6). The magnitude difference found in our sample is about 0.2 mag, and this matches very well with the theoretical prediction. Due to the small number of clusters in this age range, it has been difficult to investigate this dependence in the past works. To our knowledge, this is the first study which confirmed the metallicity dependence of the RC magnitudes in the age range of 1–3 Gyr.

To investigate the metallicity dependence more precisely, we divided our samples into younger RC stars (1–2 Gyr) and older RC stars (2–4 Gyr, Figure 3.11). In the latter age range, the predicted metallicity dependence is different in two models: [Salaris & Girardi \(2002\)](#) predicts that metal-rich RC stars have brighter K -band absolute magnitudes but [Girardi \(2016\)](#) obtained contrary results. The K_S -band absolute magnitudes of our data show the trend that more metal-rich RC stars have fainter magnitudes between 2 and 4 Gyr. This result matches the prediction by [Girardi \(2016\)](#). In optical wavelengths, both models predict that more metal-rich RC stars have fainter absolute magnitudes, and the metallicity dependence becomes stronger for shorter wavelengths. Our J - and H -band data also show metal-rich RC stars have faint absolute magnitudes. Unfortunately, model calculations for J - and H -band has not been performed. Therefore, we cannot compare this

behavior with model predictions. However, this trend is the same as the predictions for V - and I -band or K_S -band by [Girardi \(2016\)](#). The strength of the metallicity dependence is not so different among J -, H -, and K_S -band in our data.

The metallicity dependence of $J - H$, $J - K_S$, and $H - K_S$ colors is presented in [Figure 3.12](#). $J - H$ color shows the clear trend that metal-rich RC stars have redder colors. This trend is consistent with the model predictions ([Figure 3.10](#)). The difference of $J - K_S$ colors is ~ 0.1 mag and much smaller than that predicted for optical colors (~ 0.5 mag for $V - K$ colors and ~ 0.3 mag for $I - K$ colors). This result matches the model predictions that the metallicity dependence becomes weaker at longer wavelengths. On the other hand, $J - K_S$, and $H - K_S$ colors do not show strong metallicity dependence. For $H - K_S$ colors, it is not surprising that the colors are not much affected by the metallicity difference because weaker metallicity dependence is predicted for longer wavelengths. However, it is unexpected that $J - K_S$ colors have nearly constant values. This constant values can be explained by the relations between the age and metallicity of our sample RC stars. We can see the age-metallicity relation that older star clusters are more metal-poor in our sample star clusters ([Figure 2.2](#)). In the model predictions, older RC stars have redder colors, and metal-rich RC stars have redder colors. Therefore, the population effects for RC colors are canceled like young (bluer) and metal-rich (redder) or old (redder) and metal-poor (bluer) RC stars.

3.3 Absolute magnitude

The averages of the apparent RC magnitudes for our 10 (H -band) or 12 (J -, K_S -band) clusters are 17.355 ± 0.020 , 16.876 ± 0.021 , and 16.838 ± 0.018 for m_J , m_H , and m_{K_S} , respectively. Considering the distance modulus to the LMC ($18.493 \pm 0.008 \pm 0.047$, [Pietrzyński et al. 2013](#)), absolute magnitudes of RC stars, M_J , M_H , and M_{K_S} become -1.138 ± 0.020 (this work's error) ± 0.008 ([Pietrzyński's](#) statistical) ± 0.047 ([Pietrzyński's](#) systematic), $-1.617 \pm 0.021 \pm 0.008 \pm 0.047$, and $-1.655 \pm 0.018 \pm 0.008 \pm 0.047$, respectively. These results give good agreement with previous works in the K_S -band within the errors, but 0.05-0.2 mag brighter than previous studies derived from RC stars in the solar neighborhood or Kepler field in J - and H -band ([Laney et al. 2012](#); [Chen et al. 2017](#); [Hawkins et al. 2017](#); [Ruiz-Dern et al. 2018](#)).

[Laney et al. \(2012\)](#) pointed out that the distance modulus to the LMC derived from J -band RC magnitudes were about 0.1 mag smaller than that from H - or K_S -band RC magnitudes. Our results confirm this suggestion. [Laney et al. \(2012\)](#) suggested that the discrepancy is probably caused by the population effect. Both theoretical models and observations have confirmed that the population effects become stronger in the shorter wavelengths. $J - K_S$ colours of RC stars in our target clusters are 0.47-0.63 mag ([Table 2.3](#)), and bluer than those in solar neighborhood (0.629; [Laney et al. 2012](#)) or in Baade's Window (0.68; [Gonzalez et al. 2012](#)). Theoretical models predict that metal-poor RC stars have bluer colour than metal-rich RC stars because of the stronger population effect in the shorter wavelengths. $J - K_S$ colors of our sample RC stars do not show the

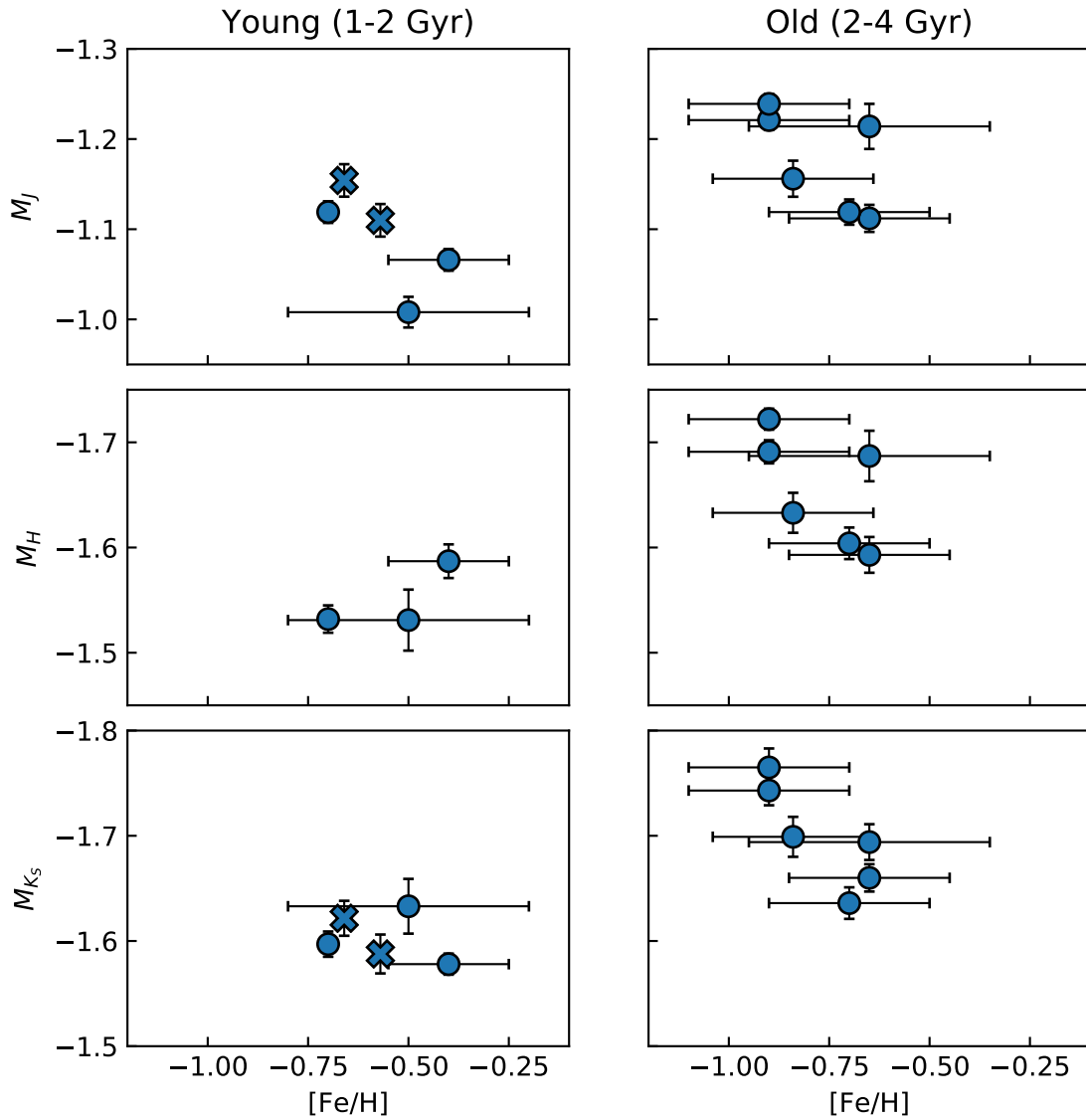


Figure 3.11: Mean magnitude versus metallicity for (left) younger (1–2 Gyr) and (right) older (2–4 Gyr) RC stars in the J - (upper), H - (center), and K_S -bands (bottom). The IRSF data are represented by circles and the VMC data are crosses.

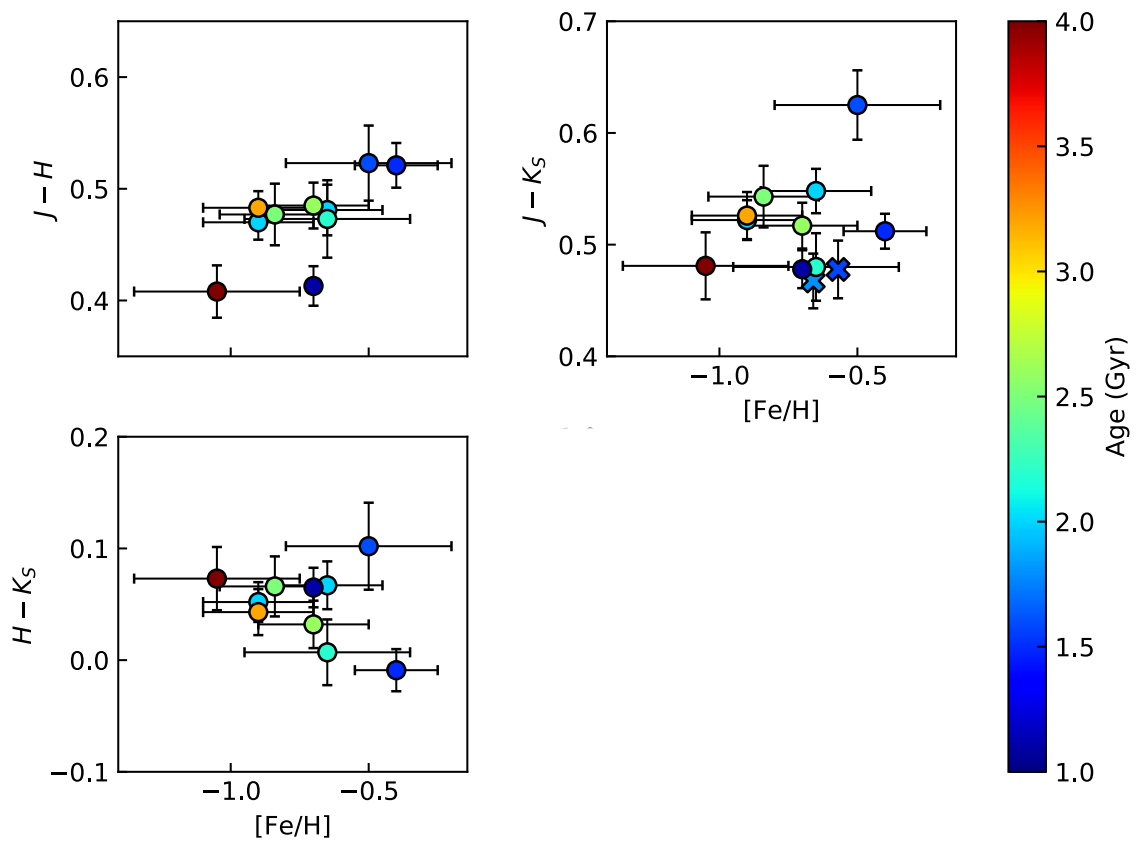


Figure 3.12: (Upper left) $J-H$, (Upper right) $J-K_S$, and (lower left) $H-K_S$ colors of RC stars as a function of metallicity. The IRSF data are indicated by circles, and the VMC data are represented by crosses. Age difference is shown by color scales.

strong metallicity dependence but the population effect of these RC stars might be canceled out because of the age-metallicity relation (Figure 3.12). In $J - H$ colors, we can see clear metallicity dependence and it confirms the influence of the population effect. Metallicities of RC stars in our target clusters are lower than those in the solar neighborhood or in Baade's Window. This result also supports that J -band population effect is stronger than K_S -band. Figure 3.6 also indicates that the population effect in the J -band is slightly stronger than that in the K_S -band. Therefore, the discrepancy in the J -band is probably caused by the population effects.

3.4 RC stars as a standard candle

So far, the population effect of RC absolute magnitudes has been corrected using theoretical models. To obtain the empirical relations, we fit our observational data with the following function

$$M_\lambda = a \log t + b[\text{Fe}/\text{H}] + c, \quad (3.1)$$

where t is the age (yr) of the star clusters. We used RC stars in 11 clusters except an old cluster, ESO 121-3 for the fitting because the behavior of the old cluster is completely different from the young clusters. As the best fit results, we obtained

$$M_J = -(0.087 \pm 0.136) \log t + (0.310 \pm 0.112)[\text{Fe}/\text{H}] - (0.120 \pm 1.217) \quad (3.2)$$

$$M_H = (-0.277 \pm 0.143) \log t + (0.136 \pm 0.117)[\text{Fe}/\text{H}] + (1.048 \pm 1.284) \quad (3.3)$$

$$M_{K_S} = (-0.201 \pm 0.096) \log t + (0.230 \pm 0.079)[\text{Fe}/\text{H}] + (0.369 \pm 0.859). \quad (3.4)$$

The adjusted coefficients of determination (adjusted R^2) are 0.578, 0.537, and 0.743, and these values are calculated by

$$\text{adjusted } R^2 = 1 - \frac{\sum_i (M_{\lambda,i} - f_i)^2 / (N - p - 1)}{\sum_i (M_{\lambda,i} - \overline{M}_\lambda)^2 / (N - 1)}, \quad (3.5)$$

where M_λ is the absolute magnitudes of observational data in the λ -band, f is the absolute magnitudes derived from equations (3.2)–(3.4), \overline{M}_λ is the mean value of M_λ , N is the number of sample clusters (nine in this time), and p is the number of explanatory variables (three in this time). The adjusted R^2 gets closer to one for the better fitting. If the adjusted R^2 is negative, the fitting is worse than just taking the average value. We also fitted our data with higher order polynomial functions but adjusted R^2 values are worse than fitting with equation (3.1). The root mean squares (RMSs) of the difference between the observational data and the fitting results are 0.041, 0.038, and 0.028 for M_J , M_H , and M_{K_S} , respectively. Figures 3.13 and 3.14 show the distribution of absolute magnitudes with fitted lines. The population effect of RC stars with the ages of 1.5–3.5 Gyr and the metallicities from -0.90 to -0.40 dex can be corrected with these relations. Within these ages and metallicities, observational data show good agreement with the prediction of Girardi (2016)

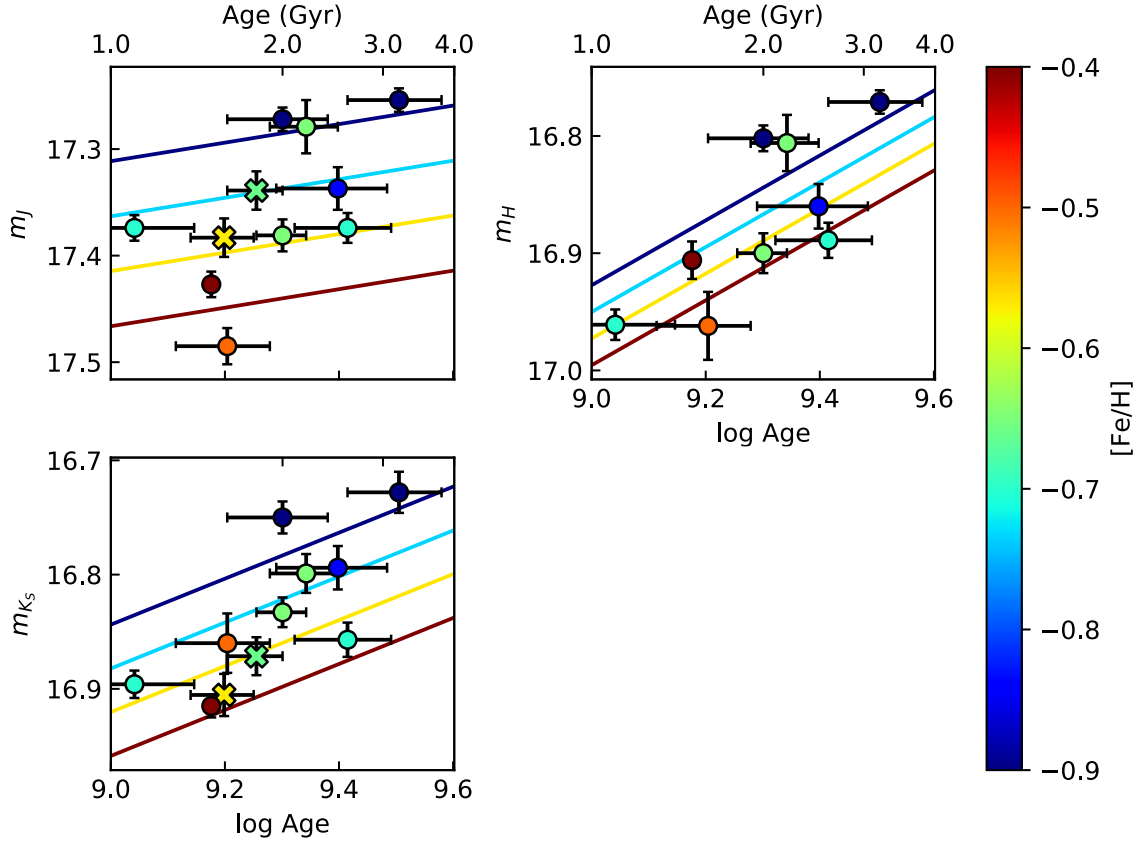


Figure 3.13: Mean RC magnitude versus age in the J - (Upper left), H - (Upper right), and K_S -band (lower left). The best-fit relations are also plotted for four metallicities (from blue to brown, -0.90 , -0.73 , -0.57 , -0.40 dex). Circles indicate the IRSF data, and crosses represent the VMC data. Metallicity difference is shown by color scales.

model. So far, it is difficult to derive the ages of RC stars. However, asteroseismology allows us to obtain the ages of individual RC stars. Recently, a way to estimate asteroseismic parameters from single-epoch optical or NIR spectra has been proposed (Hawkins et al. 2018; Ting et al. 2018). By using this technique, we can obtain the ages of many RC stars in field regions, and accurate distance determination for various regions cloud be possible.

As can be seen in Figure 2.2, the ages of clusters are correlated with the metallicities (the correlation coefficient is -0.635 for the nine clusters used for the fitting). Therefore, it is possible that multicollinearity occurs. To check the presence of multicollinearity, we calculated partial correlation coefficients. The partial correlation coefficients between ages and absolute magnitudes are -0.283 , -0.585 , and -0.494 , and the partial correlation coefficients between metallicities and absolute magnitudes are 0.684 , 0.384 , and 0.549 for J -, H -, and K_S -bands, respectively. This means that absolute magnitude depends on both age and metallicity. The correlation coefficients between

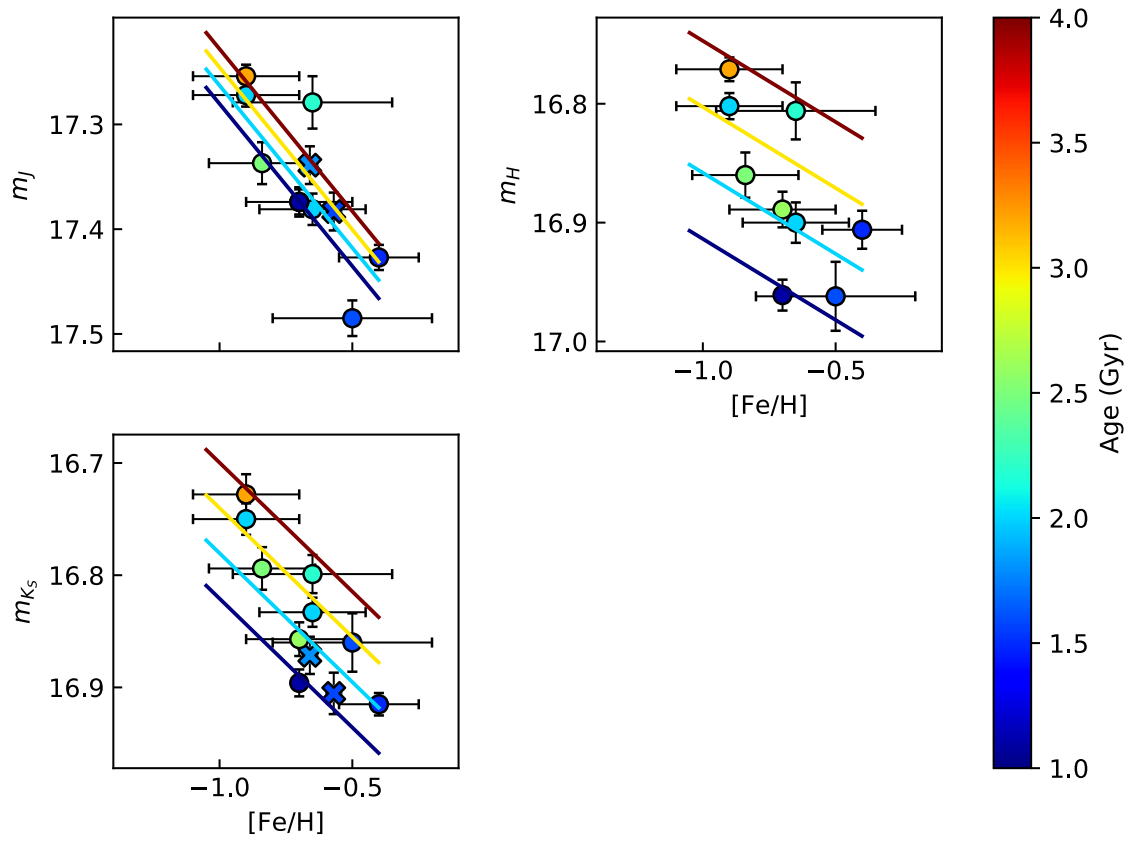


Figure 3.14: Mean RC magnitude versus metallicity in the J - (Upper left), H - (Upper right), and K_S -band (lower left). The best-fit relations are also plotted for four ages (from blue to brown, $\log t = 9.0, 9.2, 9.4, 9.6$). Circles indicate the IRSF data, and crosses represent the VMC data. Age difference is shown by color scales.

ages and absolute magnitudes are -0.626 , -0.752 , and -0.741 , and the correlation coefficients between metallicities and absolute magnitudes are 0.805 , 0.660 , and 0.741 for J -, H -, and K_S -bands, respectively. These correlation coefficients have the same signs as the partial correlation coefficients, and the values are comparable. Furthermore, the correlation coefficients have the same signs as the regression coefficients a and b . Therefore, multicollinearity does not matter much.

Unfortunately, there is no cluster younger than 1 Gyr in our sample. Within the data from [van Helshoecht & Groenewegen \(2007\)](#), RC stars with younger age have large scatter of absolute magnitudes. The observational data also show large discrepancy with the model prediction (Figures 3.7). Thus, it is difficult to correct the population effect for such young RC stars. This could be a problem because the length of core helium-burning phase is longer for the stars between 1 and 4 Gyr, and the fraction of young RC stars is high unlike the main-sequence stars, if a galaxy has a relatively constant star formation rate. As a result, this leads to the large misestimation of distance. Therefore, it needs to distinguish such young RC stars from older ones. The most accurate way to separate young RC stars is asteroseismology. Using two asteroseismic parameters, the average large frequency separation, $\Delta\nu$, and period spacing, ΔP , we can distinguish red giant branch (RGB) stars, old RC stars (primary RC), and young RC stars (secondary RC, [Bedding et al. 2011](#)). The difference in these parameters is caused by different internal structures. We can not only distinguish these three type of stars, but also obtain the age of RC stars from asteroseismic data. The weak point of the asteroseismology is that very accurate photometry with space telescopes, such as *CoRoT*, *Kepler*, and *TESS* is required to obtain asteroseismic parameters, and then the region where we can obtain very accurate photometric data is quite limited. However, as described above, single-epoch spectra can be used to estimate asteroseismic parameters. This technique could be applied to more wider regions. If spectroscopic data cannot be obtained, one possible way to identify young RC stars is using color information. The theoretical model predicts bluer color for young RC stars. However, metal-poor RC stars also have the bluer color. Therefore, we need to obtain metallicity information independently to use color for identifying young RC stars.

There is only one cluster older than 1 Gyr in our sample. The number of star clusters analyzed by [van Helshoecht & Groenewegen \(2007\)](#) is also small. Combined with the data from [van Helshoecht & Groenewegen \(2007\)](#), some scatter can be seen in RC stars older than 3.5 Gyr. Some discrepancy between the model prediction and observational data also can be seen. [Girardi \(2016\)](#) mentioned that models predict systematically ~ 0.2 mag brighter than observational data, and this discrepancy can be reduced down to ~ 0.1 mag if the mass loss is considered. On the other hand, [Chen et al. \(2017\)](#) obtained small scatter of K_S -band absolute magnitudes for old RC stars from asteroseismically derived ages. Considering these results, distance estimation using RC stars containing old ones would have 20 per cent uncertainty. If we do not take metallicity into account, this uncertainty would be large for metal-poor RC stars.

We also fits the RC colors with the form of equation (3.1), and obtained

$$J - H = (0.178 \pm 0.064) \log t + (0.179 \pm 0.053)[\text{Fe}/\text{H}] - (1.054 \pm 0.577) \quad (3.6)$$

$$J - K_S = (0.114 \pm 0.146) \log t + (0.080 \pm 0.120)[\text{Fe}/\text{H}] - (0.489 \pm 1.312) \quad (3.7)$$

$$H - K_S = (-0.092 \pm 0.110) \log t - (0.084 \pm 0.090)[\text{Fe}/\text{H}] + (0.842 \pm 0.990). \quad (3.8)$$

The adjusted R^2 values are 0.569, -0.153, -0.143. Figure 3.15 and 3.16 show th distribution of colors with the fitted lines. Comparing absolute magnitudes, the population effect for the colors are smaller. In particular, $J - K_S$ and $H - K_S$ have nearly constant values, $J - K_S = 0.512 \pm 0.015$ and $H - K_S = 0.050 \pm 0.010$, respectively. These values are used as the intrinsic RC colours at least within the ages of 1.1–3.2 Gyr and the $[\text{Fe}/\text{H}]$ of -0.90 to -0.40 dex. The partial correlation coefficients between ages and colors are 0.250 and -0.331 , and the partial correlation coefficients between metallicities and colors are 0.201 and -0.372 for $J - K_S$ and $H - K_S$, respectively. This also supports that these colours have no strong dependence of absolute magnitude on age and metallicity. These colours can be used as an interstellar extinction probe. The average value of $J - H$ is 0.473 ± 0.011 , although the population effect is slightly stronger. The partial correlation coefficients between ages and absolute magnitudes are 0.696, and the partial correlation coefficients between metallicities and absolute magnitudes are 0.781 for $J - H$. This means that $J - H$ colour depends on both age and metallicity. The RMS of the difference between the observational data and the fitting results is 0.017 for $J - H$ color. For more metal-rich RC stars, Laney et al. (2012) obtained $J - H = 0.506$, $J - K_S = 0.629$ and $H - K_S = 0.123$ in the solar neighborhood, and Gonzalez et al. (2012) derived $J - K_S = 0.68$ in Baade’s Window. These values are slightly higher than our results. Therefore, attention should be payed for applying these colors to RC stars with near solar metallicities.

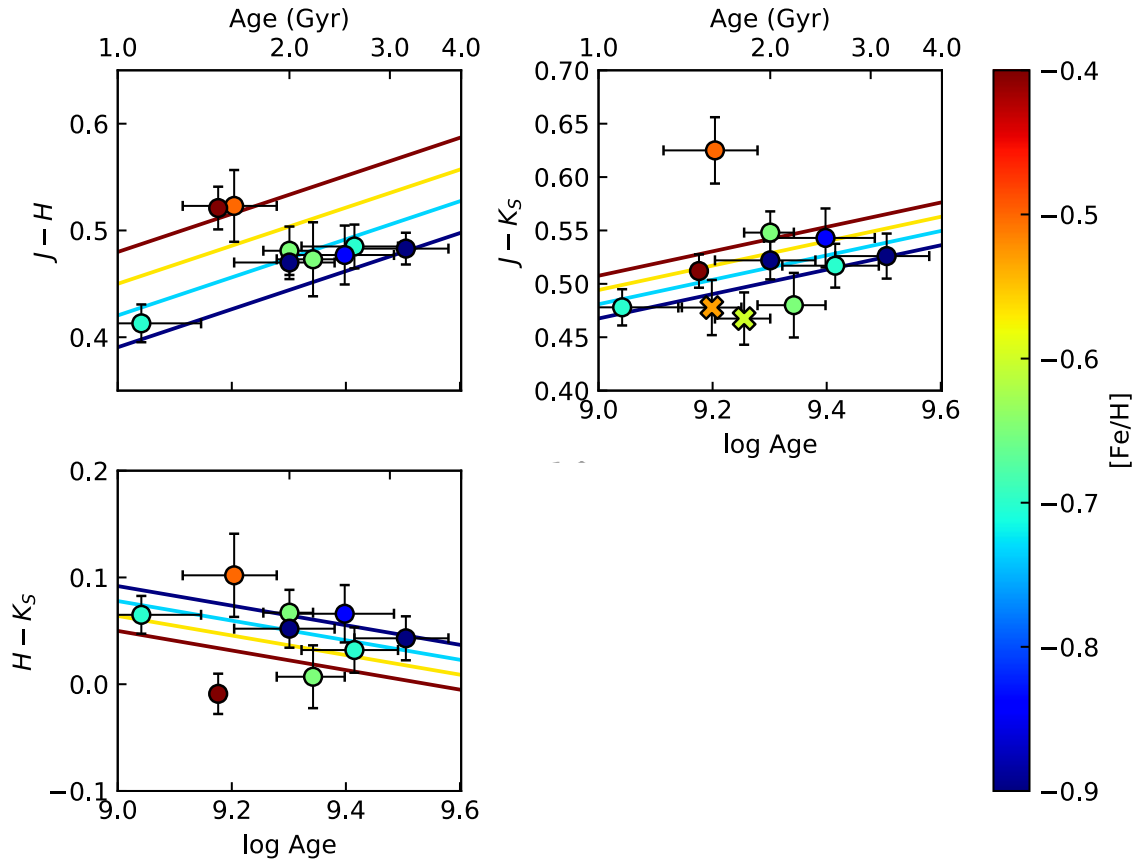


Figure 3.15: Mean RC color versus age for the $J-H$ (Upper left), $J-K_S$ (Upper right), and $H-K_S$ (lower left). The best-fit relations are also plotted for four metallicities (from blue to brown, -0.90 , -0.73 , -0.57 , -0.40 dex). Circles indicate the IRSF data, and crosses represent the VMC data. Metallicity difference is shown by color scales.

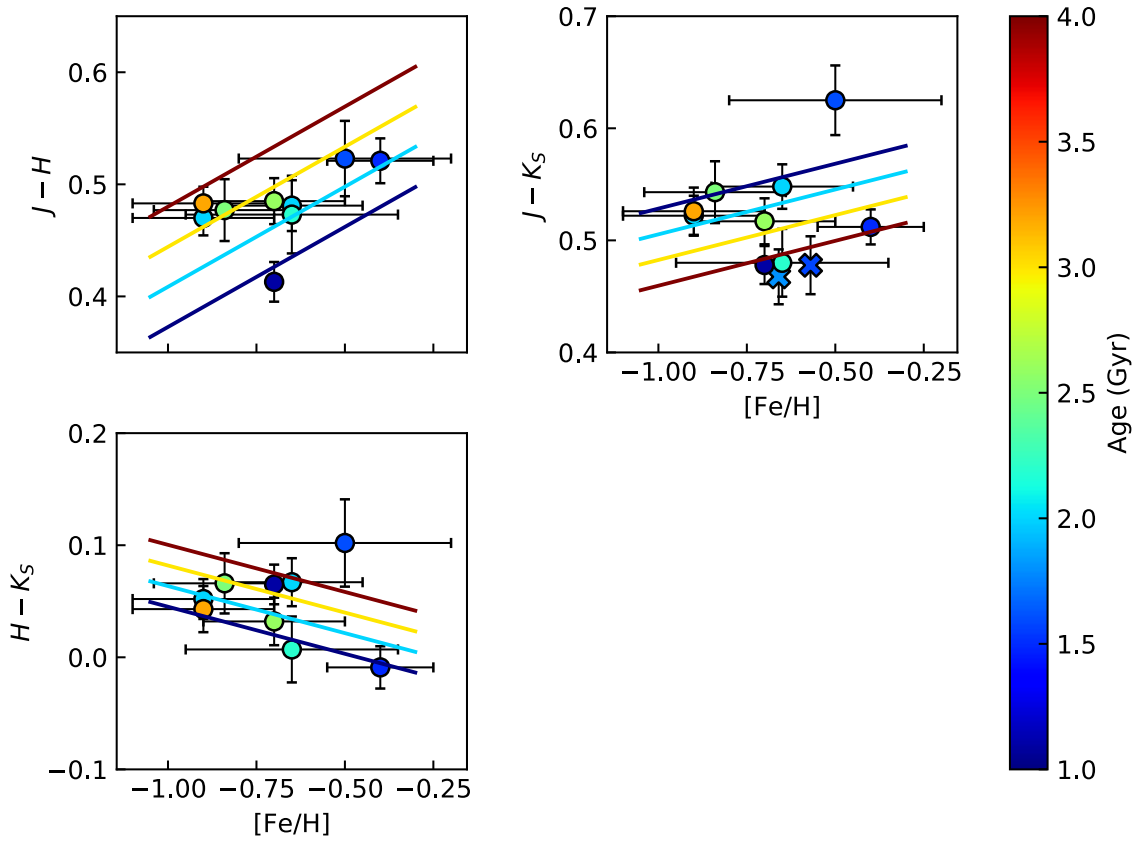


Figure 3.16: Mean RC color versus metallicity for the $J - H$ (Upper left), $J - K_S$ (Upper right), and $H - K_S$ (lower left). The best-fit relations are also plotted for four ages (from blue to brown, $\log t = 9.0, 9.2, 9.4, 9.6$). Circles indicate the IRSF data, and crosses represent the VMC data. The age difference is shown by color scales.

Chapter 4

Conclusions and future work

4.1 Conclusions

In this thesis, we investigate the age and metallicity dependence on the RC magnitudes, m_Y , m_J , m_H , and m_{K_S} , and their colors $J - H$, $J - K_S$, and $H - K_S$. We use IRSF/SIRIUS and VMC survey DR4 to obtain Y -, J -, H -, and K_S -band photometric data. Most of our samples consist of the clusters with young age and low metallicity. The age and metallicity are different from previously investigated clusters in the Milky Way. We fitted our observational data to the fitting function, and obtained the empirical relations to correct the population effect for the absolute magnitudes and colors of RC stars with the ages of 1.5–3.5 Gyr and the metallicities from -0.90 to -0.40 dex. In particular, we confirmed little population effect for $J - K_S$ and $H - K_S$ colors, and they can be used as the tracer of interstellar extinction. In model comparison, we confirmed that the prediction from [Girardi \(2016\)](#) models shows good agreement with our observational data between 1.5 and 3.5 Gyr. We divide our sample clusters into younger RC stars and older RC stars and find that the more metal-rich RC stars, the fainter they become. The averaged value of M_{K_S} is consistent with previous work for solar neighborhood RC stars, but M_J and M_H are slightly brighter. These discrepancy may be due to the population effect.

4.2 Future work

We confirmed the population effect for RC stars with the ages of 1.5–3.5 Gyr. However, RC stars with other ages have not yet investigated precisely. The later release of VMC survey can be used to investigate younger RC stars. For older RC stars, observations in the solar neighborhood may play an important role. The ages and metallicities of RC stars can be derived from single-epoch observations, and NIR photometry for bright stars is collected by InfraRed Thirty Millimeter Telescope. The information about distance can be obtained from *Gaia* data. Combining these data, we can investigate the population effect of the much larger number of RC stars. By using derived

relations and the spectroscopic technique to identify RC stars, individual RC stars can be used as a standard candles. Therefore, RC stars would be applied to much wider regions.

Acknowledgments

I would like to thank everyone who has supported my research. First of all, I would like to express the deepest appreciation to my supervisor, Assistant Professor Yoshifusa Ita. He has supported me for seven years. Without his persistent help and encouragement, I could not finish writing this dissertation.

I would like to express my gratitude to examiners, Professor Kazuyuki Omukai, Associate Professor Masaomi Tanaka, and Associate Professor Shogo Nishiyama. They gave me various constructive comments. Especially, discussions with Associate Professor Nishiyama in weekly Ita lab seminars helped improve this dissertation.

I also thank to the members of Ita laboratory, Hitomi Iwasaki, Takumi Hanaue, Takahiro Komiyama, Atsushi Iwamatsu, Ryosuke Morita, and Yuta Habasaki, and the members of Teiondo seminar, Professor Emeritus Yoshikazu Nakada, Associate Professor Hideyuki Izumiura, Associate Professor Toshiya Ueta, Assistant Professor Kenshi Yanagisawa, Assistant Professor Noriyuki Matsunaga, Dr. Hiroyuki Mito, Dr. Takafumi Kamizuka, and Dr. Kentaro Asano. These seminars provided me with the latest information about the studies of stars and got more motivated.

I am deeply grateful to all the members of the Astronomical Institute. Ms. Junko Nagasawa and Ms. Nozomi Okamoto supported my business trips, purchasing goods, and many other things. My contemporary, Jun Kumamoto listened to my problems and gave me some advice.

I thank the authors and the editor-in-chief of Annual Review of Astronomy and Astrophysics, Astronomy and Astrophysics, Monthly Notices of the Royal Astronomical Society, Nature, The Astronomical Journal, and The Astrophysical Journal for permission to use their figures in this dissertation.

This work was supported by Grant-in-Aid for Japan Society for the Promotion of Science Research Fellow Grant Number JP16J00865.

References

- Alonso-García, J., Minniti, D., Catelan, M., et al. 2017, *ApJ*, 849, L13
- Alves, D. R. 2000, *ApJ*, 539, 732
- Alves, D. R., Rejkuba, M., Minniti, D., & Cook, K. H. 2002, *ApJ*, 573, L51
- Bailey, S. I. 1902, *Annals of Harvard College Observatory*, 38, 1
- Bastian, N., & Lardo, C. 2018, *Annual Review of Astronomy and Astrophysics*, 56, 83
- Bedding, T. R., Mosser, B., Huber, D., et al. 2011, *Nature*, 471, 608
- Bica, E., Bonatto, C., Dutra, C. M., & Santos, J. F. C. 2008, *MNRAS*, 389, 678
- Blitz, L., & Spergel, D. N. 1991, *ApJ*, 379, 631
- Bressan, A., Marigo, P., Girardi, L., et al. 2012, *MNRAS*, 427, 127
- Burstein, D., & Heiles, C. 1982, *AJ*, 87, 1165
- Cabrera-Lavers, A., González-Fernández, C., Garzón, F., Hammersley, P. L., & López-Corredoira, M. 2008, *A&A*, 491, 781
- Cannon, R. D. 1970, *MNRAS*, 150, 111
- Canterna, R. 1976, *AJ*, 81, 228
- Cardelli, J. A., Clayton, G. C., & Mathis, J. S. 1989, *ApJ*, 345, 245
- Castellani, V., Degl'Innocenti, S., Girardi, L., et al. 2000, *A&A*, 354, 150
- Chen, Y. Q., Casagrande, L., Zhao, G., et al. 2017, *ApJ*, 840, 77
- Cho, H., Blakeslee, J. P., Chies-Santos, A. L., et al. 2016, *ApJ*, 822, 95
- Choudhury, S., Subramaniam, A., & Cole, A. A. 2016, *MNRAS*, 455, 1855
- Cioni, M. R. L., Clementini, G., Girardi, L., et al. 2011, *A&A*, 527, A116

REFERENCES

- Clariá, J. J., Piatti, A. E., Parisi, M. C., & Ahumada, A. V. 2007, *MNRAS*, 379, 159
- Cole, A. A. 1998, *ApJ*, 500, L137
- Dalcanton, J. J., Williams, B. F., Seth, A. C., et al. 2009, *The Astrophysical Journal Supplement Series*, 183, 67
- Dwek, E., Arendt, R. G., Hauser, M. G., et al. 1995, *ApJ*, 445, 716
- Ferraro, F. R., Dalessandro, E., Mucciarelli, A., et al. 2009, *Nature*, 462, 483
- Fitzpatrick, E. L. 1999, *Publications of the Astronomical Society of the Pacific*, 111, 63
- Gallart, C., Freedman, W. L., Mateo, M., et al. 1999, *ApJ*, 514, 665
- Gardiner, L. T., & Hawkins, M. R. S. 1991, *MNRAS*, 251, 174
- Geisler, D., Bica, E., Dottori, H., et al. 1997, *AJ*, 114, 1920
- Geisler, D., Claria, J. J., & Minniti, D. 1991, *AJ*, 102, 1836
- Geisler, D., Piatti, A. E., Bica, E., & Clariá, J. J. 2003, *MNRAS*, 341, 771
- Geisler, D., & Sarajedini, A. 1999, *AJ*, 117, 308
- Girardi, L. 2016, *ARA&A*, 54, 95
- Girardi, L., Bertelli, G., Bressan, A., et al. 2002, *A&A*, 391, 195
- Girardi, L., Bressan, A., Bertelli, G., & Chiosi, C. 2000, *Astronomy and Astrophysics Supplement Series*, 141, 371
- Girardi, L., Marigo, P., Bressan, A., & Rosenfield, P. 2013, *ApJ*, 777, 142
- Girardi, L., & Salaris, M. 2001, *MNRAS*, 323, 109
- Gonzalez, O. A., Rejkuba, M., Zoccali, M., et al. 2013, *A&A*, 552, A110
- . 2012, *A&A*, 543, A13
- Gonzalez, O. A., Zoccali, M., Debattista, V. P., et al. 2015, *A&A*, 583, L5
- Gonzalez, O. A., Minniti, D., Valenti, E., et al. 2018, *MNRAS*, 481, L130
- Gratton, R. G., Carretta, E., & Bragaglia, A. 2012, *Astronomy and Astrophysics Review*, 20, 50
- Grocholski, A. J., & Sarajedini, A. 2002, *AJ*, 123, 1603
- Groenewegen, M. A. T. 2008, *A&A*, 488, 935

-
- Han, D., & Lee, Y.-W. 2018, in IAU Symposium, Vol. 334, *Rediscovering Our Galaxy*, ed. C. Chiappini, I. Minchev, E. Starkenburg, & M. Valentini, 263–264
- Haschke, R., Grebel, E. K., & Duffau, S. 2011, *AJ*, 141, 158
- Hawkins, K., Leistedt, B., Bovy, J., & Hogg, D. W. 2017, *MNRAS*, 471, 722
- Hawkins, K., Ting, Y.-S., & Walter-Rix, H. 2018, *ApJ*, 853, 20
- Holtzman, J. A., Smith, G. H., & Grillmair, C. 2000, *AJ*, 120, 3060
- Holtzman, J. A., Gallagher, John S., I., Cole, A. A., et al. 1999, *AJ*, 118, 2262
- Joo, S.-J., Lee, Y.-W., & Chung, C. 2017, *ApJ*, 840, 98
- Kato, D., Nagashima, C., Nagayama, T., et al. 2007, *Publications of the Astronomical Society of Japan*, 59, 615
- Koerwer, J. F. 2009, *AJ*, 138, 1
- Laney, C. D., Joner, M. D., & Pietrzyński, G. 2012, *MNRAS*, 419, 1637
- Lee, Y.-W., & Jang, S. 2016, *ApJ*, 833, 236
- Lee, Y. W., Joo, J. M., Sohn, Y. J., et al. 1999, *Nature*, 402, 55
- Lee, Y.-W., Joo, S.-J., & Chung, C. 2015, *MNRAS*, 453, 3906
- Lejeune, T., & Schaerer, D. 2001, *A&A*, 366, 538
- Li, Z.-Y., & Shen, J. 2012, *ApJ*, 757, L7
- López-Corredoira, M., Cabrera-Lavers, A., & Gerhard, O. E. 2005, *A&A*, 439, 107
- Matsunaga, N., Feast, M. W., Kawadu, T., et al. 2013, *MNRAS*, 429, 385
- McQuinn, K. B. W., Skillman, E. D., Dolphin, A., et al. 2015, *ApJ*, 812, 158
- McWilliam, A., & Zoccali, M. 2010, *ApJ*, 724, 1491
- Minniti, D., Lucas, P. W., Emerson, J. P., et al. 2010, *New A*, 15, 433
- Nagashima, C., Nagayama, T., Nakajima, Y., et al. 1999, in *Star Formation 1999*, ed. T. Nakamoto, 397–398
- Nagayama, T., Nagashima, C., Nakajima, Y., et al. 2003, in *Proc. SPIE*, Vol. 4841, *Instrument Design and Performance for Optical/Infrared Ground-based Telescopes*, ed. M. Iye & A. F. M. Moorwood, 459–464

REFERENCES

- Nataf, D. M., Udalski, A., Gould, A., Fouqué, P., & Stanek, K. Z. 2010, *ApJ*, 721, L28
- Nataf, D. M., Gould, A., Fouqué, P., et al. 2013, *ApJ*, 769, 88
- Nataf, D. M., Udalski, A., Skowron, J., et al. 2015, *MNRAS*, 447, 1535
- Ness, M., & Lang, D. 2016, *AJ*, 152, 14
- Nishiyama, S., Nagata, T., Tamura, M., et al. 2008, *ApJ*, 680, 1174
- Nishiyama, S., Tamura, M., Hatano, H., et al. 2009, *ApJ*, 696, 1407
- Nishiyama, S., Nagata, T., Baba, D., et al. 2005, *ApJ*, 621, L105
- Nishiyama, S., Nagata, T., Kusakabe, N., et al. 2006a, *ApJ*, 638, 839
- Nishiyama, S., Nagata, T., Sato, S., et al. 2006b, *ApJ*, 647, 1093
- Paczyński, B., & Stanek, K. Z. 1998, *ApJ*, 494, L219
- Palma, T., Gramajo, L. V., Clariá, J. J., et al. 2016, *A&A*, 586, A41
- Peng, E. W., Ferguson, H. C., Goudfrooij, P., et al. 2011, *ApJ*, 730, 23
- Percival, S. M., & Salaris, M. 2003, *MNRAS*, 343, 539
- Piatti, A. E., & Bica, E. 2012, *MNRAS*, 425, 3085
- Piatti, A. E., Clariá, J. J., Parisi, M. C., & Ahumada, A. V. 2009, *New A*, 14, 97
- Pietrzyński, G., Graczyk, D., Gieren, W., et al. 2013, *Nature*, 495, 76
- Renzini, A., D'Antona, F., Cassisi, S., et al. 2015, *MNRAS*, 454, 4197
- Rieke, G. H., & Lebofsky, M. J. 1985, *ApJ*, 288, 618
- Romaniello, M., Salaris, M., Cassisi, S., & Panagia, N. 2000, *ApJ*, 530, 738
- Ruiz-Dern, L., Babusiaux, C., Arenou, F., Turon, C., & Lallement, R. 2018, *A&A*, 609, A116
- Saha, A., Olszewski, E. W., Brondel, B., et al. 2010, *AJ*, 140, 1719
- Salaris, M., & Girardi, L. 2002, *MNRAS*, 337, 332
- Seidel, E., Demarque, P., & Weinberg, D. 1987, *The Astrophysical Journal Supplement Series*, 63, 917
- Skrutskie, M. F., Cutri, R. M., Stiening, R., et al. 2006, *AJ*, 131, 1163

- Smecker-Hane, T. A., Cole, A. A., Gallagher, John S., I., & Stetson, P. B. 2002, *ApJ*, 566, 239
- Smecker-Hane, T. A., Stetson, P. B., Hesser, J. E., & Lehnert, M. D. 1994, *AJ*, 108, 507
- Stanek, K. Z. 1996, *ApJ*, 460, L37
- Stanek, K. Z., Mateo, M., Udalski, A., et al. 1994, *ApJ*, 429, L73
- Stanek, K. Z., Udalski, A., Szymański, M., et al. 1997, *ApJ*, 477, 163
- Stanek, K. Z., Zaritsky, D., & Harris, J. 1998, *ApJ*, 500, L141
- Subramaniam, A. 2005, *A&A*, 430, 421
- Subramanian, S., & Subramaniam, A. 2009, *A&A*, 496, 399
- Sumi, T. 2004, *MNRAS*, 349, 193
- Sweigart, A. V., Greggio, L., & Renzini, A. 1990, *ApJ*, 364, 527
- Tatton, B. L., van Loon, J. T., Cioni, M. R., et al. 2013, *A&A*, 554, A33
- Ting, Y.-S., Hawkins, K., & Rix, H.-W. 2018, *ApJ*, 858, L7
- Udalski, A. 2000, *ApJ*, 531, L25
- . 2003, *ApJ*, 590, 284
- Udalski, A., Szymanski, M., Kaluzny, J., et al. 1993, *Acta Astron.*, 43, 289
- Udalski, A., Szymanski, M., Kaluzny, J., Kubiak, M., & Mateo, M. 1992, *Acta Astron.*, 42, 253
- Udalski, A., Szymanski, M., Kubiak, M., et al. 1998, *Acta Astron.*, 48, 1
- Udalski, A., Szymanski, M., Stanek, K. Z., et al. 1994, *Acta Astron.*, 44, 165
- Udalski, A., Szymanski, M., Kubiak, M., et al. 2002, *Acta Astron.*, 52, 217
- van Helshoecht, V., & Groenewegen, M. A. T. 2007, *A&A*, 463, 559
- Wegg, C., & Gerhard, O. 2013, *MNRAS*, 435, 1874
- Whitelock, P., & Catchpole, R. 1992, in *Astrophysics and Space Science Library*, Vol. 180, The Center, Bulge, and Disk of the Milky Way, ed. L. Blitz, 103–110
- Williams, B. F., Lang, D., Dalcanton, J. J., et al. 2014, *The Astrophysical Journal Supplement Series*, 215, 9
- Wozniak, P. R., & Stanek, K. Z. 1996, *ApJ*, 464, 233

Appendix A

Density maps of VMC survey tiles

Figures [A.1](#) to [A.5](#) show the star density maps of VMC survey tiles.

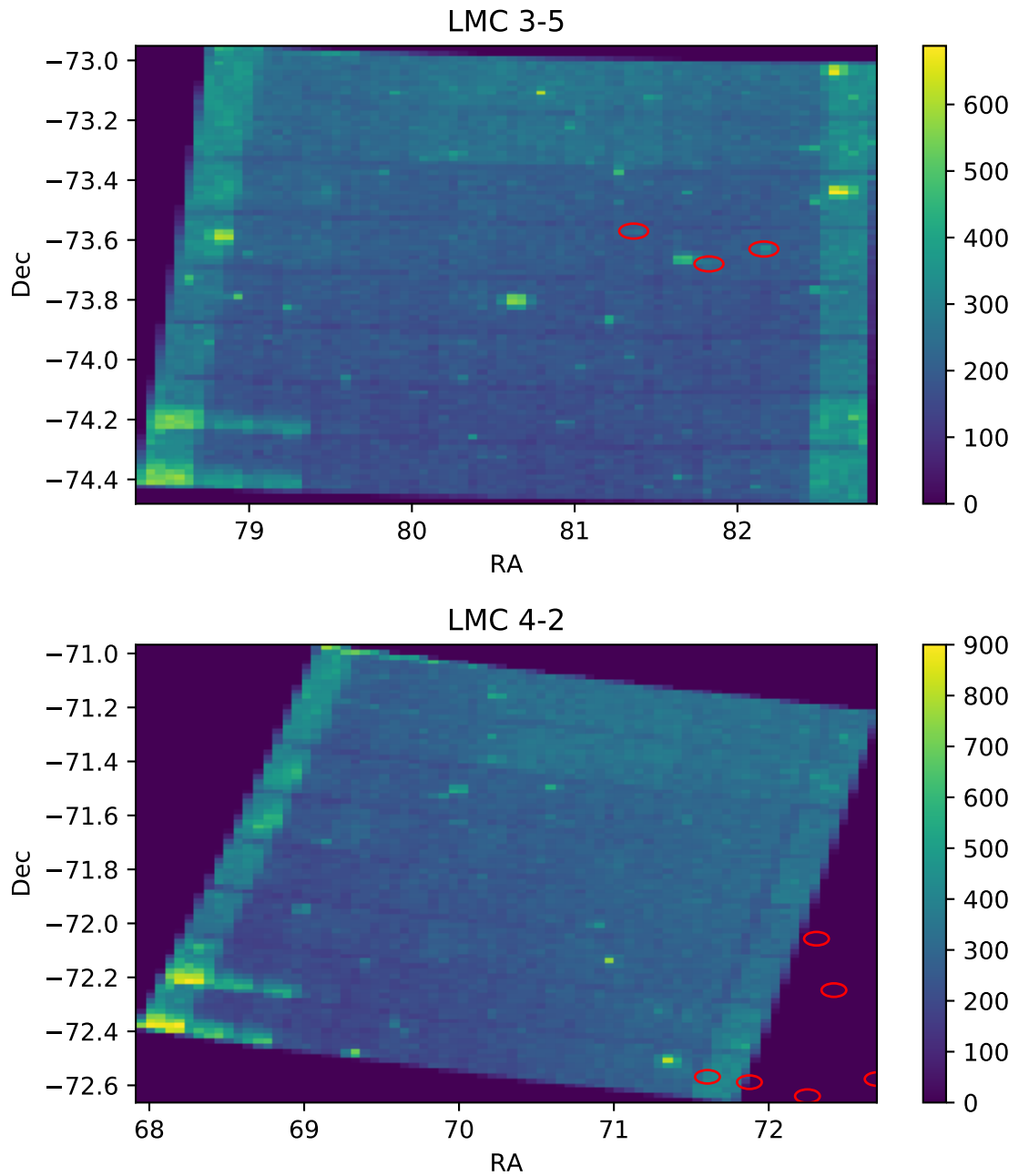


Figure A.1: The star densities of survey tiles. Red circles represent the clusters in [Palma et al. \(2016\)](#).

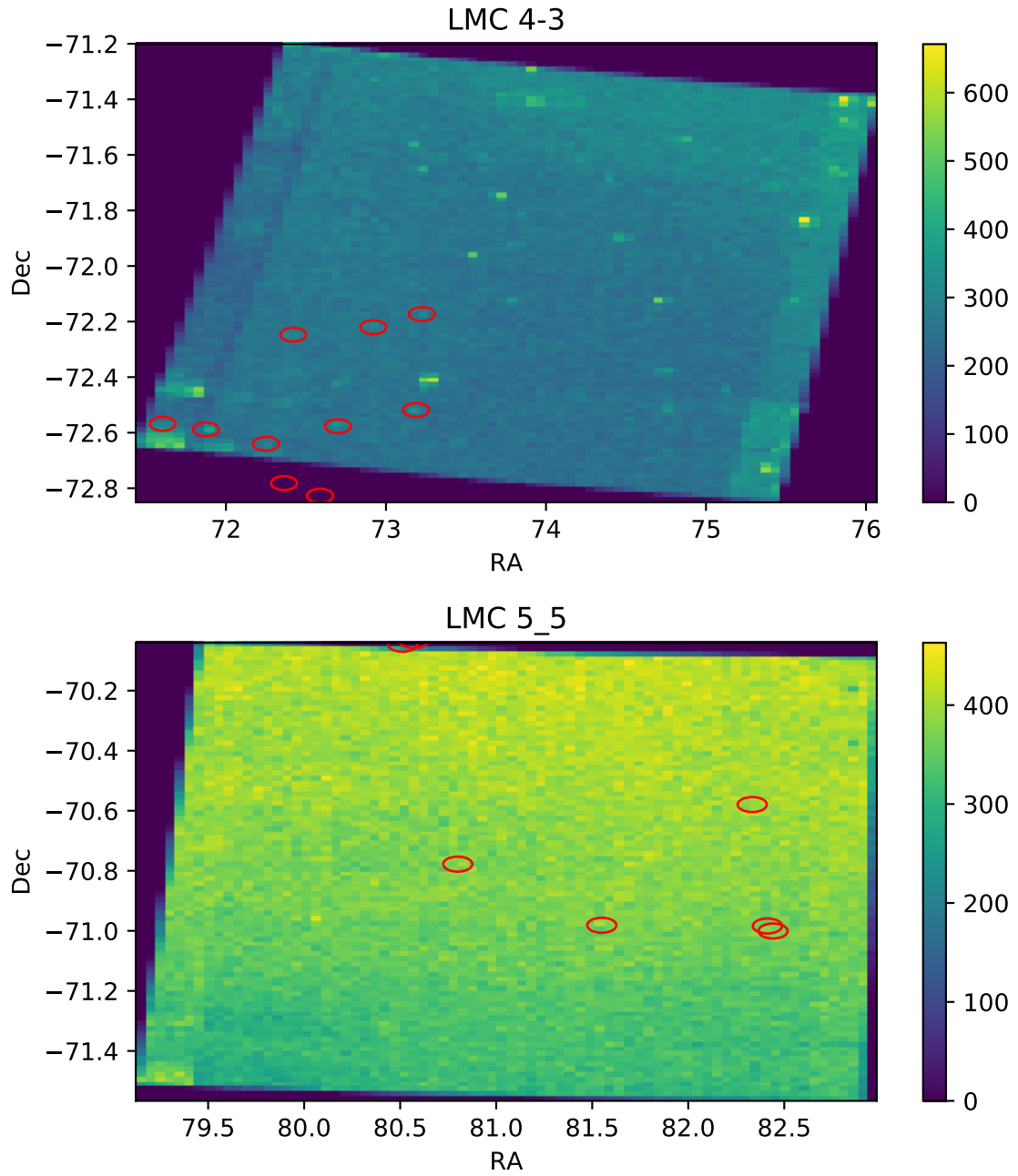


Figure A.2: Continued from Figure A.1

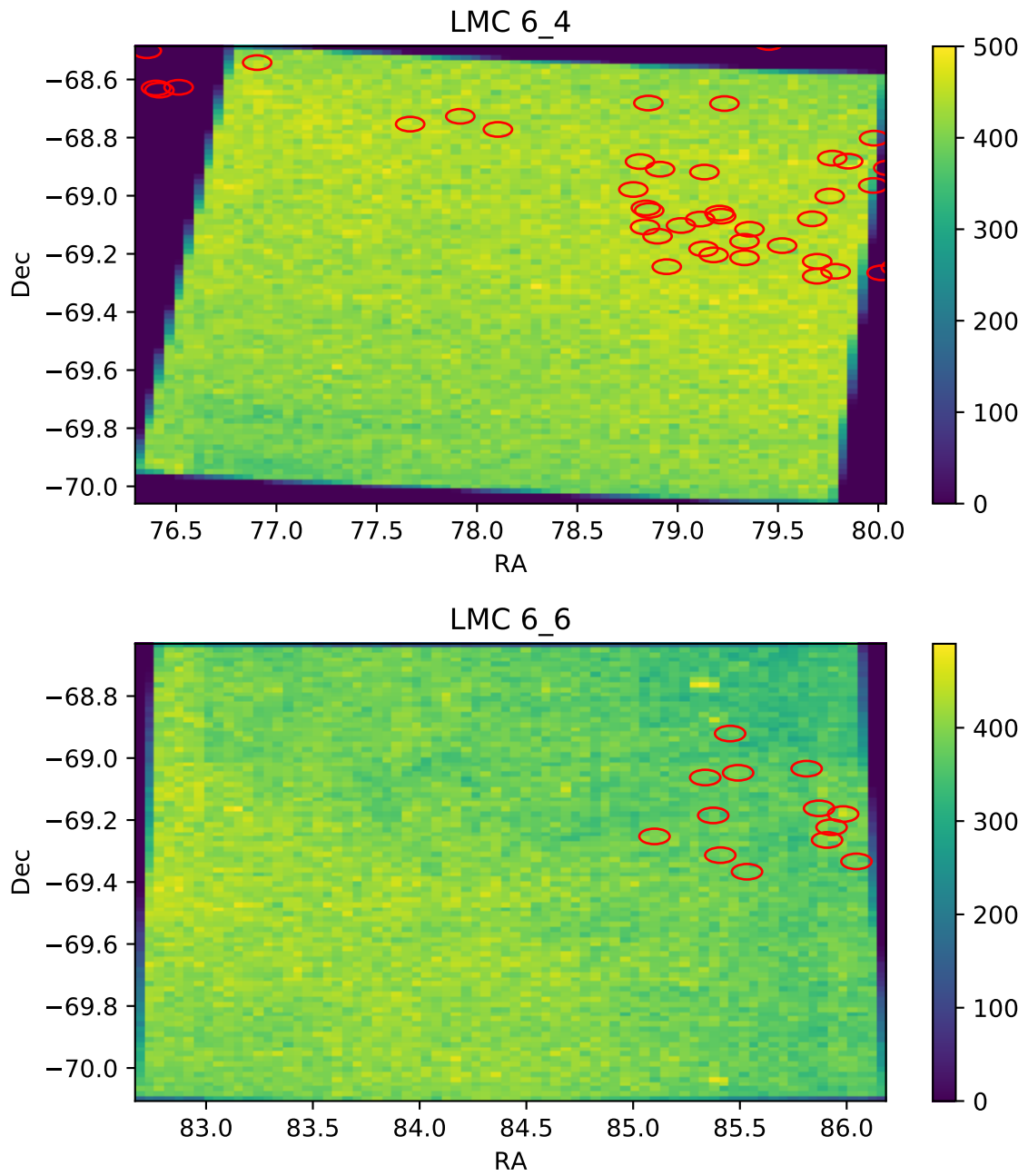


Figure A.3: Continued from Figure A.2

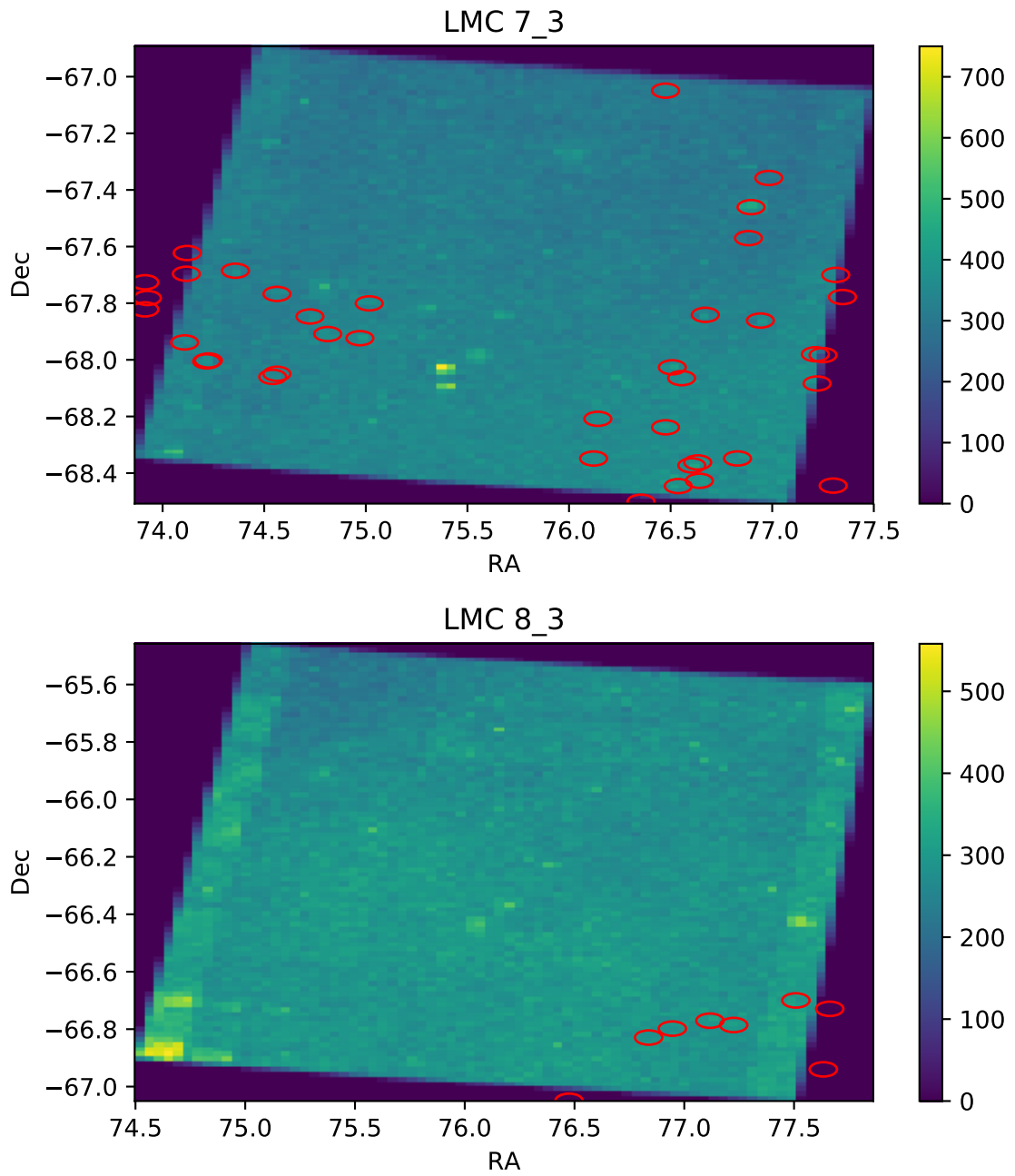


Figure A.4: Continued from Figure A.3

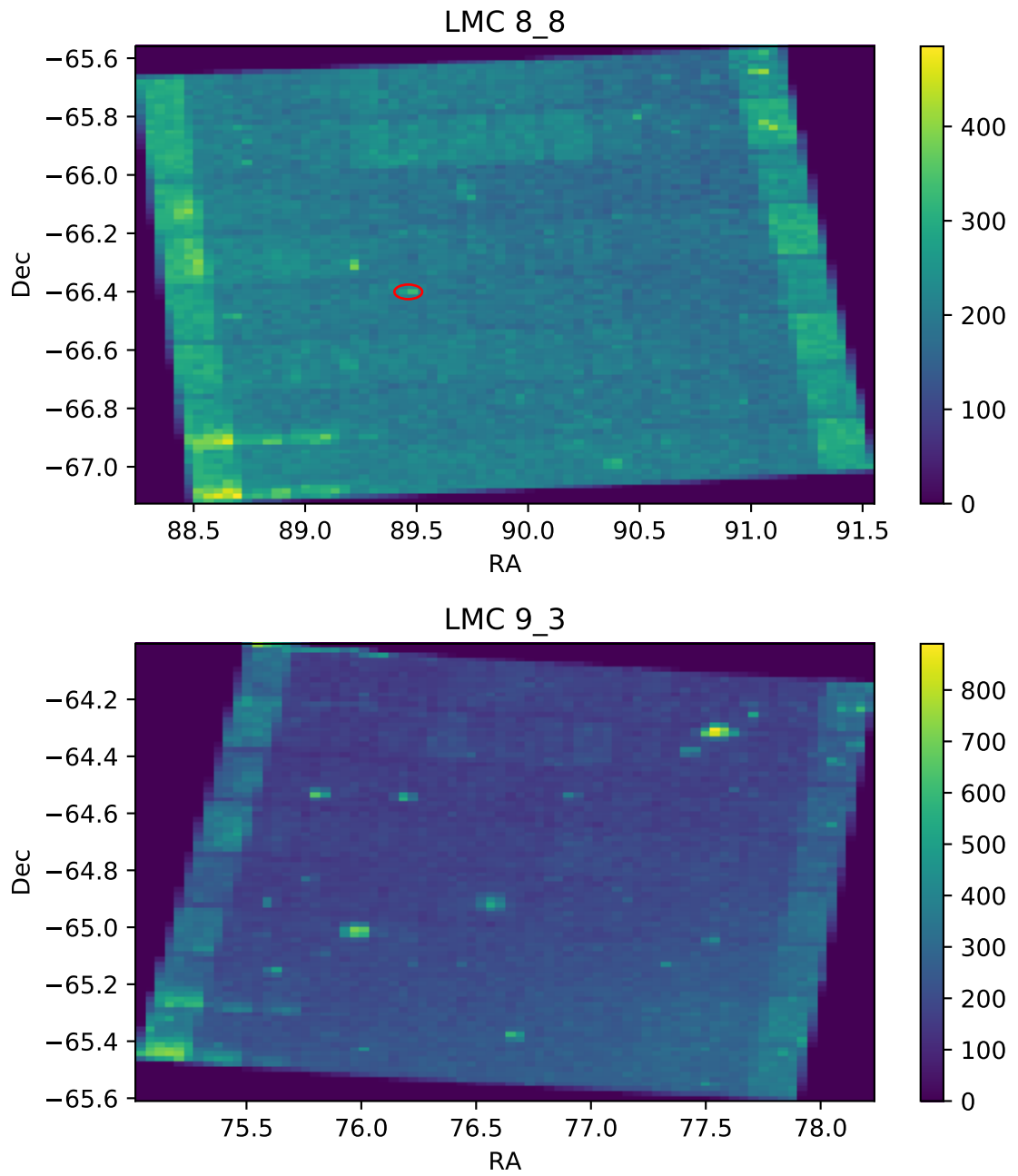


Figure A.5: Continued from Figure A.4